1D morphodynamical modelling of macro-tidal sandy beaches under pure tidal currents

PhD Thesis

By

Van Long Huynh



University of Nottingham

UK | CHINA | MALAYSIA

Faculty of Engineering

University of Nottingham

A thesis submitted to the University of Nottingham in accordance with the requirements for the degree of

Doctor of Philosophy

December 2018

Abstract

This research aims to study bed level evolution of a sandy beach under tidal effects over a long-time scale, using a fully-coupled hydro-morphodynamical numerical solver.

The proposed model originates from a system comprising nonlinear shallow water equations (NSWEs), an advection equation to describe suspended load and the Exner equation for bed change. Here non-flux conservative NSWEs are used, since no shock waves are formed by tidal motion. The moving boundary at the shoreline is treated by a coordinate transformation method (CTM) which can capture accurately the time variation of the shoreline. The absorbing-generating seaward boundary allows description of the outgoing hydrodynamic signals along with incoming signals. We also include the seaward boundary condition proposed by *Incelli et al.* [2015] to allow sediment to exit and enter the domain whilst maintaining the conservation. A fully coupled model with both bed-load and suspended-load transport is developed. The model performance is verified in both hydrodynamics and morphodynamics against available analytical and numerical solutions.

The morphodynamic evolution of a sandy beach under macro-tidal currents over a duration of 100 tidal cycles is investigated. We consider both bed load and suspended load transport, either in individual or combined mode. Furthermore,

we also consider how the coupling could affect bed change by considering the fully coupled against the quasi coupled one.

Regarding suspended load only, erosion is observed offshore; while deposition always occurs at the intertidal zone. The non zero bed change under symmetrical tide due to settling lag effect, which is the difference in phase between the suspended sediment concentration and velocity. Bed change due to suspended load depends not only on the exchange parameter but also on the bed mobility parameter. While bed mobility parameter mainly affects the bed change rate, the exchange parameter affects both bed change rate and patterns. Particularly, in case of low exchange parameter value, erosion is also observed in the sub-tidal region.

Bed change due solely to bed load is only significant in the intertidal region. This is partly due to the shock condition applied in the shoreline boundary. Moreover, the shoreline velocity due to transient from initial still water is much higher than normal, resulting in higher bed change after the first cycle compared to the remaining simulation time. Although the hydrodynamic nonlinearity is small in tidal motion, it still exists and is higher in the intertidal region than further offshore. As a result, the spatial derivatives of bed load flux is not zero and is higher in the intertidal region. Bed change under suspended load transport is more dominant than under bed load transport. Moreover, bed change under bed load converges after a shorter time than that due to suspended load.

The results of fully-coupled and quasi-coupled models qualitatively agree in bed change magnitude and pattern. The difference is proportional to bed change. In particular, the higher the bed change rate is, the greater the difference between the two model is. The quasi-coupled model obtains total suspended load or bed

load over a tide. Then bed change is only updated after every tide. The comparison results have shown that in cases of high bed mobility or low exchange parameter, the coupling effect is significant.

Dedication and acknowledgements

I am extremely grateful to my supervisor, Professor Nicholas Dodd, for his patience and providing me with the opportunity to undertake this research. I wish to thank him for all that I have learnt under his guidance, his help and above all, his dedicated support over the last four years. I would also like to thank Dr. Fangfang Zhu for her helpful advice and encouragement.

Throughout the course of this research I was in receipt of a generous grant from the Faculty of Engineering to whom I am indebted.

I would also like to acknowledge the help and support of my colleagues at the Coastal Dynamics and Engineering Research Team: Riccardo, Giorgio, Wenlong, Eranda, Waddaa, Ben, Diego. Special thanks to Wenlong, Eranda and Waddaa for their supports both academically and personally.

I wish to thank my parents for their endless encouragement and unconditional support to achieve this goal. Thanks to my dear brothers, Phuong, Hai and Nghia for the support they have given in their own way. Lastly, thanks to my wife, Tu, who accepts me for who I am, supports me with the things I choose to do and loves me no matter what.

Table of Contents

Page

List of Tables **ix**

List of Figures **x**

1 Introduction **1**

1.1 Nearshore region and macro-tidal environment 2

1.2 Aim and Objectives 8

1.3 Thesis Outline 9

2 Literature Review **11**

2.1 Morphodynamics in macro-tidal environments 12

2.2 Numerical methodology 17

2.2.1 Nonlinear shallow water equations and fully coupling model 17

2.2.2 Coordinate transformation method and Method of characteristics for boundary conditions 20

3 Governing Equations **24**

3.1 1D Nonlinear Shallow Water Equations 25

3.2 Exner Equation for Bed-load Transport 30

3.2.1 Bed-load sediment transport 31

3.3 Suspended Sediment Transport 33
3.4 Non-dimensionalisation and fully-coupled hydro-morphodynamical model 35
3.4.1 Non-dimensionalisation in swash motion 36
3.4.2 Non-dimensionalisation in tidal motion 37
3.5 Boundary Conditions 39
3.5.1 Shoreline BCs 39
3.5.2 Offshore BCs 42

4 Numerical Solver **44**
4.1 Coordinate Transformation Methodology 45
4.2 Boundary Conditions 51
4.3 Numerical Solver and Shapiro Filtering 59
4.4 Numerical scheme development 61

5 Verification Tests **65**
5.1 Hydrodynamics only 66
5.1.1 *Carrier and Greenspan* [1958] solutions 68
5.1.2 *Shen and Meyer* [1963] swash solution 77
5.1.3 *Hubbard and Dodd* [2002] numerical solutions 79
5.1.4 Offshore Boundary Verification 83
5.2 Advection equation of suspended sediment concentration 87
5.2.1 *Zhu and Dodd* [2015] solutions 87
5.2.2 *Pritchard and Hogg* [2003b] solutions 89
5.2.3 *Pritchard and Hogg* [2003a] solutions 94
5.3 Coupled hydro-morphodynamical verification 96

5.3.1 Bed change over a single event 97
5.3.2 Bed change over multiple events 100
5.4 Model convergence test 103

6 Morphodynamical Evolution of Plane Beach under pure Tidal Currents 110

6.1 Physical and corresponding dimensionless parameters; and numerical settings for tidal motion 112
6.1.1 Physical parameters 112
6.1.2 Justification of numerical settings 115
6.2 Suspended load transport only 117
6.2.1 Effect of variation in M and E 134
6.3 Bed load transport only 150
6.4 Combined load transport 158
6.5 Fully-coupled versus quasi-coupled hydro-morphodynamics model 161

7 Conclusions and Recommendations 167

7.1 Suspended-load only 168
7.2 Bed-load only and Combined mode 170
7.3 Coupling effect 172
7.4 Recommendations 173

A Appendix A: Sediment motion threshold for bed-load and suspended load 177

B Appendix B: Bed mobility under bed load and suspended load transport 182

Bibliography **187**

List of Tables

Table **Page**

6.1 Physical parameters of reference test 114
6.2 Numerical setting of reference test 115
6.3 Physical parameters of bed load test 151
6.4 Numerical setting of bed load test 151

List of Figures

Figure **Page**

1.1 Sketch of nearshore region. 3

1.2 Principal types of Tides [*NOAA*]. 4

1.3 The global distribution of tidal beaches *Short* [1991] 6

2.1 Example of equilibrium profile of tide- and wave- dominant tidal flats (*Friedrichs and Aubrey* [1996]) 17

3.1 Sketch definition of NSWEs in tidal motion. 25

3.2 Sketch of the shock for B at the shoreline both advancing and retreating in the physical domain. 41

4.1 Transformation from moving physical to fixed computational domain. 49

4.2 Sketch of the fully-coupled offshore BCs in the computational domain ($u < 0$). The squares indicate the nodes where the variables are obtained. 54

4.3 *Carrier and Greenspan* [1958] transient solution of x_s vs. t of Explicit scheme (black) and Implicit scheme (blue) without filtering. CG58 solutions: red dashed. 63

4.4 *Carrier and Greenspan* [1958] transient solution of u_s vs. t of Explicit scheme (black) and Implicit scheme (blue) without filtering. CG58 solutions: red dashed. 63
4.5 Filter test for CG58 periodic test. 64

5.1 Present results (solid line) against analytical *Carrier and Greenspan* [1958] transient solutions (red dotted) of the water surface elevation η versus cross-shore position x at every $\Delta t = 4.4$ from $t = 0$ to $t = 44$. The bottom line corresponds to initial condition, $t = 0$ and the top line corresponds to $t = 44$ 70
5.2 Present results (solid line) against analytical *Carrier and Greenspan* [1958] transient solutions (square dotted) of the shoreline position x_s (blue) and the shoreline velocity u_s (red) versus time t 70
5.3 Present results (solid line) against analytical *Carrier and Greenspan* [1958] transient solutions (red dotted) of (a): surface elevation η and (b): velocity u at offshore boundary 71
5.4 Present results (solid line) against analytical *Carrier and Greenspan* [1958] periodic solutions (black squared) of offshore hydrodynamics η_{off} (blue) and u_{off} (red) versus time t/T 74
5.5 Present results (solid line) against analytical *Carrier and Greenspan* [1958] periodic solutions (black squared) of shoreline hydrodynamics x_s (blue) and u_s (red) versus time t/T 74
5.6 Present results (black dotted) against analytical *Carrier and Greenspan* [1958] periodic solutions (red solid line) of (a): η and (b): u evolution for a full period 76
5.7 Sketch for PW01 initial condition 78

5.8 Contour plots of the present model solutions (black) of (a): h and (b): u in comparison with analytical solutions (red) 79

5.9 Present (solid lines) and *Hubbard and Dodd* [2002] (dashed lines) solutions of (a): the offshore water surface elevation η_{off}, (b): the offshore velocity u_{off} for $c_d = 0$ 82

5.10 Present (solid lines) and *Hubbard and Dodd* [2002] (dashed lines) solutions of the shoreline position x_s versus t/T for $c_d = 0$ (black), 0.01 (red), 0.025 (blue), 0.1(magenta) 83

5.11 Simultaneous generating-absorbing boundary conditions: Time series at $\bar{x} = 0$ for individual signal incoming signal η_i and outgoing signal η_r. The magnified subplot is the disturbance left within the domain after theoretical time elapsed 86

5.12 Simultaneous generating-absorbing boundary conditions: Time series at $\bar{x} = 0$ for total signal η 86

5.13 Contour plots of present model solution (black) against *Zhu and Dodd* [2015] (red dashed) of $c - u^2$ for exchange rate parameter of (a): $E = 0.001$ and (b): $E = 0.03$ 88

5.14 Evolution of c for a full period under *Carrier and Greenspan* [1958] flow conditions plotted at every $T/16$. (a): first half of run-up, (b): second half of run-up, (c): first half of run-down and (d): second half of run-down. *Pritchard and Hogg* [2003b] solutions: red dashed; present solutions: black solid 91

5.15 Instantaneous sediment flux $q(x,t) = chu$ versus time t at different locations. (i): $x = 0.0325$, (ii): $x = -0.0025$, (iii): $x = -0.0375$, (iv): $x =$ flài0.0725 and (v): $x =$ flài0.1075. *Pritchard and Hogg* [2003b] solutions: red dashed; present solutions: black solid 93

5.16 Net flux $Q(x) = \int_0^T q(x,t)dt$ over a period. *Pritchard and Hogg* [2003b] solutions: red dashed; present solutions: black solid 93

5.17 Evolution of c for a full period under tidal motion plotted at every $T/16$ during (a): flood; (b): ebb. *Pritchard and Hogg* [2003a] solutions: red dashed, present solutions: black solid 95

5.18 Net flux $Q(x)$ over a tidal cycle. *Pritchard and Hogg* [2003a] solutions: red dashed, present solutions: black solid 95

5.19 (a): Contour plots of ΔB, (b): Final bed change ΔB for *Shen and Meyer* [1963] swash event over a mobile bed of bed load only, $\sigma = 0.01$ and $M = 0$ (present model: black solid line, *Zhu and Dodd* [2013]: red dashed line) 98

5.20 Final bed change ΔB for *Shen and Meyer* [1963] swash event over a mobile bed of suspended load only, $\sigma = 0$. (a) $E = 1 \times 10^{-3}$ and varied M; (b) $M = 1 \times 10^{-4}$ and varied E (present model: solid line, *Zhu and Dodd* [2015]: dashed line) 99

5.21 Bed change ΔB between present model (dashed line) and *Incelli et al.* [2016] model (solid line) at $t = 1000T$ (black), $t = 2000T$ (red), $t = 3000T$ (blue) and $t = 4000T$ (magenta) 102

5.22 Sediment conservation of present model 103

5.23 Spatial grid convergence test result for hydrodynamics only. (a): in log scale, (b): in linear scale. 105

5.24 Error sensitivity test for different Courant number. The results of x_s versus t for *Carrier and Greenspan* [1958] periodic case 106

5.25 Spatial grid convergence test result for fully coupled model. (a): in log scale, (b): in linear scale. 108

5.26 Convergence test for morphodynamical simulation of *Shen and Meyer* [1963] swash event (solid black line: present solutions; red dashed line: solutions of [*Zhu and Dodd*, 2013]). The contour plot of ΔB for (a): $\Delta\bar{x} = 0.03125$ and (b): $\Delta\bar{x} = 0.01$ 109

6.1 Contour plot of u for 2 tides from $0 - 2T$ (bottom) and $98 - 100T$ (top).120

6.2 Contour plot of c for 2 tides from $0 - 2T$ (bottom) and $98 - 100T$ (top).121

6.3 Reference test results of c (blue), u^2 (black) and $c - u^2$ (magenta) versus t/T at periodic state (a): $x = -10$; (b): $x = -6$. Morphodynamics phases: E_f (red solid), E_e (red dashed), D_f (green solid) and D_e (green dashed). 123

6.4 Reference test results of c (blue), u^2 (black) and $c - u^2$ (magenta) versus t/T at periodic state (a): $x = -2$; (b): $x = 0$. 124

6.5 Reference test results of c (blue), u^2 (black) and $c - u^2$ (magenta) versus t/T at periodic state (a): $x = 0.25$; (b): $x = 0.75$. 125

6.6 Reference test result of each morphodynamic phase over a tide $10T - 11T$ vs. x: D_f (solid green), D_e (dashed green), E_f (solid red) and E_e (dashed red). 127

6.7 Reference test result of depositional (erosional) flux and net flux over a tide $10T - 11T$ vs. x. 129

6.8 Reference test result of bed change and depositional (erosional) flux over initial tide $0 - T$ vs. x. 131

6.9 Reference test result of bed change and depositional (erosional) flux over a tide $10T - 11T$ vs. x. 131

6.10 Reference test result of bed change and depositional (erosional) flux over whole simulation $0 - 100T$ vs. x. 132

6.11 Reference test result of ΔB vs. x after every 10 tides. The bed change after 100 tides is given in solid black line. 132

6.12 Results of c (blue), u^2 (black) and $c - u^2$ (magenta) versus t/T at periodic state of REF, low and high M (a): $x = -10$; (b): $x = 0.5$. Morphodynamics phases: E_f (red solid), E_e (red dashed), D_f (green solid) and D_e (green dashed). 136

6.13 ΔB versus x over the initial tide $0 - T$ for REF, low and high M . . 137

6.14 ΔB versus x over a tide after the periodic state achieved $10T - 11T$ for REF, low and high M 138

6.15 ΔB versus x over the whole simulation $0 - 100T$ for REF, low and high M 138

6.16 Results of c (blue), u^2 (black) and $c - u^2$ (magenta) versus t/T at periodic state of REF (solid), low E (dashed) (a): $x = -10$; (b): $x = -2$. Morphodynamics phases: E_f (red solid), E_e (red dashed), D_f (green solid) and D_e (green dashed). 140

6.17 Results of c (blue), u^2 (black) and $c - u^2$ (magenta) versus t/T at periodic state of REF (solid), low E (dashed) (a): $x = 0$; (b): $x = 0.5$. 141

6.18 Results of c (blue), u^2 (black) and $c - u^2$ (magenta) versus t/T at periodic state of REF (solid), high E (dashed-dot) (a): $x = -10$; (b): $x = -2$. Morphodynamics phases: E_f (red solid), E_e (red dashed), D_f (green solid) and D_e (green dashed). 142

6.19 Results of c (blue), u^2 (black) and $c - u^2$ (magenta) versus t/T at periodic state of REF (solid), high E (dashed-dot) (a): $x = 0$; (b): $x = 0.5$. 143

6.20 Morphodynamics phases versus x over a tide after the periodic state achieved $10T - 11T$ for low E. 144

6.21 Morphodynamics phases versus x over a tide after the periodic state achieved $10T - 11T$ for high E. 145

6.22 Erosional (depositional) flux and net bed change versus x over a tide after the periodic state achieved $10T - 11T$ for low E. 145

6.23 Erosional (depositional) flux and net bed change versus x over a tide after the periodic state achieved $10T - 11T$ for high E. 146

6.24 ΔB versus x after 100 tidal cycles for REF, low and high E 149

6.25 ΔB vs. x over 100 tides under bed load only, different velocity thresholds. 153

6.26 $B(100T) - B(10T)$ vs. x under bed load only, different velocity thresholds. 153

6.27 Bed change vs. x over a tide under bed load only, Grass formula: $0 - T$, $T - 2T$ and $10T - 11T$. 155

6.28 Bed change vs. x over a tide under bed load only, Grass formula: $10T - 11T$, $50T - 51T$ and $99T - 100T$. 155

6.29 Contour plot of ΔB over a tidal cycle $19T - 20T$ and $99T - 100T$ . . 157

6.30 Bed level at $t = 100T$ due to bed load transport only (Grass formula) with different initial conditions ($\sigma = 5 \times 10^{-4}$). 158

6.31 ΔB vs. x at $t = 100T$ under combined load transport. 159

6.32 Combined load of Grass and REF: ΔB vs. x at $t = 100T$. 160

6.33 Comparison between combined and the sum of individual modes of transport: ΔB vs. x at $t = 100T$. 161

6.34 Coupling test: ΔB vs. x after 100 tides under REF case. 163

6.35 Coupling test: ΔB vs. x after 100 tides under low M case. 164

6.36 Coupling test: ΔB vs. x after 100 tides under high M case. 164

6.37 Coupling test: ΔB vs. x after 100 tides under low E case. 165

6.38 Coupling test: ΔB vs. x after 100 tides under high E case. 165

6.39 Coupling test: ΔB vs. x after 100 tides under bed load transport only, Grass formula. 166

A.1 The augmented Shields Diagram as function of dimensionless grain size (*Allen* [1985]). 179

Chapter 1

Introduction

Coastal regions, the interfaces between land and ocean, change continuously under the dynamic interaction between various physical processes. The boundary between sea and land, known as the shoreline, varies in both time and space. These areas are an increasing source of interest in a number of human activities like travel, recreational, commercial and industrial activities. The interaction between land and the sea under severe weather conditions can result in progressive erosion of beaches, risks of settlements and structure damages. On the other hand, sediment accumulation can severely affect the efficiency of ports and harbours. It is therefore important to achieve better understanding of the physical processes involved in the evolution of the shape of coasts and the possibility to predict their long-term changes. The knowledge would guarantee safer environment and a sustainable approach to exploit coastal areas.

1.1 Nearshore region and macro-tidal environment

The nearshore is the region starting from where waves begin shoaling and ending at the shoreline (see Fig 1.1). *Masselink and Hughes* [2003] and *Svendsen* [2005] identified and described the possible physical process taking place in the nearshore area. The shoaling zone is the first zone starting from offshore, where waves propagating landward begin to be affected by reduced water depth which tends to increase the wave height. Moving shoreward, waves break at a certain height, signposting the surfzone. Breaking waves are usually associated with considerable energy dissipation and turbulence, and thus sediment resuspension and transport. Finally, the impact of waves on the foreshore, inundating and receding, marking the swash zone limit by two time-dependent boundaries, namely the run-up and run-down limits. This swash motion is therefore composed of two phases, the first with waves moving landward (run-up or uprush) and the second with waves directing seaward (run-down or backwash). The flow under this oscillatory process interacts and mobilises sediment as bed- and/or suspended load, inducing rapid change of the beach profile (*Svendsen* [2005]).

Tides are the periodic rise and fall of sea level due to combined effects of gravitational forces exerted by the Moon, the Sun and Earth's rotation. Tides vary on a larger timescale (ranging from hours to days) and lengthscale (ranging from hundreds to thousands metres) compared to swash events (normally in second and metre scales) (*Sorensen* [2005]). Similar to swash motion, tidal motion is composed of two phases associated with the rise and fall of water level. This oscillatory motion also delineates a region, namely the intertidal zone. Intertidal

zone is the region between the lowest and highest water levels of tidal motion. Sea level rises over several hours, until reaching the highest point (high tide). This stage covers the intertidal region and is known as flood tide. On the other hand, sea level falls during ebb tide, revealing the intertidal region, until reaching the lowest point (low tide). Tidal currents are directed landward during flood tide and vice versa during ebb tide. Tides are commonly semi-diurnal (two tidal cycles per day), or diurnal (one tidal cycle per day).

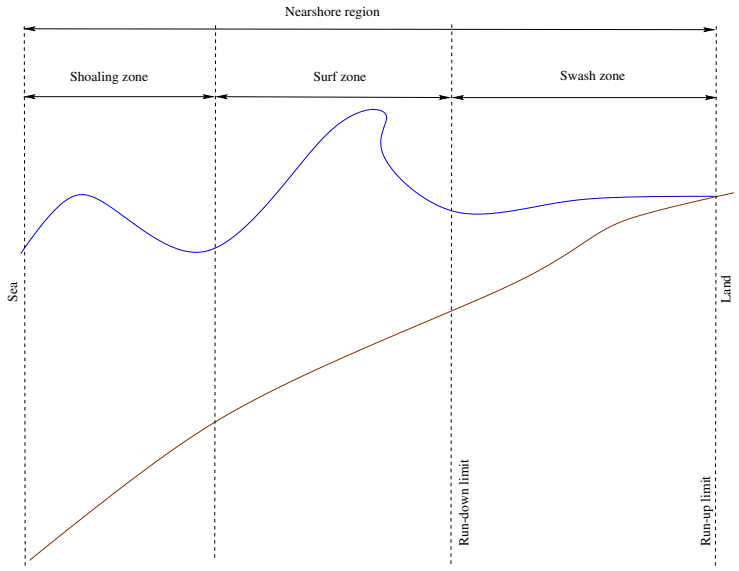


Figure 1.1: Sketch of nearshore region.

The difference in water level between the high tide and the succeeding low tide defines tidal range. Tidal range at a specific place is not constant over time but changes depending on the relative locations of the Sun, the Moon and the Earth. Approximately twice a month, around new moon and full moon, tidal range is at its maximum, namely the spring tide. On the other hand, at first quarter and third quarter moon, tidal range is at its minimum, namely neap tide. Examples of the distribution of tidal levels and phases are shown in Fig 1.2 [*NOAA*]. Since

the scales of tidal motion are larger than those for swash motion, the flow is less dynamical and is normally considered as a non-breaking long wave process. The flow under this oscillatory process interacts with and mobilises sediment. Coastal sediment is mainly transported by tidal currents, or by waves or very commonly by both currents and waves acting together (*Van Rijn* [1993]).

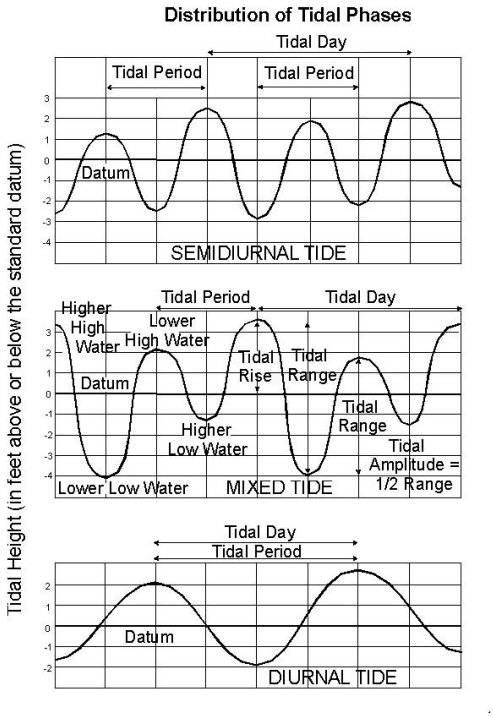


Figure 1.2: Principal types of Tides [*NOAA*].

Sediment is transported by the basic processes of entrainment, transportation and deposition (*Van Rijn* [1993]). These three processes take place at the same time and may interact with each other. *Van Rijn* [1993] has described these processes in detail. Entrainment is a result of the friction exerted on the sea bed by flows, with turbulent diffusion carrying sediment up into suspension. Transportation is defined as the sediment rolling, hopping and sliding along the bed in response to friction and gravity. This kind of transportation is defined as

bed load transport and is the dominant mode of transport for slow flows and/or large grains. If the flow is fast enough and the grain is fine enough, its turbulent is sufficient to erode sediment from the bed into suspension up to several metres higher than the bed level, which is then carried under the currents (*Soulsby* [1997]). This mode of sediment transport is defined as suspended load transport, which normally transports much greater sediment than bed load transport (*Soulsby* [1997]). Waves and sand with diameter less than $2mm$ are commonly found in nature. Turbulence by wave actions are capable to erode fine sediment into suspension. This is the reason why suspended load is more dominant than bed load transport. Deposition takes place when grains come to rest in bed load transport or by settling out of suspension in suspended load transport (*Van Rijn* [1993]). Tidal currents are considered as slow flows. Therefore, the sediment is mobilised under both manners of load transport. The evolution of beach profile under tides is considerable under a long-term time scale (years, decades or even longer)

In the presence of wind waves or surface gravity waves in the nearshore region, interaction between the flow and sediment is very complicated. The hydrodynamics under waves and currents interaction are complex, resulting in erosion and accretion on a continuous basis. The rates of bed change also vary considerably in time. However, influence of tides on beach morphology and beach morphodynamics is more subtle and not as well understood. Natural beaches can be grouped into several types based on multiple criteria, i.e. breaker height, tidal range, wave period (*Short* [1991]).

Based on tidal range, beaches have been classified accordingly into micro- ($<$ 2m), meso- ($2-4$m) and macro- ($>$ 4m) tidal beaches. However, as the

interaction between waves and tides is complicated, the morphology of different types of tidal environment will vary. The global distribution of tidal environments is illustrated in Fig 1.3 (*Short* [1991]). It is also noted that around the British Isles, tidal ranges are commonly larger than 4m and beaches are classified as macro-tidal environments (*BODC* [2013]). Over the past decades, increasing efforts have been made to investigate both the hydrodynamics and morphodynamics of these regions. The impact of tidal currents in macro-tidal environment is significant due to high tidal variation. For macro-tidal beaches, the shoreline variation is large and a wide beach length of hundreds or even thousands metres will be exposed and/or submerged due to variation in tide, adding complexity toward the hydrodynamics and morphodynamics in this region (*Friedrichs and Aubrey* [1996]).

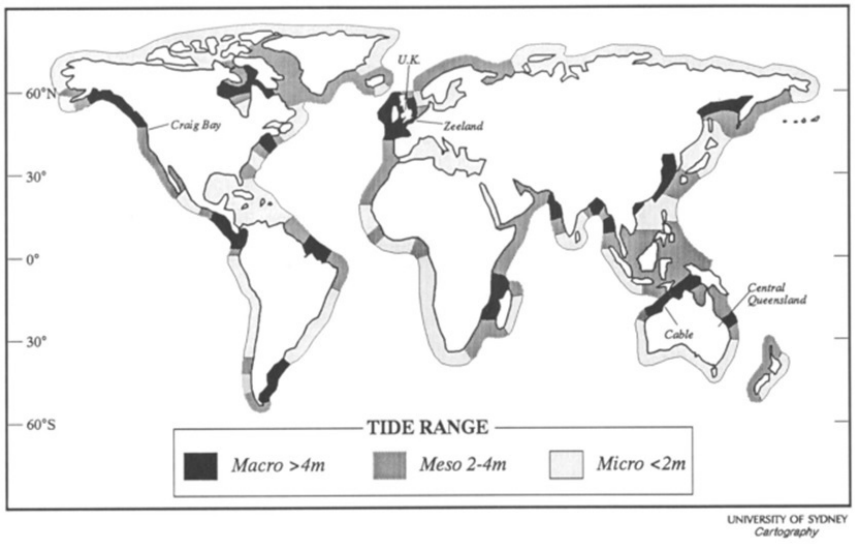


Figure 1.3: The global distribution of tidal beaches *Short* [1991]

Tidal effects on macro-tidal environment are not well understood although field observations have indicated that tides can strongly affect the type, intensity

and duration of wave processes on cross-shore profile (*Kroon and Masselink* [2002] and *Price and Ruessink* [2008]). Tides can modulate the surf zone circulation, wave breaking and swash bar dynamics (*Le Hir et al.* [2000]). In severe weather conditions, high tides allow the swash zone to operate on the upper beaches. There is no doubt that tidal effects are a key parameter in morphology of macro-tidal environment. The sediment, which is resuspended into the water column by means of turbulence due to wave breaking or various hydrodynamics interaction, is mainly transported by tidal currents (*Soulsby* [1997]). Furthermore, under weak flows such as tidal currents and large grain in sandy beaches, the bed load transport also becomes important (*Soulsby* [1997]). A better understanding of tidal effects on morphodynamics is necessary for justification of any engineering applications in a macro-tidal environment, particularly in those beaches being nourished.

Tides are considered non-breaking long waves where the water depth is much smaller than wave length (*Özkan-Haller and Kirby* [1997]). The hydrodynamics of this motion can be well described by the depth-averaged nonlinear shallow water equations (hereinafter NSWEs) (see *Peregrine* [1967]). These descriptions are also suitable to estimate the hydrodynamics of the surf-zone toward the shoreline where non-linearities are predominant (*Brocchini and Dodd* [2008]). There are many available morphodynamics models being developed on the NSWEs. However, most of them focus on the morphodynamics of the swash region (see *Liu et al.* [2008] for detailed reviews).

Using a numerical model allows us to examine the effects of macro-tide separately without wind-waves effects that cannot be investigated in reality. The wetting and drying (i.e. cross-shore behaviour) is intrinsic to the tidal motion

and needs to be implemented into the numerical model. So, this behaviour needs to be investigated. We firstly consider cross-shore dimension only and neglect the alongshore dimension. However, it is noted that the alongshore component is still important.

1.2 Aim and Objectives

From the above identified problems, the main focus of this research is to understand the morphodynamics of sandy beaches under the effects of pure macro-tidal currents. A numerical model, which includes tidal motion description as the main hydrodynamics, is developed. In this model, both suspended and bed-load transport are considered. The morphodynamics evolution of a plane sandy beach under macro-tidal currents will be investigated for seasonal scale of days or months. The main aim is pursued through the following objectives:

- To identify a system of nonlinear equations that adequately describe both the hydrodynamics and morphodynamics of intertidal region. The governing equations should be able to represent the hydrodynamics of non-breaking long waves motion such as tides and to reliably predict the beach change under a long-term simulation of multiple events;

- To develop a computational model which is able to solve the governing equations numerically;

- To assess the performance and robustness of the model against available analytical and numerical solutions from literature;

- To simulate the macro-tidal environment hydrodynamics;

- To investigate the morphodynamics under these hydrodynamics conditions.

1.3 Thesis Outline

This introductory chapter provides the research motivation and background. The aim and objectives of the following chapters are also given below.

§ 2 presents a review of some relevant works on the macro-tidal morphodynamics, which focus on the development of the numerical model.

§ 3 presents the governing equations used in the model, which includes NSWEs hydrodynamics, suspended concentration equation and then the bed change due to both bed and suspended load transports. Absorbing-generating offshore boundary conditions, based on Method of Characteristic developed by *Kobayashi et al.* [1987] and *Incelli et al.* [2015], are presented.

The numerical scheme and treatment of the so-called moving boundary problem are described in § 4.

Several verification tests are described in § 5, drawing attention to specific aspects of the present model performance. These preliminary assessments are necessary to enhance confidence in both reasonable and realistic morphodynamics predictions later on. Those tests are mostly for swash dynamics. The reason for this is that swash morphodynamics can be described by the same equations considered here, and there are many more verification tests available for the swash

than for tidal motion; and these are often more demanding than those for the equivalent tidal problems.

§ 6 presents the evolution of plane beaches over seasonal time-scale of months including both suspended and bed load transport (both individual and combined) under tidal hydrodynamics. Additionally, bed profile under tidal currents are either updated simultaneously (fully coupled) or after each tide (quasi coupled). The solutions of different coupling modes are compared. This raises some interesting findings on the level of impact coupling could have on the morphodynamics modelling. The difference between these models can illustrate how the coupling degree could be simplified but still maintain accuracy as in the fully coupled model.

Finally, § 7 provides the conclusions of this research and suggests some possible future developments, which the author hopes can lead to further understanding of morphodynamics macro-tidal environments, particularly when perturbations such as beach nourishment are included.

CHAPTER 2

Literature Review

Beach morphology varies in time due to the interaction with changing hydrodynamic forces (tides and waves) and response to the geographical variability in environmental conditions (waves, tides, sediments, geology, etc.). These conditions have been widely applied in literature for beach classification (*Masselink and Short* [1993]). It is useful to provide a conceptual framework within which the nearshore region can be studied and understood. On all natural beaches, processes and morphology are predominantly influenced by waves and tides. Beach environment can be classified based on tidal ranges. However, as *Davis and Hayes* [1984], *Short* [1991] and *Masselink and Short* [1993] indicated, beach morphology is not simply dependent on wave height or tidal range, but on interaction of the two.

2.1 Morphodynamics in macro-tidal environments

Existing micro-tidal beach models assume a micro-tidal range in the presence of wind or surface gravity waves, in which the intertidal zone and tidal currents are small and do not contribute much into the morphodynamics (*Short* [1991]). These models assume tidal currents and tidal level variations negligible. However, these assumptions do not hold in a macro-tidal beach environment. For high tidal range, the shoreline mobility is induced by tides on both wave dynamics and morphodynamics (*Masselink and Short* [1993]). *Masselink and Short* [1993] indicated that the interaction among tides, waves and sediment on beaches with the mean spring tide range exceeding 3m is complicated, since not much of their dynamics are truly known. *Wright and Short* [1984] used wave breaker height, wave period, high tide sediment fall velocity and tidal range to classify micro-tidal beaches. *Masselink and Short* [1993] developed the same conceptual framework on the macro-tidal environment to classify wave-dominated beaches in all tidal ranges. Their investigation on morphology of macro-tidal beach is still restricted to certain sites or hydrodynamic conditions. The results were also compared against the in situ observation and measurements. However, their framework is only applicable for classification purpose without giving any further prediction on the future evolution of bed profile.

Tides are usually considered as the dominant factor to shape the morphology of tidal flats (*Le Hir et al.* [2000], *Pritchard et al.* [2002] and *Friedrichs* [2011]). Tidal currents are large-scale flow circulation and can be split into cross-shore and long-shore components. The relative magnitude of these components depends

on the local geology and hydrodynamics properties. *Le Hir et al.* [2000] has indicated that the cross-shore component usually acts as responsible driver to the morphodynamics of intertidal region.

Over the past decade, the bed profile of macro-tidal flats have been extensively studied but are limited by specific conditions, mostly focusing on the cross-shore profile of muddy flats (*Roberts et al.* [2000], *Pritchard and Hogg* [2003a], *Friedrichs* [2011] and *Zhou et al.* [2015]). These types of flats are commonly found in nature, particularly in estuaries where sediment supply from rivers is abundant. The formation of tidal flat and long-term evolution are governed by interaction between a variety of factors, particularly tidal currents, wind waves, sediment supply, fluvial inflow, biological and anthropogenic activities (*Friedrichs* [2011] and *Coco et al.* [2013]).

Sediment supply (fluvial or marine) can pronouncedly alter the width and overall shape of tidal flats, even at a seasonal scale (*Liu et al.* [2011]). Abundant sediment supply promotes the progradation of tidal flats while insufficient sediment supply results in erosion (*Roberts et al.* [2000] and *Pritchard et al.* [2002]). River flows also affect the flow field and suspended sediment transport pattern. Its influence on intertidal flats depends on the magnitude of discharge and associated sediment source (*Zhou et al.* [2014]). Based on field observations of the Seine estuary, *Deloffre et al.* [2005] found that accretion of intertidal flats occurred during high river inflow and erosion during low river inflow. Human-induced influences, e.g. land reclamation, have been found to play an increasingly stronger role on the morphodynamics and ecosystems of tidal flats (see *Wang et al.* [2012]).

Friedrichs and Aubrey [1996] assumed a uniform spatial distribution of maximum bottom shear stress, and derived elegant analytical solutions of equilibrium

profiles of tidal flats for both tide and wave-dominated environment. They demonstrated that convex-up and concave-up hypsometries of tidal flats with straight shorelines were favoured by the dominance of tidal currents and waves, respectively (see Fig. 2.1). *Roberts et al.* [2000] developed numerical models solving the shallow water equations together with an advection equation of suspended concentration. Their model simulated the equilibrium mudflat profile shapes under suspended load transport over a long-term scale (in decades). The suspended sediment concentration is averaged tidally and then the bed level is updated after every tide. They assumed that the depth-averaged velocity and water elevation level are functions of time only, thus are constant with the space throughout the computational domain at any certain time. The wind waves effect, as a suspension factor, is described through a simple mathemetical model. It allows prediction of the equilibrium profile of tidal flats under tides alone or both tides and waves. The results indicated that the large tidal ranges corresponded to steeper mudflats while the action of waves was shown leading to a concave upwards profile, which qualitatively agreed with those predictions of *Friedrichs and Aubrey* [1996].

Extending the work of *Roberts et al.* [2000], *Pritchard et al.* [2002] and *Pritchard and Hogg* [2003a] investigated the long-term morphodynamics of tide-dominated mudflats under different combinations of sediment supply and tidal boundaries. They only focus on the advection of suspended sediment concentration under the depth-averaged shallow water hydrodynamics without including any bed change calculation. The suspended sediment concentration are averaged over every tidal cycle. They observed the tendency of direct sediment landward that leads to the accretion of sediment in the intertidal region. These findings also indicate that the cross-shore width of tidal flats or the magnitude of accretion increases with

rising sediment supply but is independent from tidal range.

The effects of other physical processes on tidal flats have also been investigated. *Fagherazzi and Wiberg* [2009] and *Mariotti and Fagherazzi* [2013] studied the effects of wind waves and fetch-limited waves on large sediment resuspension on shallow water tidal flats. They defined a parameter called erosional potential, which is a function of wave activity, tidal elevation, wind speed and directionally dependent fetch. This erosional potential was spatially integrated over the entire flat. Their finding was that together with the tidal oscillation, waves action tends to resuspend the sediment winthin the intertidal region, its peak occuring between the mean mid-tide level and mean high tide level, which leads to increasing erosional potential in the intertidal zone. From existing field measurements and numerical studies, *Bassoullet et al.* [2000] and *Roberts et al.* [2000] also suggested that waves generally favour offshore sediment transport which results in the erosion of tidal flats. *Pritchard and Hogg* [2003b] developed similar method to the approach for tide-dominant environment as in *Pritchard and Hogg* [2003a], but for smaller scale, e.g. waves in swash zone. They found out that without tidal oscillation, wave action tended to transport the suspended cohesive sediment landward, with the accretion of profile observed at the upper swash zone. Their findings does not agree with the erosion tendency of wave-dominant environment found in *Friedrichs and Aubrey* [1996] and *Roberts et al.* [2000]. Although tidal currents are the main transportation mechanism of suspended sediment (*Soulsby* [1997]); tidal hydrodynamics were not considered in *Pritchard and Hogg* [2003b] model. This may be responsible for the disagreement between *Pritchard and Hogg* [2003b] and *Friedrichs and Aubrey* [1996].

These literature numerical models were developed on shallow water equations

with the assumption that the spatial variation of velocity and water elevation level are negligible. Moreover, these models only focus on sediment transport under suspension. In slow flows such as tidal currents, bed load transport becomes more and more important. Although the contribution of bed load transport to the morphodyanmics is probably much smaller than suspended load transport, its effect should be taken into the account. However, there is no such model considering this type of sediment transportation. In addition, the considered sediment in these models are cohesive and sediment grain size is so small that the threshold of sediment movement in bed load transport becomes meaningless (see *Allen* [1985]).

Compared to a wide literature on profile shape of macro-tidal muddy flats, there is no such numerical modelling on the long-term morphodynamics of a tidal-dominant macro-tidal sandy beach. The main reason is that sandy beaches usually have wave actions. It is unlikely for a shallow sandy beach to have little wave activity, with the only possible exception of those in extremely sheltered environment. Although sandy beaches without wave action are not usually found in nature, it is important to understand the effect of tides alone, so to understand their role in beach evolution, particularly in a macro-tidal environment.

Moreover, the literature models either do not include the bed change calculations (*Pritchard et al.* [2002], *Pritchard and Hogg* [2003a]) or only update the bed at certain time level (*Roberts et al.* [2000], *Zhou et al.* [2015]). As a result, the hydrodynamics variation due to bed change is not considered or only considered after a certain time. For a long-term simulation of tides (years or decades), the effects of bed change on hydrodynamics and vice versa are significant. The question "how often bed profile should be updated without affecting the accuracy of

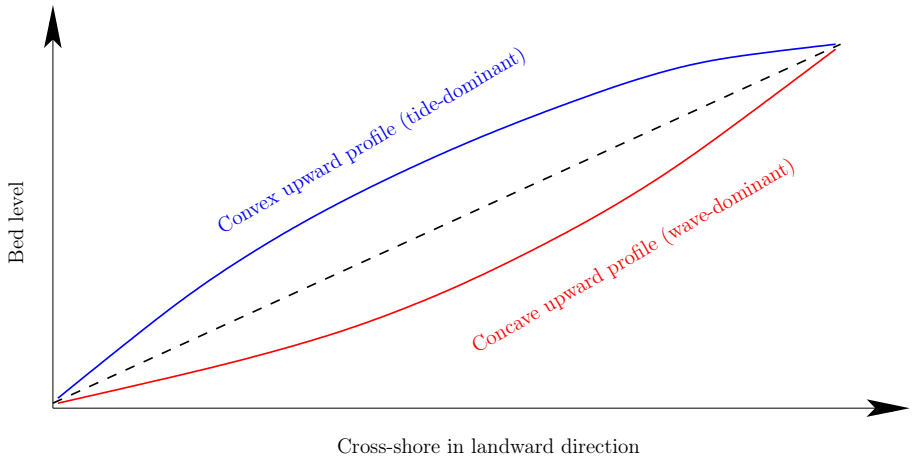


Figure 2.1: Example of equilibrium profile of tide- and wave- dominant tidal flats (*Friedrichs and Aubrey* [1996])

the model" needs to be investigated.

2.2 Numerical methodology

2.2.1 Nonlinear shallow water equations and fully coupling model

The shallow water approach is appropriate to describe the hydrodynamics of tidal flows, where the vertical length scale is much smaller than horizontal length scale (*Peregrine* [1967], *Özkan-Haller and Kirby* [1997], *Pritchard and Hogg* [2003a], *Liu et al.* [2008]). Under this condition, conservation of mass implies that the variation of velocity in vertical dimension is small. Moreover, the momentum equation implies that vertical pressure gradients are nearly hydrostatic (*Peregrine* [1967]), resulting in a constant velocity field throughout the depth of fluid. This allows the vertical component of velocity to be removed. Shallow water equations are suitable to model tides which have very large wavelength scales (over hundreds of

kilometres) (*Roberts et al.* [2000], *Pritchard and Hogg* [2003a]). It is also noted that shallow water equations are suitable to describe waves in the surf zone and swash zone since the condition of vertical length scale being much smaller than the horizontal length scale is still applicable (*Hibberd and Peregrine* [1979], *Titov and Synolakis* [1995], *Brocchini and Dodd* [2008]). This approach is well suited even for the steep gradient of sandy beaches of the order of 1/20 (*Peregrine* [1967]).

The shallow water equations are derived from equations of the conservation of mass and the conservation of linear momentum (the Navier-Stokes equations) (*Peregrine* [1967]), which hold even when the assumptions of shallow water break down, such as across a hydraulic jump. This is called the conservative form of shallow water equations and can be applied for breaking waves in swash zone when hydraulic jumps or discontinuities are found (*Brocchini and Dodd* [2008]). The non-conservative or primitive form of shallow water equations is obtained from expanding the conservative form by the product rule. Since velocities are not subject to a fundamental conservation equation, the non-conservative forms do not hold across a shock or hydraulic jump. This form is more simple and suitable to apply for non-breaking waves such as tidal motions or some specific wave conditions in swash zone. Many models based on shallow water equations have been developed to investigate the morphodynamics of tidal motions (*Roberts et al.* [2000], *Pritchard and Hogg* [2003a], *Zhou et al.* [2015]). These models, however, only focus on the suspended load transport of muddy sediments; and even do not include bed change computation in their governing equations (*Pritchard and Hogg* [2003a]). In this work, we apply the shallow water equations to describe tidal hydrodynamics. The hydrodynamics are written in the form of non-conservative

non-linear shallow water equations (hereinafter NSWEs). Details on the derivation of NSWEs and their applications are presented in the following chapters.

In numerical model, the coupling degree is the frequency of updating feedback from morphodynamics into hdyrodynamics. The fully coupled model is where hydrodynamics and morphodynamics are solved simultaneously in every time step. On the other hand, the model is called uncoupled if those two are computed subsequently, thus the change of hydrodynamics due to morphodynamics are not updated. In some models, the morphodynamic feedbacks into hydrodynamics are only included after a certain number of time steps. These are called weak-coupled or quasi-coupled models (see *Kelly and Dodd* [2010], *Reniers et al.* [2004]).

The fully coupled hydro-morphodynamical model are advantageous on allowing flow-by-flow processes. These couplings have been applied widely in solving hydro-morphodynamics of NSWEs such as multiple events in swash motions (*Dodd et al.* [2008]). In multiple-tide simulations, the fully coupled model is suitable to allow tide-by-tide processes and interactions between multiple tides. They allows any feedback from bed change into the hydrodyanmics to be updated simultaneously. Furthermore, the coupled model is advantageous in modelling sediment transport as it considers bed load and suspended load both individually and as a combined load of transport (see *Kobayashi and Johnson* [2001], *Kelly and Dodd* [2010], *Zhu and Dodd* [2015]). The disadvantage of fully-coupled model is that mathematical and numerical challenges can occur when complicated sediment transport formulae are employed (see *Castro Diaz et al.* [2008]). The uncoupled model allows more flexibility in choosing different integration time steps for hydrodynamic and morphodynamic modules as the solution of flow and bed change equations are solved separately (*Reniers et al.* [2004]). However,

the bed level solutions need to employ a targeted filter since spurious numerical oscillations can occur (see *Postacchini et al.* [2012]). Moreover, the effects of bed change on hydrodynamics are not considered in the uncoupled model. Compared to existing literature of fully-coupled hydro-morphodynamic model on swash motion, the fully coupled model on tidal motion is still limited. Existing models are either uncoupled (*Roberts et al.* [2000]) or only consider a fixed bed (*Pritchard and Hogg* [2003a]). In particular, fully-coupled model studies using NSWEs focus on the swash as the flows are more dynamical and bed change is at the same time-scale with the flow (see *Kelly and Dodd* [2009], *Kelly and Dodd* [2010], *Zhu and Dodd* [2013] and *Zhu and Dodd* [2015]). In the present study, we use fully coupled model to investigate the morphodynamics of tidal currents. We also apply simple sediment transport formulae to minimise the mathematical and numerical challenges which may occur for fully-coupled model.

2.2.2 Coordinate transformation method and Method of characteristics for boundary conditions

Many difficulties related to the NSWEs model have been recognised by many researchers (see *Özkan-Haller and Kirby* [1997], *Hubbard and Dodd* [2002], *Brocchini and Dodd* [2008]). One of the most challenging problems when modelling nearshore dynamics is properly describing the free-moving boundary condition at the shoreline of computational domain. The motion with time of this boundary, or the so-called run-up and run-down (or wetting and drying) (*Liu et al.* [2008]), is related to solutions over the whole domain. Challenges associated with the wetting and drying problem are mainly because the shoreline position is unknown from earlier and is a part of the solution. The computational domain is constrained by

this moving boundary which requires careful integration of the numerical model. Additionally, at the shoreline, water depth approaches zero but not velocity, thus degenerating the momentum equations of NSWEs to trivial zero solution; therefore, the singular solutions of partial differential equations may collapse due to numerical errors (*Liu et al.* [2008]). Many methods have been developed to deal with the moving boundary problem.

In CTM, the real, time-varying physical domain can be mapped onto a fixed computational domain through transformation equations. In traditional models, at any instant of time, the time dependent shoreline motion needs to be calculated as part of the computational domain. In CTM model, the shoreline boundary is fixed and shoreline position and the associated velocity are included in the model as a part of the governing equations (*Johns* [1982], *Takeda* [1984], *Özkan-Haller and Kirby* [1997] and *Prasad and Svendsen* [2003]). In CTM model, each fixed computational node or cell corresponds to the unique physical node or cell. The CTM changes the physical grid spacing such that time-varying wetting physical domain always corresponds to the fixed computational domain, thus requiring appropriate transform functions. These functions also transform the governing equations, therefore they should be simple for easy implementation and not posing mathematical and numerical challenges to the model (*Özkan-Haller and Kirby* [1997], *Brocchini et al.* [2002]).

Johns [1982] applied a simple linear transformation function and solved the NSWEs on a staggered grid and used linear extrapolation of the water surface elevation from interior nodes to obtain the shoreline position. Good agreement with the analytical periodic solution of *Carrier and Greenspan* [1958] has been obtained. *Takeda* [1984] applied a similar technique in Lagrangian coordinates with the path-

line method to reduce nonlinear instability. There was good agreement with the transient solutions of *Carrier and Greenspan* [1958]. However, some discrepancies were observed at the run-down phase, explained as the false reflection of numerical error at the shoreline, which later became magnified. *Özkan-Haller and Kirby* [1997] solved the NSWEs in characteristic form, with the computational domain transformed into a rectangular shape, in which spatial derivatives are obtained by spectral collocation. Chebyshev polynomials and trigonometric functions were applied in cross- and along-shore direction, respectively, to generate better resolution near the shoreline than further offshore. The solution was in good agreement with transient analytical solutions of *Carrier and Greenspan* [1958] and numerical solutions in 2D run up of *Zelt* [1986]. It is also noteworthy that they applied a high-order Shapiro filter (see *Shapiro* [1970]) to deal with aliasing instability by nonlinearity which caused spurious growth of undesired short waves. However this model includes a second transformation which increases nonlinearities in the governed equations; thus is difficult to implement when the morphodynamic equations are included. *Brocchini et al.* [2002] and *Prasad and Svendsen* [2003] applied a similar transformation with simple finite difference technique for NSWEs. They carefully obtain simple transformation functions through many tests. The numerical results are very accurate and highly agree with both transient and periodic analytical solutions of *Carrier and Greenspan* [1958]. Their transformation and numerical schemes are very simple and seem promising to implement in the fully-coupled model. *Zhou et al.* [2004] applied the same transformation as *Johns* [1982] to solve the NSWEs in Lagrangian framework. It was shown to give good agreement to the dam-break problem. Through literature review, the CTM reproduced well wetting and drying problem for both 1D and 2D

cases (*Brocchini et al.* [2002] and *Prasad and Svendsen* [2003]). We also expected that the morphodynamic models can be incorporated well with this method to predict bed changes.

Regarding the offshore boundary conditions, *Kobayashi et al.* [1987] applied Method of Characteristics on NSWEs to derive the absorbing-generating boundary conditions for hydrodynamics. It allows waves to exit the domain simultaneously with specifying incoming waves at the offshore boundary. The same technique was applied by *Özkan-Haller and Kirby* [1997] and *Van Dongeren and Svendsen* [1997] for NSWEs hydrodynamics in 2D to describe incoming waves at different directions. Furthermore, *Kelly and Dodd* [2009] and *Zhu* [2012] developed the boundary condition of NSWEs with advection equation for suspended concentration. Later, *Incelli et al.* [2015] included the Exner equation into characteristic equations, which describes the generating-absorbing condition for fully-coupled model. However, the advection equation of suspended sediment concentration was not considered and the method is invalid if linear approximation is not applicable (*Incelli et al.* [2015]).

CHAPTER 3

Governing Equations

In this chapter, the governing equations for water flows, advection equation of suspended sediment concentration and bed evolution on an erodible bed are presented. Firstly, for hydrodynamics, 1D NSWEs are presented (see § 3.1). A Chézy approach for the inclusion of bottom friction in the model is considered. Here, the 1D NSWEs are derived from the Navier-Stokes equations, in which effects of viscosity and compressibility are negligible. During derivation, long-wave assumption with very small water depth compared to wavelength, and zero vorticity assumption are applied. In this work, an advection equation of suspended sediment concentration is proposed to describe further physical aspect, depth-averaged suspended sediment concentration (see § 3.3). Bed-load transport by means of the well-known Grass or MPM formulae are described in an Exner-type equation (see § 3.2). The complete system of fully coupled model comprising bed evolution under both bed- and suspended load, and NSWEs are presented in non-dimensional in § 3.4. Finally, the offshore boundary conditions

for the system are presented in § 3.5

3.1 1D Nonlinear Shallow Water Equations

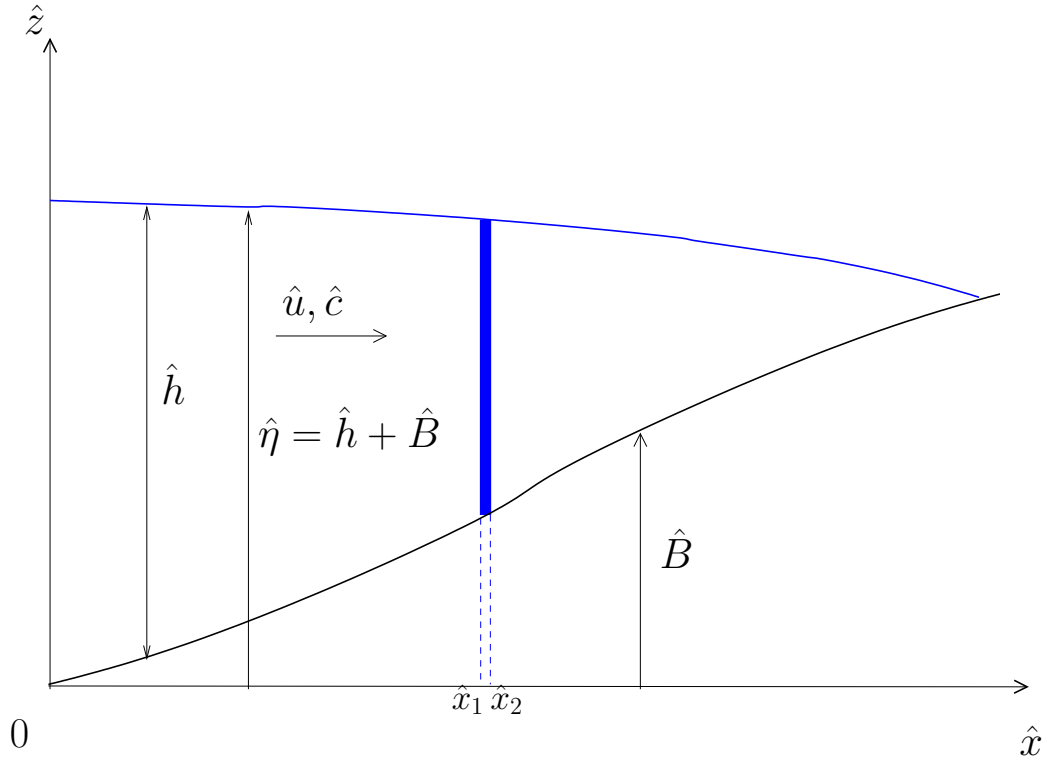


Figure 3.1: Sketch definition of NSWEs in tidal motion.

The schematic definition of NSWEs in tidal motion is shown in Fig. 3.1. Long wave motion, in which the water depth is very small in comparison to spatial scale of the flow (i.e. a wavelength), is assumed. This allows vertical accelerations of the fluid to be neglected, corresponding to a hydrostatic pressure distribution within the water column. As a result, the horizontal flow are depth-averaged (or depth-uniform) in which the vertical variation is negligible. Complete development of NSWEs from Navier-Stokes equations can be found in *Stoker* [1948], *Vreugdenhil*

[1994] and *Panton* [2005].

Consider mass balance over a control volume $\hat{\Omega}$, we have

$$\frac{d}{d\hat{t}}\int_{\hat{\Omega}} \hat{\rho} d\hat{V} = -\int_{\partial\hat{\Omega}} (\hat{\rho}\hat{\mathbf{U}}) \cdot \hat{\mathbf{n}} d\hat{A} \tag{3.1}$$

where LHS represents the time rate of change of total mass in $\hat{\Omega}$ and RHS represents net mass flux across boundary of $\hat{\Omega}$. $\hat{\mathbf{U}} = (\hat{u}, \hat{w})$ is fluid velocity along $\hat{x}$ and $\hat{z}$ directions, respectively. $\hat{z}$ is vertical coordinate, with positive direction upward, and $\hat{x}$ is 1D horizontal coordinate. $\hat{\mathbf{n}}$ is the outward unit normal vector on $\partial\hat{\Omega}$. It is noted that caret $\hat{}$ denotes dimensional variables, while dimensionless variables are unadorned. Subscripts $\hat{x}$ and $\hat{z}$ represent partial derivatives with respect to $\hat{x}$ and $\hat{z}$ respectively, e.g., $\hat{u}_{\hat{x}} = \frac{\partial \hat{u}}{\partial \hat{x}}$. Applying Gauss's theorem gives

$$\frac{d}{d\hat{t}}\int_{\hat{\Omega}} \hat{\rho} d\hat{V} = -\int_{\hat{\Omega}} \nabla \cdot (\hat{\rho}\hat{\mathbf{U}}) d\hat{V} \tag{3.2}$$

Assuming $\hat{\rho}$ is smooth, we can apply the Leibniz integral rule

$$\int_{\hat{\Omega}} \left[\hat{\rho}_{\hat{t}} + \nabla \cdot (\hat{\rho}\hat{\mathbf{U}})\right] d\hat{V} = 0 \tag{3.3}$$

Since $\hat{\Omega}$ is arbitrary,

$$\hat{\rho}_{\hat{t}} + \nabla \cdot (\hat{\rho}\hat{\mathbf{U}}) = 0 \tag{3.4}$$

Next, consider linear momentum balance over $\hat{\Omega}$, we have

$$\frac{d}{d\hat{t}}\int_{\hat{\Omega}} \hat{\rho}\hat{\mathbf{U}} d\hat{V} = -\int_{\partial\hat{\Omega}} (\hat{\rho}\hat{\mathbf{U}})\hat{\mathbf{U}} \cdot \hat{\mathbf{n}} d\hat{A} + \int_{\hat{\Omega}} \hat{\rho}\hat{\mathbf{b}} d\hat{V} + \int_{\partial\hat{\Omega}} \hat{\mathbf{T}}\hat{\mathbf{n}} d\hat{A} \tag{3.5}$$

where LHS represents time rate of change of total momentum in $\hat{\Omega}$; three terms in RHS represents the net momentum flux across boundary of $\hat{\Omega}$, the body forces acting on $\hat{\Omega}$ and the external forces acting on $\partial\hat{\Omega}$, respectively. $\hat{\mathbf{b}}$ is the body force density per unit mass acting on the fluid and $\hat{\mathbf{T}}$ is the Cauchy stress tensor (see *Panton* [2005] for more details). Applying Gauss's Theorem and rearranging gives

$$\frac{d}{d\hat{t}}\int_{\hat{\Omega}} \hat{\rho}\hat{\mathbf{U}} d\hat{V} + \int_{\hat{\Omega}} \nabla \cdot (\hat{\rho}\hat{\mathbf{U}}\hat{\mathbf{U}}) d\hat{V} - \int_{\hat{\Omega}} \hat{\rho}\hat{\mathbf{b}} d\hat{V} - \int_{\hat{\Omega}} \nabla \cdot \hat{\mathbf{T}} d\hat{V} = 0 \tag{3.6}$$

Assuming $\hat{\rho}\hat{\mathbf{U}}$ is smooth, we apply the Leibniz integral rule

$$\int_{\hat{\Omega}} \left[(\hat{\rho}\hat{\mathbf{U}})_{\hat{t}} + \nabla \cdot (\hat{\rho}\hat{\mathbf{U}}\hat{\mathbf{U}}) - \hat{\rho}\hat{\mathbf{b}} - \nabla \cdot \hat{\mathbf{T}} \right] dV = 0 \tag{3.7}$$

Since $\hat{\Omega}$ is arbitrary,

$$(\hat{\rho}\hat{\mathbf{U}})_{\hat{t}} + \nabla \cdot (\hat{\rho}\hat{\mathbf{U}}\hat{\mathbf{U}}) - \hat{\rho}\hat{\mathbf{b}} - \nabla \cdot \hat{\mathbf{T}} = 0 \tag{3.8}$$

The fluid is assumed incompressible. This means that $\hat{\rho}$ does not depend on pressure. However, it does not necessarily mean that $\hat{\rho}$ is constant. In ocean modelling, $\hat{\rho}$ also depends on the salinity and temperature of the sea water. Here, we assume salinity and temperature to be constant throughout our domain, so we can just take $\hat{\rho}$ as a constant. It is also noted that sea water is a Newtonian fluid and gravity is one body force, so

$$\hat{\rho}\hat{\mathbf{b}} = \hat{\rho}\hat{\mathbf{g}} + \hat{\rho}\hat{\mathbf{b}}_{other} \tag{3.9}$$

$$\hat{\mathbf{T}} = -\hat{p}\mathbf{I} + \bar{\mathbf{T}} \tag{3.10}$$

where $\hat{\mathbf{g}}$ is the acceleration due to gravity; $\hat{\mathbf{b}}_{other}$ are other body forces (e.g. the Coriolis force in rotating reference frames). We will neglect these other body forces for now. $\hat{p}$ is the pressure and $\bar{\mathbf{T}}$ is a matrix of stress terms. So (3.4) and (3.8) can be expressed in the form of

$$\nabla \cdot \hat{\mathbf{U}} = 0 \tag{3.11}$$

$$(\hat{\rho}\hat{\mathbf{U}})_{\hat{t}} + \nabla \cdot (\hat{\rho}\hat{\mathbf{U}}\hat{\mathbf{U}}) = -\nabla\hat{p} + \hat{\rho}\hat{\mathbf{g}} + \nabla \cdot \bar{\mathbf{T}} \tag{3.12}$$

(3.11) and (3.12) can be written in 2D form as

$$\hat{u}_{\hat{x}} + \hat{w}_{\hat{z}} = 0 \tag{3.13}$$

$$(\hat{\rho}\hat{u})_{\hat{t}} + (\hat{\rho}\hat{u}^2)_{\hat{x}} + (\hat{\rho}\hat{u}\hat{w})_{\hat{z}} = \frac{\partial(\hat{\tau}_{\hat{x}\hat{x}} - \hat{p})}{\partial\hat{x}} + \frac{\partial\hat{\tau}_{\hat{x}\hat{z}}}{\partial\hat{z}} \tag{3.14}$$

$$(\hat{\rho}\hat{w})_{\hat{t}} + (\hat{\rho}\hat{u}\hat{w})_{\hat{x}} + (\hat{\rho}\hat{u}\hat{w}^2)_{\hat{z}} = -\hat{\rho}\hat{g} + \frac{\partial\hat{\tau}_{\hat{x}\hat{z}}}{\partial\hat{x}} + \frac{\partial(\hat{\tau}_{\hat{x}\hat{z}} - \hat{p})}{\partial\hat{z}} \tag{3.15}$$

At the bottom boundary ($\hat{z} = \hat{B}$), where there is no slip and no normal flow, the bottom shear stress $\hat{\tau}_b$ are given as

$$\hat{u} = 0$$

$$\hat{u}\hat{B}_{\hat{x}} + w = 0$$

$$\hat{\tau}_b = \hat{\tau}_{\hat{x}\hat{x}}\hat{B}_{\hat{x}} + \hat{\tau}_{\hat{x}\hat{z}}$$

At the free surface ($\hat{z} = \hat{\eta}$), where there is no relative normal flow and surface atmospheric pressure, the surface shear stress $\hat{\tau}_s$ are given as

$$\hat{\eta}_{\hat{t}} + \hat{u}\hat{\eta}_{\hat{x}} - \hat{w} = 0$$

$$\hat{p} = 0$$

$$\hat{\tau}_s = -\hat{\tau}_{\hat{x}\hat{x}}\hat{\eta}_{\hat{x}} + \hat{\tau}_{\hat{x}\hat{z}}$$

Before we integrate over depth, we can examine the momentum equation for vertical velocity. By a scaling argument, all terms except the pressure derivative and gravity term are small. Then the z-momentum equation collapses to

$$\hat{p}_{\hat{z}} = \hat{\rho}\hat{g}$$

implying that

$$\hat{p} = \hat{\rho}\hat{g}(\hat{\eta} - \hat{z})$$

This is the hydrostatic pressure distribution. Then

$$\hat{p}_{\hat{x}} = \hat{\rho}\hat{g}\hat{\eta}_{\hat{x}}$$

We now integrate the continuity equation (3.11) from $\hat{z} = \hat{B}$ to $\hat{z} = \hat{\eta}$. Since

both $\hat{B}$ and $\hat{\eta}$ depend on $\hat{x}$ and $\hat{t}$, we apply the Leibniz integral rule:

$$\begin{aligned} 0 &= \int_{\hat{B}}^{\hat{\eta}} \nabla \cdot \hat{\mathbf{U}} d\hat{z} \\ &= \int_{\hat{B}}^{\hat{\eta}} \hat{u}_{\hat{x}} d\hat{z} + \hat{w}\Big|_{\hat{z}=\hat{\eta}} - \hat{w}\Big|_{\hat{z}=\hat{B}} \\ &= \frac{\partial}{\partial \hat{x}} \int_{\hat{B}}^{\hat{\eta}} \hat{u} d\hat{z} - \left(\hat{u}\Big|_{\hat{z}=\hat{\eta}} \hat{\eta}_{\hat{x}} + \hat{u}\Big|_{\hat{z}=\hat{B}} \hat{B}_{\hat{x}}\right) + \left(\hat{w}\Big|_{\hat{z}=\hat{\eta}} - \hat{w}\Big|_{\hat{z}=\hat{B}}\right) \end{aligned}$$

Defining depth-averaged velocity as

$$\bar{\hat{u}} = \frac{1}{\hat{h}} \int_{\hat{B}}^{\hat{\eta}} \hat{u} dz$$

We can use boundary conditions to get rid of the boundary terms. So the depth-averaged continuity equation is

$$\hat{h}_{\hat{t}} + (\hat{h}\bar{\hat{u}})_{\hat{x}} = 0 \tag{3.16}$$

Applying the same derivation to (3.12) yields

$$(\hat{h}\bar{\hat{u}})_{\hat{t}} + (\hat{h}\bar{\hat{u}}^2)_{\hat{x}} + \frac{1}{2}\hat{g}(\hat{h}^2)_{\hat{x}} + \hat{g}\hat{h}\hat{B}_{\hat{x}} = \frac{1}{\hat{\rho}}\left[\hat{\tau}_s - \hat{\tau}_b + \hat{F}\right] \tag{3.17}$$

where F is dissipative body force. Henceforth, $\hat{u}$ instead of $\bar{\hat{u}}$ is used to denote the depth-averaged velocity along $\hat{x}-$direction. The conservative momentum equation (3.17) can be expressed in primitive variable form as

$$\hat{u}_{\hat{t}} + \hat{u}\hat{u}_{\hat{x}} + \hat{g}(\hat{h} + \hat{B})_{\hat{x}} = \frac{1}{\hat{\rho}\hat{h}}\left[\hat{\tau}_s - \hat{\tau}_b + \hat{F}\right] \tag{3.18}$$

(3.16) and (3.17) represent, respectively, mass conservation and momentum conservation, thus constitute the 1D NSWEs in conservative form. It is noted that the conservative form NSWEs are suitable when hydraulic jump or discontinuity occurs (*Brocchini and Dodd* [2008]). We use the primitive form (3.18) instead of the conservative form (3.17) since the interested hydrodynamics are tidal motion

which are non-breaking waves. There is no discontinuity in non-breaking waves, so that the tide is well-described by primitive form (*Brocchini and Dodd* [2008]). Here, we only consider the bottom friction as the source term, which can be expressed through Chézy approach

$$\frac{\hat{\tau}_b}{\hat{\rho}} = c_d \left|\hat{u}\right| \hat{u} \tag{3.19}$$

where c_d is the non-dimensional friction coefficient, which is a function of the bed sediment grain size or, more broadly, the bed roughness. Here, we take a constant value of c_d.

3.2 Exner Equation for Bed-load Transport

In the bed evolution process, if only bed load is considered, the rate of bed change within a fixed region $[\hat{x}_1 \to \hat{x}_2]$ (Fig. 3.1) is equal to net sediment mass flux into and out of the region, i.e.

$$\frac{\partial}{\partial \hat{t}} \int_{\hat{x_1}}^{\hat{x_2}} \hat{B} d\hat{x} + \xi \Big[\hat{q}_b\Big]_{\hat{x}_1}^{\hat{x}_2} = 0 \tag{3.20}$$

where $\hat{q}_b$ is bed-load sediment flux, which is considered as a function of $\hat{h}$ and $\hat{u}$, and $\xi = \frac{1}{1-p}$ with p being bed porosity. Since $\hat{x}_1$ and $\hat{x}_2$ are fixed and independent from $\hat{t}$. Applying the Leibniz's law for continuous bed, (3.20) can be written as

$$\int_{\hat{x}_1}^{\hat{x}_2} \hat{B}_{\hat{t}} d\hat{x} + \int_{\hat{x}_1}^{\hat{x}_2} \xi (\hat{q}_b)_{\hat{x}} d\hat{x} = 0 \Rightarrow \int_{\hat{x}_1}^{\hat{x}_2} (\hat{B}_{\hat{t}} + \xi (\hat{q}_b)_{\hat{x}}) d\hat{x} = 0 \tag{3.21}$$

For any arbitrary fixed and continuous region, (3.21) is only valid if

$$\hat{B}_{\hat{t}} + \xi (\hat{q}_b)_{\hat{x}} = 0 \tag{3.22}$$

(3.22) is the Exner equation of bed evolution for bed-load sediment transport. The set of three governing equations (3.16), (3.18)and (3.22) are the fully-coupled

model for the hydro-morphodynamics system under bed-load transport. In this system, $\hat{q}_b$ stands for the instantaneous bed-load sediment flux, for which several formulae exist (see *Briganti et al.* [2012b], *Soulsby* [1997])

3.2.1 Bed-load sediment transport

In this work, two different formulae are considered. The first is the well-known Grass formula (see *Grass* [1981], *Soulsby* [1997], *Pritchard and Hogg* [2005], *Kelly and Dodd* [2009]):

$$\hat{q}_b = A\hat{u}^3 \tag{3.23}$$

where A is the sediment mobility parameter. A suitable value of A can be found from specific empirical data or can be computed alternatively from a simplification of standard sediment transport formulae such as those of Meyer-Peter Müller (MPM) or van Rijn. An excellent description of many sediment transport formulae in the coastal area can be found in *Soulsby* [1997] and *Fredsøe and Deigaard* [1992]. The relation between Grass formula and MPM formula can be seen in *Kelly* [2009]. The MPM formula is written as:

$$\hat{q}_b = 8.0(\theta - \theta_{cr})^{1.5}\Big[\hat{g}(s_{rel} - 1)D_{50}^3\Big]^{0.5} \tag{3.24}$$

where D_{50} is the median grain size, $s_{rel} = \frac{\hat{\rho}_s}{\hat{\rho}}$ is relative density of sediment ($\hat{\rho}_s$) compared to water ($\hat{\rho}$), $\theta = \frac{c_d\hat{u}^2}{\hat{g}(s_{rel}-1)D_{50}}$ is Shields parameter and $\theta_{cr,b}$ is the threshold for initiation of the bed-load sediment movement. Setting $\theta_{cr,b} = 0$, equating (3.23) and (3.24) yields:

$$A \equiv \frac{8}{\hat{g}(s_{rel} - 1)}c_d^{1.5} \tag{3.25}$$

From (3.25), MPM formula can be rewritten as follows:

$$\hat{q}_b = A(\hat{u}^2 - \hat{u}_{cr,b}^2)^{1.5} \tag{3.26}$$

where $\hat{u}_{cr,b}$ is bed-load sediment critical velocity at which the bed sediment is mobilised. A number of reasons justify the choice of these two bed load formulae among the others. The Grass formula is simple and straightforward with exact derivatives. It has been widely employed in previous literature, in both analytical solutions and numerical tests; therefore is useful for the later verification of the present model (see *Reniers et al.* [2013]).

The MPM formula, on the other hand is recognised as more physically based because of the threshold for the initiation of sediment transport. Moreover, the formula is explicitly dependent on the bottom shear stress and the bed sediment characteristics. The MPM formula is expected to lead to more realistic results in numerical simulations. It is also acknowledged that recent development of other bed-load transport formulae originates from the MPM formula, which includes incident wave conditions, near-bed excursion orbital and mean wave period (*Soulsby* [1997]). The formula is also widely used by many authors in investigation morphodynamics of NSWEs framework (*Briganti et al.* [2012b])

Following *Dodd et al.* [2008] and *Sriariyawat* [2009], the presence of a slope in flow direction affects the sediment transport, which either enhances or reduces the already mobilised sediment in down-slope or up-slope direction. This bed diffusion is included through an additional term, modifying the instantaneous bed-load transport formula:

$$\widetilde{q}_b = \hat{q}_b - \frac{1}{\tan\phi} |\hat{q}_b| \, (\Delta\hat{B})_{\hat{x}} \tag{3.27}$$

where ϕ is the angle of repose of the sediment, $\Delta\hat{B} = B(\hat{x},\hat{t}) - B(\hat{x},0)$ is the bed change from the initial bathymetry. If the downslope mobilisation is not considered, the term $1/\tan\phi = 0$, i.e. $\widetilde{q}_b = \hat{q}_b$. It is noted that the bed diffusion term in (3.27) is consistent with *Dodd et al.* [2008], as they consider the spatial

derivative of bed change $(\Delta\hat{B})_{\hat{x}}$ instead of bed level $\hat{B}_{\hat{x}}$. The reason for removing the contribution of initial bed level from the bed diffusion is that these and the previous literature (see *Falqués et al.* [1996], *Garnier et al.* [2008] also) focus on studying the evolution of 2DH bed patterns, i.e. beach cusps, long-shore/ oblique/ transverse bars, rip channels and the how development of these features from the initial bed profile that was assumed the equilibrium profile. In this work, the sloping effects are only considered in (3.27) for comparison with *Dodd et al.* [2008] to verify the current model under multiple events.

3.3 Suspended Sediment Transport

Suspended-load is taken into account in a similar manner to the bed-load system in § 3.2. The rate of bed change in arbitrary fixed domain $[\hat{x}_1, \hat{x}_2]$ (see Fig. 3.1) is equal to the total amount of suspended sediment settled down (entrained off) the bed (*Soulsby* [1997]) (there is no bed-load transport)

$$\frac{\partial}{\partial \hat{t}} \int_{\hat{x}_1}^{\hat{x}_2} \hat{B} d\hat{x} - \int_{\hat{x}_1}^{\hat{x}_2} \xi(\hat{D} - \hat{E}) d\hat{x} = 0 \tag{3.28}$$

where $\hat{D}$ is the deposition rate, expressed as the volume of sediment grain settling from suspension per unit area of bed per unit time. $\hat{E}$ is erosion rate, expressed as the volume of sediment grain eroded into suspension per unit area of bed per unit time. When the bed over domain $[\hat{x}_1, \hat{x}_2]$ is continuous, fixed and independent from $\hat{t}$, Leibniz's law is applied for (3.28) to yield:

$$\int_{\hat{x}_1}^{\hat{x}_2} \hat{B}_{\hat{t}} d\hat{x} - \int_{\hat{x}_1}^{\hat{x}_2} \xi(\hat{D} - \hat{E}) d\hat{x} = 0 \tag{3.29}$$

Therefore, for any arbitrary region (3.29) is only valid if

$$\hat{B}_{\hat{t}} - \xi(\hat{D} - \hat{E}) = 0 \tag{3.30}$$

(3.30) is the sediment conservation equation for suspended-load transport. For a combined system of both bed-load and suspended-load, the sediment conservation equation is derived by taking both sediment fluxes by bed-load and suspended-load into account. The rate of bed change over a fixed domain is equal to the total amount of net sediment flux into (out of) the region plus the sediment settled on (entrained off) the bed (*Soulsby* [1997]). The sediment conservation equation including both bed- and suspended-load is:

$$\hat{B}_{\hat{t}} + \xi\Big\{\hat{q}_{b\hat{x}} - (\hat{D} - \hat{E})\Big\} = 0 \tag{3.31}$$

The rate of change of total suspended sediment in the water column over a fixed domain $[\hat{x}_1, \hat{x}_2]$ is equal to the summation of net suspended sediment flux into (out of) the region and net sediment entrained into (settled from) the water column, i.e.:

$$\frac{\partial}{\partial \hat{t}} \int_{\hat{x}_1}^{\hat{x}_2} \hat{h}\hat{c}d\hat{x} + \Big[\hat{h}\hat{u}\hat{c}\Big]_{\hat{x}_1}^{\hat{x}_2} - \int_{\hat{x}_1}^{\hat{x}_2} (\hat{E} - \hat{D})d\hat{x} = 0 \tag{3.32}$$

where $\hat{c}$ is the depth-averaged concentration of suspended sediment. Applying Leibniz's law to (3.32) for region $[\hat{x}_1, \hat{x}_2]$, which is continuous, arbitrary and independent from $\hat{t}$, yields:

$$\int_{\hat{x}_1}^{\hat{x}_2} \Big\{(\hat{h}\hat{c})_{\hat{t}} + (\hat{h}\hat{u}\hat{c})_{\hat{x}} - (\hat{E} - \hat{D})\Big\}d\hat{x} = 0 \tag{3.33}$$

Therefore, the conservative form of suspended sediment transport is

$$(\hat{h}\hat{c})_{\hat{t}} + (\hat{h}\hat{u}\hat{c})_{\hat{x}} = (\hat{E} - \hat{D}) \tag{3.34}$$

From (3.16), (3.34) can be rewritten as:

$$\hat{c}_{\hat{t}} + \hat{u}\hat{c}_{\hat{x}} = \frac{1}{\hat{h}}(\hat{E} - \hat{D}) \tag{3.35}$$

The erosional and depositional rates are employed following *Pritchard and Hogg* [2003a] and *Pritchard and Hogg* [2005]

$$\hat{E} = \hat{m}_e \left(\frac{\hat{\tau} - \hat{\tau}_{cr,s}}{\hat{\tau}_0} \right) \tag{3.36}$$

$$\hat{D} = \hat{w}_s \hat{c} \tag{3.37}$$

where $\hat{\tau}_{cr,s}$ is threshold shear stress of sediment entrainment and $\hat{\tau}_0$ is a reference bed shear stress. $\hat{m}_e$ is a parameter related to rate of entrainment of sediment as suspended load, $\hat{w}_s$ is the effective settling velocity of suspended sediment. From (3.19), (3.36) can be rewritten as

$$\hat{E} = \hat{m}_e \left(\frac{\hat{u}^2 - \hat{u}^2_{cr,s}}{\hat{u}^2_0} \right) \tag{3.38}$$

where $\hat{u}_{cr,s}$ is suspended-sediment critical velocity at which the sediment is eroded into water column and $\hat{u}_0$ is a reference velocity corresponding to $\hat{\tau}_0$.

Using the sediment fluxes formulae of § 3.2 and § 3.3, (3.31) and (3.35) for combined system of bed-load and suspended-load become

$$\hat{B}_{\hat{t}} + 3\xi A \left|\hat{u}\right| (\hat{u}^2 - \hat{u}^2_{cr,b})^{0.5} \hat{u}_{\hat{x}} = \xi \left\{ \hat{w}_s \hat{c} - \hat{m}_e \left(\frac{\hat{u}^2 - \hat{u}^2_{cr,s}}{\hat{u}^2_0} \right) \right\} \tag{3.39}$$

$$\hat{c}_{\hat{t}} + \hat{u}\hat{c}_{\hat{x}} = \frac{1}{\hat{h}} \left\{ \hat{m}_e \left(\frac{\hat{u}^2 - \hat{u}^2_{cr,s}}{\hat{u}^2_0} \right) - \hat{w}_s \hat{c} \right\} \tag{3.40}$$

3.4 Non-dimensionalisation and fully-coupled hydro-morphodynamical model

The system of nonlinear equations (3.16), (3.18), (3.39) and (3.40), which are referred to as the combined load system as it considers both bed- and suspended-load, are consistent with the previous work of *Pritchard and Hogg* [2003a], *Zhou*

et al. [2015]. For swash motions, the threshold for bed motion of non-cohesive sediment is considered insignificant, and thus have no significant impact on morphodynamics. For tidal motion, most transport is effected by suspended load with waves entraining the sediment (*Pritchard and Hogg* [2003a]). Here, following *Zhu and Dodd* [2015], we use $\hat{u}_{s,cr} = 0$ for simplicity, (see Appendix A for more details). Non-dimensional variables are introduced to make results more inter-comparable. In this work, separate non-dimensionalisation for swash and tide is presented. The reason for swash non-dimensionalisation is the limitation of available coupling models for tidal motions. There are a number of NSWEs swash models developed by *Zhu and Dodd* [2013], *Zhu and Dodd* [2015], *Pritchard and Hogg* [2003b], that can be used for verification stage of NSWEs coupled model.

3.4.1 Non-dimensionalisation in swash motion

Following *Peregrine and Williams* [2001], *Carrier and Greenspan* [1958] we scale hydrodynamics and bed level on the vertical excursion of the swash and the concentration scale as given in *Pritchard and Hogg* [2003b]. The non-dimensional variables are:

$$x = \frac{\hat{x}}{\hat{h}_0}, t = \frac{\hat{g}^{1/2}\hat{t}}{\hat{h}_0^{1/2}}, h = \frac{\hat{h}}{\hat{h}_0}, u = \frac{\hat{u}}{\hat{u}_0}, B = \frac{\hat{B}}{\hat{h}_0}, c = \frac{\hat{c}}{\hat{c}_0} \tag{3.41}$$

where $\hat{h}_0$ is reference vertical length-scale, $\hat{c}_0 = \hat{m}_e/\hat{w}_s$ is reference concentration (*Pritchard and Hogg* [2003a] and *Pritchard and Hogg* [2003b]) and $\hat{u}_0 = \sqrt{\hat{g}\hat{h}_0}$ is reference velocity. Physically, if the sea bed is composed of a single grain size we can expect that $u_{s,cr} \geq u_{b,cr}$. For non-cohesive sediment of medium size (e.g. $0.2 - 2$mm, *Soulsby* [1997]) such as on sandy beach, this simplification will not significantly affect beach morphodynamics (*Zhu and Dodd* [2015]). Applying this

assumption and substituting the dimensional variables in (3.16), (3.18), (3.39) and (3.40) by the corresponding nondimensional forms in (3.41) yields

$$h_t + (hu)_x = 0 \tag{3.42}$$

$$u_t + uu_x + h_x + B_x = -c_d \frac{|u|\, u}{h} \tag{3.43}$$

$$c_t + uc_x = \frac{E}{h}(u^2 - c) \tag{3.44}$$

$$B_t + 3\sigma(u^2 - u_{cr,b}^2)u_x = M(c - u^2) \tag{3.45}$$

where $E = \frac{\hat{w}_s}{\hat{u}_0}$ is exchange rate parameter, which is representative of the setting velocity of the sediment, and is therefore related to the sediment grain size (see *Pritchard and Hogg* [2005]; *Zhu and Dodd* [2015]). $M = \frac{\xi \hat{m}_e}{\hat{u}_0}$ and $\sigma = \frac{\xi \hat{A}}{\hat{h}_0 \hat{u}_0}$ are dimensionless bed mobility with respect to suspended-load and bed-load, respectively (see *Zhu and Dodd* [2015]). To determine the range of E, σ and M, we refer to *Pritchard and Hogg* [2005], *Masselink and Hughes* [1998] and *Zhu and Dodd* [2015] for more details. In particular, E ranges from around 0.001 to 0.03; σ ranges from 5×10^{-4} to 0.01; and M ranges from 1×10^{-4} to 5×10^{-3}.

3.4.2 Non-dimensionalisation in tidal motion

The non-dimensionalisation in tidal motion is similar to that in swash motion, with the exception of including horizontal scale and time scale to better inter-comparable to hydrodynamics of tidal motion. The non-dimensional variables are:

$$x = \frac{\hat{x}}{\hat{x}_0}, t = \frac{\hat{t}}{\hat{T}_0}, h = \frac{\hat{h}}{\hat{h}_0}, u = \frac{\hat{u}}{\hat{u}_0}, B = \frac{\hat{B}}{\hat{h}_0}, c = \frac{\hat{c}}{\hat{c}_0} \tag{3.46}$$

where the reference vertical length scale $\hat{h}_0$ can be set to be tidal range; $\hat{x}_0$ is the horizontal length scale which is related to the vertical length scale through the gradient of the flat ($\tan\gamma$), i.e. $\hat{x}_0 = \frac{\hat{h}_0}{\tan\gamma}$; $\hat{T}_0$ is the time scale which can be set as

tidal period; and velocity scale $\hat{u}_0 = \frac{\hat{x}_0}{\hat{T}_0}$. The governing equations (3.16), (3.18), (3.39) and (3.40) are expressed in non-dimensional form of tidal motion as

$$h_t + (hu)_x = 0 \tag{3.47}$$

$$u_t + uu_x + \frac{1}{F^2}(h_x + B_x) = -\frac{c_d \hat{x}_0}{\hat{h}_0}\frac{|u|\,u}{h} \tag{3.48}$$

$$c_t + uc_x = \frac{E}{h}(u^2 - c) \tag{3.49}$$

$$B_t + 3\sigma(u^2 - u_{cr,b}^2)u_x = M(c - u^2) \tag{3.50}$$

Here the exchange rate $E = \frac{\hat{w}_s \hat{T}_0}{\hat{h}_0}$, the bed mobility with respect to suspended load $M = \frac{\xi \hat{m}_e \hat{T}_0}{\hat{h}_0}$ and bed load $\sigma = \frac{\xi \hat{A} \hat{x}_0^2}{\hat{h}_0 \hat{T}_0^2}$. The system of governing equations are similar between swash motion and tidal motion, so we apply the same annotation for E, M and σ as they are applied to the same physical processes. In macro-tidal motion reference, $F = \frac{\hat{u}_0}{(\hat{g}\hat{h}_0)^{1/2}}$ is the global Froude number, reflecting the flow regimes, typically of order 1×10^{-2} and the drag coefficient $C_D = \frac{c_d \hat{x}_0}{\hat{h}_0}$ is typically of order 1 (*Le Hir et al.* [2000], *Pritchard and Hogg* [2003a]). E is typically of order 1×10^2; σ is typically of order 1×10^{-3} and M is typically of order 1 (*Pritchard and Hogg* [2003a]).

It is noted that the governing equations are almost similar in both tidal and swash system. Values of M, E and σ are not the same due to the difference in length and time scales of these two systems. From the given equations and approximation of the parameters, we can make some further predictions of the system. Firstly, F is very small, resulting in a small spatial variation of hydrodynamics(see also *Pritchard and Hogg* [2003a]). It is also noted that E affect the advection of c too. The larger the value of E, the smaller the value of $u^2 - c$. It means c is closer to its instantaneous equilibrium state u^2. It is also noted that M and E are related to sediment property, thus likely to be linked in reality. However, we treated them

as independent parameters, allowing us to varying M and E independently and investigate how these parameters affect on the morpodynamics of tidal system.

The system is solved simultaneously to obtain four unknown variables h, u, c and B with bed level B being updated at every time-step. The numerical solver of this coupled hydro-morphodynamical model is presented in § 4. If the downslope mobilisation is taken into account (i.e. the bed diffusion in (3.21) is considered), the bed evolution equation given in (3.39) (or (3.50) is modified to include the slope term as

$$B_t + 3\sigma(u^2 - u_{cr,b}^2)u_x - 3\sigma\frac{u^2 - u_{cr,b}^2}{\tan\phi}u_x\Delta B_x - \sigma\frac{(u^2 - u_{cr,b}^2)^{1.5}}{\tan\phi}\Delta B_{xx} = M(c - u^2) \tag{3.51}$$

3.5 Boundary Conditions

In this section, the governing equations at the offshore boundary are presented. Firstly, the conditions of moving boundary at the shoreline will be described. Additionally, using the characteristic form allows derivation of the generating-absorbing boundary condition at the offshore.

3.5.1 Shoreline BCs

At the moving boundary, shoreline dynamics, i.e. shoreline position $x_s(t)$ and the associated velocity $u_s(t)$ need to be determined. The shoreline velocity u_s is obtained by the fact that both water volume flow rate $q = hu$ and water depth h approach zero at the shoreline. So, u_s can be obtained from limiting calculus, L'Hospital's rule, as in *Sobey* [2009]

$$u_s = \frac{q}{h}\Big|_{x_s} = \frac{q_x}{h_x}\Big|_{x_s} \tag{3.52}$$

Once u_s is known, x_s can be approximated from

$$x_s = \int u_s dt \tag{3.53}$$

This method is found more stable than the approach of *Brocchini et al.* [2002] and *Prasad and Svendsen* [2003]. If bed friction is included ($c_d \neq 0$), $-c_d \frac{|u|u}{h}$ needs to be balanced by h_x, else numerical problems will arise during backwash as there is no practical balance term (*Antuono et al.* [2012]). Following *Zhu and Dodd* [2013], the momentum equation is balanced by assuming $u_s = 0$ in the backwash, which means a vanishingly thin film of water develops. Instead, another solution is to impose a threshold for shoreline water depth, h_{min}, so that the term $-c_d \frac{|u|u}{h}$ does not approach infinity in this vicinity (*Zhu and Dodd* [2013]). Although the momentum equation is not applied at the shoreline node, the term $-c_d \frac{|u|u}{h}$ of adjacent node is still very large as h becomes smaller. However, since the wet region is bounded in the transformed domain, neither threshold water depth nor zero shoreline velocity is necessary in this model. It is noted that in verification tests (§ 5), h_{min} and/or $u_s = 0$ are still applied in some tests to maintain consistency with other models.

3.5.1.1 Shock conditions at shoreline boundary

The shoreline boundary condition require particular attention because bed level must now be allowed to change, but the dry bed always lies outside the computational domain. For some bed load formulae, bed-evolution at the shoreline is related to a shock condition (*Zhu and Dodd* [2013]) where bed levels on the left and on the right of the shoreline point are different. This is due to the discontinuity of velocity at the shoreline. In these cases our shoreline boundary conditions must

include shock conditions and that must be applied differently depending on either uprush or backwash stage.

As $h \to 0$ at the shoreline, $E/h \to \infty$, thus, the right hand side of (3.44) (or 3.49) is undefined ($\to \infty$) unless either $c \to c_{eq}(= u^2)$ or imposing a threshold of shoreline water depth h_{min}. In this case, we take the equilibrium state for suspended concentration $c = u_s^2$ at the shoreline (*Zhu and Dodd* [2015]). Here we exclude the effect of downslope diffusion in the boundary conditions. We use linear extrapolation when incorporating this diffusion.

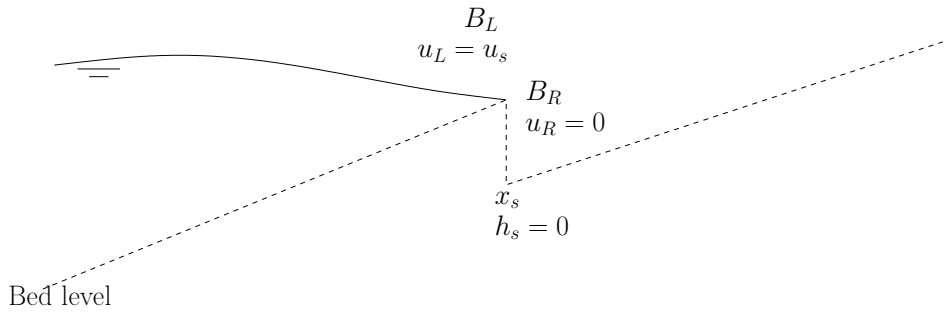


Figure 3.2: Sketch of the shock for B at the shoreline both advancing and retreating in the physical domain.

The shock at the advancing/retreating tip (see Fig. 3.2) can be defined in terms of bed-levels and velocities on the left-side (wet region) and right-side (dry region) of the shoreline: B_L, u_L and B_R, u_R. Since the dry region is also included in the bed shock relation for B at the shoreline, the solution of B at x_s can be related to that in the dry region. Following *Kelly and Dodd* [2010], the shock condition at the shoreline can be obtained by integrating across a physical region $[x_1, x_2]$ such that

$$\frac{\mathrm{d}}{dt}\int_{x_1}^{x_2} B dx + \int_{x_1}^{x_2} 3\sigma(u^2 - u_{cr,b}^2)u_x dx = \int_{x_1}^{x_2} M(c - u^2)dx \tag{3.54}$$

Assuming that $x_1 < x_s < x_2$, and in the limit of $x_1 \to x_s$ and $x_2 \to x_s$, and assuming $c_s = c_{eq} = u_s^2$, and $h_R = 0$, $u_R = 0$, $h_L = 0$ and $u_L = u_s$. (3.54) becomes

$$\begin{aligned} -u_s[B]_{x_1}^{x_2} + [\sigma(u^2 - u_{cr,b}^2)^{3/2}]_{x_1}^{x_2} = 0 \\ \Rightarrow (B_R - B_L) + \sigma(u_s^2 - u_{cr,b}^2)^{3/2} = 0 \end{aligned} \tag{3.55}$$

The shock relation for B at the shoreline is applied to compute bed level B for one side while the one on the other side is unknown. During uprush ($u_s \geq 0$), dry bed level B_R is interpolated linearly from the known bed level at the previous time-step and wet bed level B_L can be obtained from (3.55). On the other hand, during backwash ($u_s < 0$), dry bed level B_R is unknown, and in this case, bed level on the left side B_L is extrapolated linearly from the neighbouring nodes at the same time-step. Since the spatial grid size is small, the error of extrapolation is assumed negligible. Once B_L is known, B_R is then computed from (3.55).

3.5.2 Offshore BCs

Incelli et al. [2015] presented their open boundary treatment for the fully-coupled hyrdo-morphodynamical model based on NSWE-Exner equations. This allows the generation of incoming signals and absorption of the reflected ones, together with the evolution of bed level at the seaward boundary. The boundary conditions were based on linear wave theory approximations through solutions of the Riemann equations.

Absorbing-generating BCs were developed from Riemann invariants (method of characterisitcs) for hydrodynamics by *Kobayashi et al.* [1987] and *Van Dongeren and Svendsen* [1997]. Morphodynamic aspects such as suspended sediment concentration and bed level were included for a fully-coupled model by *Zhu* [2012] and

Incelli [2016]. It is noted that the BCs were applied for the frictionless case only. Additionally, no bed diffusion and infiltration were considered. It was also pointed out by *Incelli et al.* [2015] that the BCs are not suitable for large incoming wave heights as the linear wave approximations are then no longer valid. Offshore BCs for the fully-coupled model are here developed based on transformed coordinate. It is also noted that this model includes suspended sediment concentration, which was not included in *Incelli et al.* [2015]. Details of the offshore boundary conditions will be presented in the following chapter since the numerical method is part of the offshore boundary solutions.

CHAPTER 4

Numerical Solver

This chapter presents the numerical solver to simulate the coupled hydro-morphodynamical system described in § 3. The solver is motivated by a hydrodynamic model, created for investigating wave transformation, run-up within the nearshore region (see *Brocchini et al.* [2002] and *Prasad and Svendsen* [2003]). The present model uses a similar numerical approach but extending it to incorporate the suspended sediment concentration and sediment conservation equation, to make it morphodynamic. The NSWEs and morphodynamic equations are solved simultaneously in this fully-coupled hydro-morphodynamical model. This chapter gives a summary of the numerical solver, description of offshore boundary conditions and methodology to deal with the moving boundary of run-up (down) waves at the shoreline. The Shapiro filtering technique applied in this model is explained in the last section.

4.1 Coordinate Transformation Methodology

There are many problems related to the NSWE models which have been recognised by researchers (*Özkan-Haller and Kirby* [1997], *Brocchini and Dodd* [2008]). One of the most challenging problem in modelling nearshore dynamics is properly describing the free-moving boundary condition at the shoreline of domain (*Takeda* [1984], *Liu et al.* [2008]). This so-called wetting-drying problem is related to the solution over the whole domain (*Özkan-Haller and Kirby* [1997], *Prasad and Svendsen* [2003]). The challenges in wetting-drying problem are mainly because

1. The shoreline position is unknown from earlier and is a part of the solution. The computational domain is constrained by this moving boundary which requires careful integration into numerical models.

2. At the shoreline, water depth approaching zero but not velocity, which means that there do exist singular solutions of the partial differential equations (*Liu et al.* [2008]).

3. The boundary conditions of lateral and offshore also affect the accuracy of solutions. Moreover, in finite difference methods, at the shoreline, derivatives can only be obtained by one-sided representations which were implemented directly or indirectly by fictitious points combined with extrapolation (*Balzano* [1998], *Lynett et al.* [2002]). Common consequence is that the level of accuracy of the numerical method is reduced at the shoreline; and there is a production of noise, which must be controlled by filtering or dissipation (*Liu et al.* [2008]).

In numerical models, properly defining shoreline boundary condition is crucial for implementing an efficient and robust model of nearshore flows. In view of

these difficulties the performance of a wetting-drying models should be carefully assessed. The solutions of NSWEs in wetting-drying should be compared to the analytical solutions or at least compared to computational results obtained independently. In addition, grid dependence in the solution should be reported. However, it is surprising how seldom the latter is found in literature. Some of the literature that address moving shorelines focus on storm surges and tides (*Pritchard and Hogg* [2003a], *Pritchard and Hogg* [2003b] and *Liu et al.* [2008]). Such applications involve smaller gradients and longer time scales than swash motion, and are thus less challenging. The contributions of this kind often omit both testing and detailed descriptions of shoreline dynamics. So, it is difficult to evaluate the potential of such published methods on NSWEs wetting-drying and later coupling hydro-morphodynamics NSWEs.

The wetting-drying in NSWEs models consist of two parts. The first part is to describe shoreline motions which are velocity and position of the shoreline. The second part is to develop a method to incorporate the time-varying domain into the numerical model. These method can be classified into two groups. The first group consists of coordinate transformation methods in which the time dependence of computational domain is removed (see e.g. *Goto and Shuto* [1980], *Gjevik and Pedersen* [1981], *Johns* [1982], *Özkan-Haller and Kirby* [1997], *Prasad and Svendsen* [2003], *Zhou et al.* [2004]). The second group uses fixed grid methods in which the computational domain is also the physical domain and the shoreline position is tracked within this fixed physical domain (see e.g. *Balzano* [1998], *Sielecki and Wurtele* [1970], *Hibberd and Peregrine* [1979], *Titov and Synolakis* [1995], *Hubbard and Dodd* [2002], *Kelly and Dodd* [2009], *Briganti et al.* [2012a]).

For CTM models, very good performance is reported for wetting-drying of

both 1D and 2D cases (*Brocchini et al.* [2002] and *Prasad and Svendsen* [2003]). The transformation function can obtain a high resolution in the nearshore region, where the flows are dynamical in NSWEs. In fixed grid method, either a small grid size throughout the domain (see *Brocchini et al.* [2002]) or a adaptive mesh approach (*Hubbard and Dodd* [2002]) is applied to obtain high resolution. Moreover, a minimum values are prescribed in fixed grid method to determine whether a cell is wetting or drying (see *Hubbard and Dodd* [2002]). This threshold should be very small to obtain a smooth solution. The domain in fixed grid method should be able to accommodate the maximum wetting region. Compared to fixed grid method, CTM does not require such threshold but still obtains smooth solutions of hydrodynamics and shoreline motion (see *Brocchini et al.* [2002]). For the same spatial grid size, the solution obtained by CTM is more accurate than by fixed grid method under the same numerical scheme (see *Brocchini et al.* [2002] for detailed comparison). A widely accepted weakness of CTM is strong grid deformation that may occur in demanding applications such as breaking waves in swash motion. For long, non-breaking waves such as tidal motion, this method is suitable to deal with the difficulties of wetting-drying and obtain smooth solutions in the vicinity of the shoreline while requiring less computational effort compared to fixed grid methods (*Özkan-Haller and Kirby* [1997] and *Prasad and Svendsen* [2003]).

We implement the CTM method developed by *Prasad and Svendsen* [2003] as the treatment of moving shoreline boundary, and incorporate it into our morpho-hydro coupled model. The main reason is their transformation equations are adequate to obtain a better grid resolution in the nearshore region but do not require a second transformation as *Özkan-Haller and Kirby* [1997]. We

choose to develop this technique to cope with the moving boundary problem; and extend it further into hydro-morphodynamic coupled model to investigate the morphodynamics of sandy beaches under pure macro-tidal motion. It is noted that CTM have never been attempted before in fully coupled model with the morphodynamic equations included. It allows us to verify the CTM in coupled model and investigate how well the solution obtained by CTM compared to existing models in fixed grid method.

The definition sketch of both physical and computational domains is shown in Fig. 4.1. Wet region of the physical domain is bounded by a moving shoreline position $L + x_s$, where L is the physical domain length at $t = 0$ and also the computational domain length and x_s is the shoreline position with respect to the original position at $t = 0$.

The transformation equations are used so that the instantaneous physical domain always corresponds to fixed computational domain, i.e. without a moving boundary. Following *Johns* [1982], *Özkan-Haller and Kirby* [1997], *Brocchini et al.* [2002] and *Prasad and Svendsen* [2003], the physical domain is transformed into computational domain by applying the transformation

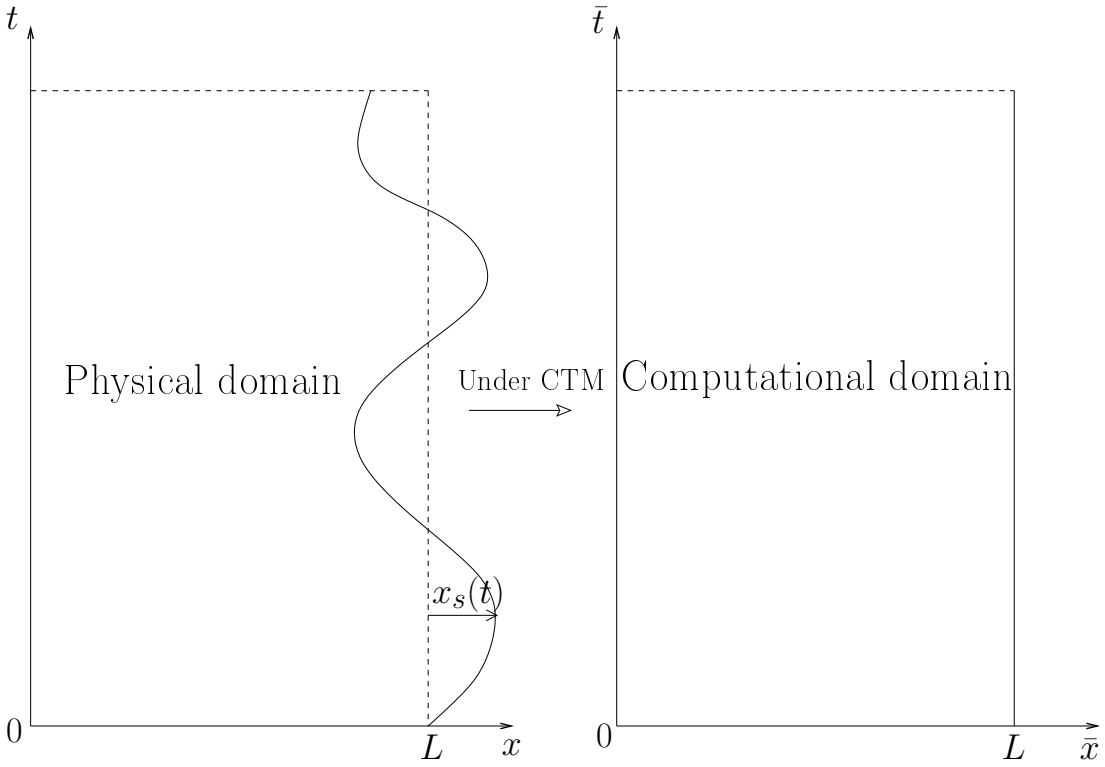


Figure 4.1: Transformation from moving physical to fixed computational domain.

$$x = g(\overline{x}) + x_s(\bar{t}) f(\overline{x}) \tag{4.1}$$

$$t = \bar{t} \tag{4.2}$$

Equations (4.1) and (4.2) map (x, t) onto computational coordinates $(\overline{x}, \bar{t})$ such that the transformed domain is defined from $\overline{x} = 0$ (offshore) to $\overline{x} = L$ (shoreline) for $0 < \bar{t} < \infty$. The conditions for $f(\overline{x})$ and $g(\overline{x})$ to maintain the coincidence of both domains are

$$\overline{x} = 0 \qquad \Rightarrow \qquad x = 0 \tag{4.3}$$

$$\overline{x} = L \qquad \Rightarrow \qquad x = L + x_s(t) \tag{4.4}$$

which implies that

$$f(\overline{x}=0)=0 \qquad \text{and} \qquad g(\overline{x}=0)=0 \tag{4.5}$$

$$f(\overline{x}=L)=1 \qquad \text{and} \qquad g(\overline{x}=L)=L \tag{4.6}$$

It is also desirable that a higher grid resolution is achieved in the nearshore other than in the offshore region as more rapid changes typically take place there. Following *Brocchini et al.* [2002] and *Prasad and Svendsen* [2003], this can be achieved by taking

$$f(\overline{x})=\frac{\exp[-\alpha(L-\overline{x})]-\exp(-\alpha L)}{1-\exp(-\alpha L)} \tag{4.7}$$

$$g(\overline{x})=0.5\overline{x}-\frac{1}{\beta}\ln\{\cosh[\beta(L-\overline{x})]\}+0.5L \tag{4.8}$$

where α and β are coefficients.

By carefully selecting the transformation functions $f(\bar{x})$ and $g(\bar{x})$, a higher resolution in the vicinity of the shoreline can be achieved. $\Delta x/\Delta\bar{x}$ is the ratio of physical cell versus computational cell. For higher resolution in the nearshore, a value of $\Delta x/\Delta\bar{x}<1$ is desirable in that vicinity. Moreover, the condition of grid size distribution $\Delta x/\Delta\bar{x}>0$ must be maintained throughout the domain. Applying this condition to (4.5) and (4.6), yields

$$0<\alpha<\frac{0.5}{|x_s(t)|_{max}} \tag{4.9}$$

$$\beta=\frac{2\ln[\cosh(\beta L)]}{L} \tag{4.10}$$

in which, β can be solved numerically by Newton-Raphson method as a function of L. From the condition given in (4.9), the fixed value of $\alpha=0.01$ is used in simulations unless stated otherwise.

Under CTM, governing equations (3.42) - (3.45) for swash motions become

$$h_{\bar{t}} + A_1 h_{\bar{x}} + A_2 (hu)_{\bar{x}} = 0 \tag{4.11}$$

$$u_{\bar{t}} + A_1 u_{\bar{x}} + A_2 u u_{\bar{x}} + A_2 h_{\bar{x}} + A_2 B_{\bar{x}} = -c_d \frac{|u|\, u}{h} \tag{4.12}$$

$$c_{\bar{t}} + A_1 c_{\bar{x}} + A_2 u c_{\bar{x}} = \frac{1}{h} E(u^2 - c) \tag{4.13}$$

$$B_{\bar{t}} + A_1 B_{\bar{x}} + 3\sigma A_2 (u^2 - u_{cr,b}^2) u_{\bar{x}} = M(c - u^2) \tag{4.14}$$

while (3.47)-(3.50) for tidal motions are transformed as

$$h_{\bar{t}} + A_1 h_{\bar{x}} + A_2 (hu)_{\bar{x}} = 0 \tag{4.15}$$

$$u_{\bar{t}} + A_1 u_{\bar{x}} + A_2 u u_{\bar{x}} + A_2 \frac{1}{F^2} (h + B)_{\bar{x}} = -C_D \frac{|u|\, u}{h} \tag{4.16}$$

$$c_{\bar{t}} + A_1 c_{\bar{x}} + A_2 u c_{\bar{x}} = \frac{1}{h} E(u^2 - c) \tag{4.17}$$

$$B_{\bar{t}} + A_1 B_{\bar{x}} + 3\sigma A_2 (u^2 - u_{cr,b}^2) u_{\bar{x}} = M(c - u^2) \tag{4.18}$$

where A_1 and A_2 are defined as

$$A_1(\overline{x}, \bar{t}) = \frac{\partial \overline{x}}{\partial t} = -\left\{ \frac{1}{g'(\overline{x}) + x_s(\bar{t}) f'(\overline{x})} \right\} u_s(\bar{t}) f(\overline{x}) \tag{4.19}$$

$$A_2(\overline{x}, \bar{t}) = \frac{\partial \overline{x}}{\partial x} = \frac{1}{g'(\overline{x}) + x_s(\bar{t}) f'(\overline{x})} \tag{4.20}$$

where $u_s = \frac{\mathrm{d}x_s}{\mathrm{d}\bar{t}}$ is velocity of the shoreline. If downslope diffusion is included, i.e. (3.51) is considered instead of (3.45) (or (3.50)), the bed change evolution (4.14) (or (4.18)) becomes

$$B_{\bar{t}} + A_1 B_{\bar{x}} + A_2 \sigma \left\{ 3(u^2 - u_{cr,b}^2) u_{\bar{x}} - \frac{3(u^2 - u_{cr,b}^2)}{\tan\phi} u_{\bar{x}} (\Delta B)_{\bar{x}} - \frac{(u^2 - u_{cr,b}^2)^{1.5}}{\tan\phi} (\Delta B)_{\bar{x}\bar{x}} \right\} = M(c - u^2) \tag{4.21}$$

4.2 Boundary Conditions

The shoreline boundary conditions have been presented in § 3.5. Here we only illustrate how the offshore boundary conditions are obtained in conjunction with

CTM (for the details of offshore boundary conditions in physical domain, see *Kobayashi et al.* [1987], *Incelli et al.* [2015])

Governing equations in CTM for swash motion (4.11)-(4.14) is rewritten in a vector form of:

$$\boldsymbol{X}_{\bar{t}} + \boldsymbol{W}(\boldsymbol{X})\boldsymbol{X}_{\bar{x}} = \boldsymbol{S} \tag{4.22}$$

where

$$\boldsymbol{X} = \begin{bmatrix} h \\ u \\ c \\ B \end{bmatrix}$$

$$\boldsymbol{W}(\boldsymbol{X}) = \begin{bmatrix} A_1 + A_2 u & A_2 h & 0 & 0 \\ A_2 & A_1 + A_2 u & 0 & A_2 \\ 0 & 0 & A_1 + A_2 u & 0 \\ B & 3\sigma A_2 u^2 & 0 & A_1 \end{bmatrix}$$

$$\boldsymbol{S} = \begin{bmatrix} 0 \\ -c_d \frac{|u|u}{h} \\ \frac{E}{h}(u^2 - c) \\ M(c - u^2) \end{bmatrix}$$

It is note that $A_1 = 0$ at offshore ($\bar{x} = 0$) and $\boldsymbol{W}$ can be simplified. The eigenvalues of $\boldsymbol{W}$ of swash motion are the roots of the polynomial

$$(\lambda - A_2 u)\Big\{\lambda^3 - 2A_2 u\lambda^2 + (A_2^2 u^2 - 3\sigma A_2^2 u^2 - A_2^2 h)\lambda + 3\sigma A_2^3 u^3\Big\} = 0 \tag{4.23}$$

Similarly, the vector form of tidal motion are the same as swash, except for

$\boldsymbol{W}$ and $\boldsymbol{S}$, i.e.

$$\boldsymbol{W}(\boldsymbol{X}) = \begin{bmatrix} A_1 + A_2 u & A_2 h & 0 & 0 \\ \frac{A_2}{F^2} & A_1 + A_2 u & 0 & \frac{A_2}{F^2} \\ 0 & 0 & A_1 + A_2 u & 0 \\ B & 3\sigma A_2 u^2 & 0 & A_1 \end{bmatrix}$$

$$\boldsymbol{S} = \begin{bmatrix} 0 \\ -C_D \frac{|u|u}{h} \\ \frac{E}{h}(u^2 - c) \\ M(c - u^2) \end{bmatrix}$$

The eigenvalues of $\boldsymbol{W}$ of tidal motion are the roots of the polynomial

$$(\lambda - A_2 u)\Big\{\lambda^3 - 2A_2 u\lambda^2 + (A_2^2 u^2 - 3\sigma\frac{A_2^2}{F^2}u^2 - \frac{A_2^2}{F^2}h)\lambda + 3\sigma\frac{A_2^3}{F^2}u^3\Big\} = 0 \quad (4.24)$$

The polynomial (4.23) (or (4.24)) has four roots λ_k (with $k = 1, 2, 3, 4$), one of which is $\lambda_4 = A_2 u$ corresponding to the transport of suspended sediment in the computational domain. It is noted that here we only derive the solution of tidal motion. However, the solution of swash motion is similar with only exception of not including Froude number F (see *Incelli et al.* [2015] for more details). The cubic equation in curly brackets in (4.24) can be solved directly using Cardano's formula (see *Kelly and Dodd* [2009], *Zhu* [2012] and *Incelli et al.* [2015]) and the solutions are:

$$\lambda_1 = 2(-Q)^{\frac{1}{2}} \cos(\frac{\Theta + 2\pi}{3}) - \frac{a_2}{3} \quad (4.25)$$

$$\lambda_2 = 2(-Q)^{\frac{1}{2}} \cos(\frac{\Theta}{3}) - \frac{a_2}{3} \quad (4.26)$$

$$\lambda_3 = 2(-Q)^{\frac{1}{2}} \cos(\frac{\Theta + 4\pi}{3}) - \frac{a_2}{3} \quad (4.27)$$

where

$$Q = \frac{3a_1 - a_2^2}{9}$$
$$R = \frac{9a_1a_2 - 27a_0 - 2a_2^3}{54}$$
$$\Theta = \cos^{-1}\left(\frac{R}{(-Q)^{3/2}}\right)$$

and a_0, a_1 and a_2 are the coefficient terms of the cubic polynomial,

$$a_0 = 3\sigma\frac{A_2^3}{F^2}u^3$$
$$a_1 = A_2^2u^2 - 3\sigma\frac{A_2^2}{F^2}u^2 - \frac{A_2^2}{F^2}h$$
$$a_2 = -2A_2u$$

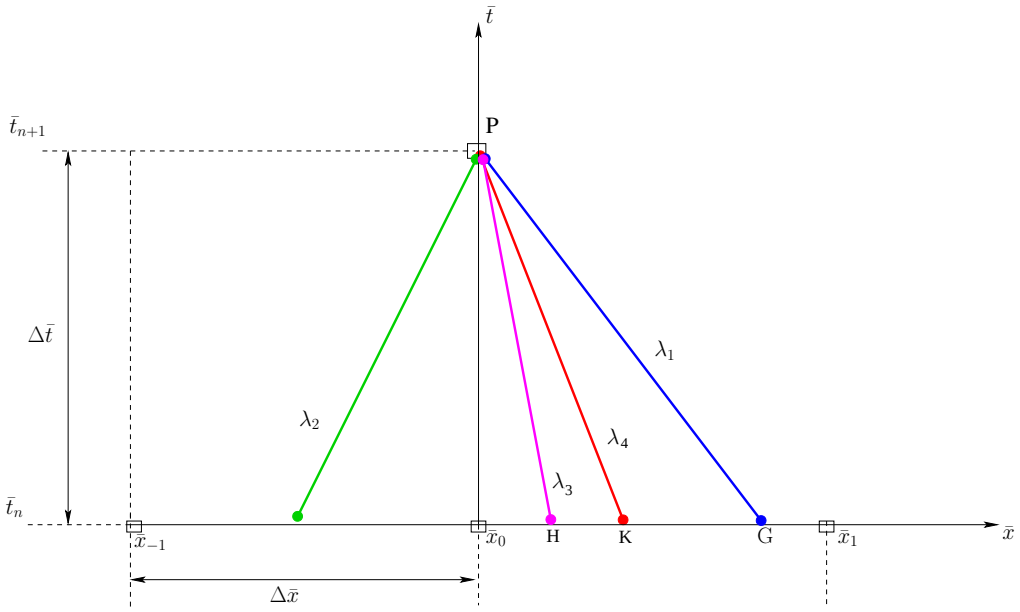


Figure 4.2: Sketch of the fully-coupled offshore BCs in the computational domain ($u < 0$). The squares indicate the nodes where the variables are obtained.

It is noted that $\lambda_1 \leq \lambda_3 \leq \lambda_2$. Similar to *Kelly* [2009] and *Zhu* [2012], at $\bar{x} = 0$, λ_1 is always negative while λ_2 is always positive. λ_3 and λ_4 are positive if $u > 0$

and vice versa. It is also noted that when $u > 0$, $\lambda_1 \leq \lambda_3 \leq \lambda_4 \leq \lambda_2$; when $u < 0$, $\lambda_1 \leq \lambda_4 \leq \lambda_3 \leq \lambda_2$. It is assumed that the flow at offshore boundary is subcritical so that the linear waves theory can be applied (*Kobayashi et al.* [1987]). The offshore boundary is located at the node $j = 0$, corresponding to $\bar{x} = 0$ and the information carried by characteristics is illustrated in Fig 4.2.

Following *Özkan-Haller and Kirby* [1997], at the offshore boundary water depth and velocity are given by sumperimposing the incoming and outgoing signals

$$h(0,\bar{t}) = h(0,0) + B(0,0) - B(0,\bar{t}) + \eta_i(0,\bar{t}) + \eta_r(0,\bar{t}) \tag{4.28}$$

$$u(0,\bar{t}) = u_i(0,\bar{t}) + u_r(0,\bar{t}) \tag{4.29}$$

where initial water depth $h(0,0)$ is assumed to be still water.

$$u_i(0,\bar{t}) = \frac{\eta_i(0,\bar{t})}{\sqrt{h(0,0) - B(0,\bar{t})}} \tag{4.30}$$

$$u_r(0,\bar{t}) = -\frac{\eta_r(0,\bar{t})}{\sqrt{h(0,0) - B(0,\bar{t})}} \tag{4.31}$$

where η is the perturbation of water surface level from the initial level, i.e. the summation of both incident u_i and reflected u_r signals. $\eta_i(0,\bar{t})$ is imposed, while $\eta_r(0,\bar{t})$, u_i and u_r are unknown. The proposed methodology is used to determine the values of these unknowns at the boundary. $B(0,0) = 0$ so that (4.28) can be simplified. Following *Zhu* [2012], the generic Riemann equation by means of (4.11) - (4.14) is written as

$$\lambda_k \frac{du}{d\bar{t}} + \frac{\lambda_k}{\lambda_k - u}\frac{dh}{d\bar{t}} + \frac{dB}{d\bar{t}} = -\lambda_k C_D \frac{|u|\,u}{h} + M(c - u^2) \qquad \text{along} \qquad \frac{d\bar{x}}{d\bar{t}} = \lambda_k \tag{4.32}$$

$$\frac{dc}{d\bar{t}} = \frac{E}{h}(u^2 - c) \qquad \text{along} \qquad \frac{d\bar{x}}{d\bar{t}} = \lambda_4 = A_2 u \tag{4.33}$$

where $\frac{d.}{dt}$ is the total derivative and λ_k (for $k = 1, 2, 3$) are the eigenvalues of the Jacobian matrix $\boldsymbol{W}$. As can be seen from Fig (4.2), the variables at current time level n are known while those at time level $n + 1$ need to be solved. Point P is located at the offshore boundary, $j = 0$, and at time level $n + 1$, where dependent variables h, u, c and B require updating. The characteristic $\lambda_k > 0$ carries information in the direction $+\bar{x}$ and vice versa. Therefore, for $\lambda_k > 0$, information from outside the domain is required for specifying variables. The values of $\lambda_{1,3,4}$ characteristics originate from the interior domain at points G, H and K, respectively and pass through point P at time level n. Although spatial coordinates of G, H and K are unknown, they are always located between 2 adjacent nodes ($j = 0$ and $j = 1$ if $\lambda_k < 0$; $j = -1$ (outside domain) and $j = 0$ if $\lambda_k > 0$). It is also noted that λ_1 is always negative, thus information is carried from inside the domain; while λ_2 is always positive, and information is carried from outside the domain. $\lambda_{3,4}$ only carries information from inside the domain if $u < 0$. The information carried by Riemann equations for $k = 1, 3, 4$ are used to determined the unknowns B_P, $\eta_{r,P}$ and c_P. At a given time level, the eigenspeed values and variables are assumed to be continuous in space so that linear interpolation error can be considered negligible. It is also noted that λ_4 is linearly degenerated in characteristic form (see (4.33)).

Following *Incelli et al.* [2015], the procedure for obtaining offshore boundary are:

1. Estimate $\bar{x}_G$, $\bar{x}_H$, $\bar{x}_K$ from $\frac{D\bar{x}}{Dt} = \lambda_{1,3,4}$ by iterative method (see *Incelli et al.* [2015] for more details)

2. Once G, H, K are located, dependent variables at these points are determined h_G, u_G, B_G and c_G are obtained by linear interpolation from node

0 and 1 while $h_{H(K)}$, $u_{H(K)}$, $B_{H(K)}$ and $c_{H(K)}$ are obtained by either linear interpolation (if $\lambda_{3,4} < 0$) or linear extrapolation (if $\lambda_{3,4} > 0$). The error related to interpolation or extrapolation is assumed negligible since the flow is subcritical and variables are continuous in space. The eigenvalues $\lambda_{1,3,4}$ at these points are also determined ((4.25)-(4.27)).

3. The Riemann equations for $\lambda_{1,3,4}$ in (4.32) and (4.33) can be rewritten in Euler difference form as

$$(B_P - B_j) + \mu_{k,j}(h_P - h_j) + \lambda_{k,j}(u_P - u_j) = -\lambda_{k,j}\frac{(\Delta\bar{t})C_D\,|u_j|\,u_j}{h_j} + \Delta\bar{t}M(c_j - u_j^2) \tag{4.34}$$

$$c_P - c_K = \frac{(\Delta\bar{t})E}{h_K}(u_K^2 - c_K) \tag{4.35}$$

where

$$\mu_{k,j} = \frac{\lambda_{k,j}}{\lambda_{k,j} - u_j}$$

with $(k, j) = (1, G)$ or $(3, H)$. (4.34) can be rearranged in the form of a system of two equations

$$B_P + \mu_{k,j}h_P + \lambda_{k,j}u_P = S_j \tag{4.36}$$

where

$$S_j = B_j + \mu_{k,j}h_j + \lambda_{k,j}\left[u_j - \frac{(\Delta\bar{t})c_d\,|u_j|\,u_j}{h_j}\right] + \Delta\bar{t}M(c_j - u_j^2)$$

Subtracting the two equations of (4.36) to eliminate B_P forms

$$\mu h_P + \lambda u_P = S \tag{4.37}$$

where

$$\mu = \mu_{1,G} - \mu_{3,H}$$

$$\lambda = \lambda_{1,G} - \lambda_{3,H}$$

$$S = S_G - S_H$$

Substituting (4.28)-(4.31) into (4.36) and (4.37) and letting $h(0,0)_P = h_{ini}$ yields

$$B_P + \mu_{1,G}(h_{ini} - B_P + \eta_{i,P} + \eta_{r,P}) + \frac{\lambda_{1,G}}{h_{ini} - B_P}(\eta_{i,P} - \eta_{r,P}) = S_G \quad (4.38)$$

$$\mu(h_{ini} - B_P + \eta_{i,P} + \eta_{r,P}) + \frac{\lambda}{h_{ini} - B_P}(\eta_{i,P} - \eta_{r,P}) = S \quad (4.39)$$

Set $\Omega = \sqrt{h_{ini} - B_P}$ so Ω must be a real value, rearranging (4.39) yields

$$\eta_{r,P} = \eta_{i,P} + \Omega\frac{S - \mu(\Omega^2 + 2\eta_{i,P})}{\Omega\mu - \lambda} \quad (4.40)$$

and substituting into (4.38) gives a cubic polynomial equation of Ω

$$\Omega^3 + \{\frac{\lambda - \mu_{1,G}\lambda + \mu\lambda_{1,G}}{-\mu}\}\Omega^2 + \{\frac{\mu h_{ini} + \mu_{1,G}S - \mu S_G}{-\mu}\}\Omega$$

$$+ \{\frac{\lambda S_G - \lambda_{1,G}S - \lambda h_{ini} + 2\eta_{i,P}(\mu\lambda_{1,G} - \mu_{1,G}\lambda)}{-\mu}\} = 0 \quad (4.41)$$

4. (4.41) are solved directly using Cardano's formula (see (4.25) - (4.27) for details) to obtain three solutions of Ω. In case there is more than one real root, B_P obtained will be compared with the known B_P at time level n and the closest value of B_P will be used as the boundary bed level at new time level $n+1$.

5. Once Ω is known, $\eta_{r,P}$ is computed from (4.40) and the dependent variables at the offshore boundary are updated by means of (4.28)-(4.31)

6. (4.35) is solved directly to obtain value of concentration at P.

$$c_P = c_K + \frac{(\Delta\bar{t})E}{h_K}(u_K^2 - c_K) \tag{4.42}$$

7. Following *Incelli et al.* [2015], further iterations can be applied to converge variables at the offshore boundary. This can be done by averaging the computed $\lambda_{k,P}$ and other variables with previously estimated ones at point G and H. Similarly, iterative process can be applied to RHS of (4.42) by averaging variables of point P and K. Steps 3-7 are repeated iteratively until a specified tolerance is achieved.

4.3 Numerical Solver and Shapiro Filtering

Equations (4.11)-(4.14) are solved numerically in the transformed computational domain. Note that the transformed equations include nonlinear terms $A_1(\overline{x}, \bar{t})$ and $A_2(\overline{x}, \bar{t})$. A finite difference scheme of spatial derivatives in conjunction with an explicit time-stepping scheme are applied to solve for unknown variables.

The computational domain is discretised spatially into $N+1$ nodes with node order from $j = 0$ (offshore) to $j = N$ (shoreline). The spatial derivatives for central nodes $j = 2$ to $j = N - 2$ are computed using a fourth order central difference approximation

$$\left.\frac{\partial X}{\partial \overline{x}}\right|_{j=2-(N-2)} = \frac{1}{12\Delta\overline{x}}\Big\{X_{j-2} - 8X_{j-1} + 8X_{j+1} - X_{j+2}\Big\} + O(\Delta\overline{x}^4) \tag{4.43}$$

where $\Delta\overline{x}$ is the computational spatial grid size, X represents any dependent variable and j is the spatial node at which the derivative is calculated. For nodes adjacent to the boundary, $j = 1$ and $j = N - 1$, a second order central difference

approximation is used

$$\left.\frac{\partial X}{\partial \overline{x}}\right|_{j=1,N-1} = \frac{1}{2\Delta\overline{x}}\Big\{ - X_{j-1} + X_{j+1}\Big\} + O(\Delta\overline{x}^2) \tag{4.44}$$

At the boundary node $j = 0$ and $j = N$, the spatial derivative is approximated by a one-sided second order approximation, i.e.

$$\left.\frac{\partial X}{\partial \overline{x}}\right|_{j=0} = \frac{1}{2\Delta\overline{x}}\Big\{ - 3X_j + 4X_{j+1} - X_{j+2}\Big\} + O(\Delta\overline{x}^2) \tag{4.45}$$

$$\left.\frac{\partial X}{\partial \overline{x}}\right|_{j=N} = \frac{1}{2\Delta\overline{x}}\Big\{X_{j-2} - 4X_{j-1} + 3X_j\Big\} + O(\Delta\overline{x}^2) \tag{4.46}$$

Given the initial conditions and boundary conditions, the governed NSWEs in the computational domain are integrated in time using an Adams-Bashforth-Moulton predictor-corrector scheme. Equations (4.11)-(4.14) (or (4.15)-(4.18)) can be written in the form

$$X_{\bar{t}} = F \tag{4.47}$$

A second order Adams-Bashforth scheme is applied for prediction, while a third order Adams-Moulton scheme is used iteratively for correction of predicted variables X at the next time-step.

$$X^{n+1}_{Predictor} = X^n + \frac{\Delta\bar{t}}{2}\Big\{3F^n - F^{n-1}\Big\} \tag{4.48}$$

$$X^{n+1}_{Corrector} = X^n + \frac{\Delta\bar{t}}{12}\Big\{5F^{n+1}_{Predictor} + 8F^n - F^{n-1}\Big\} \tag{4.49}$$

It is noted that an apparently non-physical oscillation occurs in this scheme and also in other schemes (*Van Dongeren and Svendsen* [1997], *Özkan-Haller and Kirby* [1997]). It appears to originate at the vicinity of shoreline, $\bar{x} = L$. The cause of this behaviour is unknown but it is noted that *Özkan-Haller and Kirby* [1997] observed similar behaviour. Here we treat it the same way by using a numerical filter technique developed by *Shapiro* [1970]. The filter is applied

after every 100 time-steps to prevent spurious growth and avoid model instability. Moreover, the decentred Shapiro filter method developed by *Falissard* [2015] also allows boundary filtering as well as centred filtering of the original Shapiro filter. For a computational domain of $N+2$ nodes, nodes $i=4$ to $N-1$ are filtered using the 16^{th}-order Shapiro filter:

$$F^{16}(X_i) = \frac{1}{256}\Big(-(X_{i-4}+X_{i+4}) + 8(X_{i-3}+X_{i+3}) - 28(X_{i-2}+X_{i+2}) \\ +56(X_{i-1}+X_{i+1}) + 186X_i\Big) \quad (4.50)$$

Near the boundaries, a non-symmetric filter is used as mentioned. Accordingly, at nodes $i=1,2,3,N-2,N-1,N$, the decentred 16^{th}-order Shapiro filter is applied following *Falissard* [2015]. The variables at boundary $i=0$ and $i=N+1$ remain unchanged. The details of CTM model and numerical solver can also be found in *Huynh et al.* [2017].

4.4 Numerical scheme development

In this section, the initial model development stages are presented. We initially focus on the hydrodynamic NSWE. We applied two different time integration numerical schemes in conjunction with spatial finite difference approximation, without filtering. Results are verified against *Carrier and Greenspan* [1958] transient solutions. The descriptions of this verification test are given in the following chapter.The Adam-Moulton scheme is presented above, namely explicit scheme. Another time-integration scheme is Crank-Nicholson, namely implicit scheme. Details of Crank-Nicholson scheme can be found in *Smith* [1985] and *Pedrozo-Acuna* [2013].

Both schemes show good agreement at some initial stage but quickly diverge no matter what scheme is used and how small the Courant number is. An apparently non-physical oscillation occurs in both scheme and appears to originate in the vicinity of the shoreline. The performance of both schemes against *Carrier and Greenspan* [1958] transient solutions are shown in Fig. 4.3 (shoreline position) and Fig. 4.4 (shoreline velocity). In the same grid sizes, the explicit scheme obtained better results compared to implicit one. The latter scheme becomes unstable at $t = 1.5$; while the former scheme is unstable at $t = 3$ (not shown in current scale). Additionally, the error in the implicit scheme is magnified earlier and higher than the explicit one. This is why we choose explicit scheme as model numerical solver.

The errors in both schemes are magnified and the model becomes unstable. However, the explicit scheme obtain higher accuracy compared to the implicit one, because a higher order finite difference approximation is easier to be implemented in the former one than the latter. Unstable behaviour of both model also points out that implicit or explicit scheme is not the reason of this numerical oscillation. This numerical error seems to be due to an apparently non-physical oscillation, which must be controlled by a low-pass filtering (see also *Van Dongeren and Svendsen* [1997] and *Özkan-Haller and Kirby* [1997]). This instability is successfully controlled by the low-pass filtering such as that developed by *Shapiro* [1970].

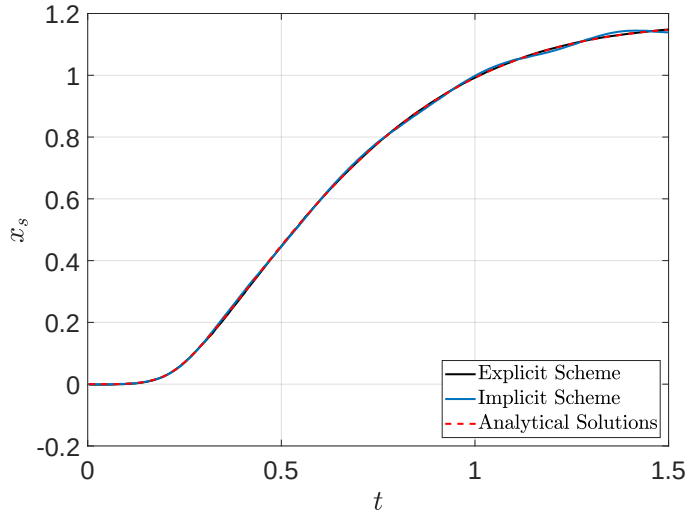


Figure 4.3: *Carrier and Greenspan* [1958] transient solution of x_s vs. t of Explicit scheme (black) and Implicit scheme (blue) without filtering. CG58 solutions: red dashed.

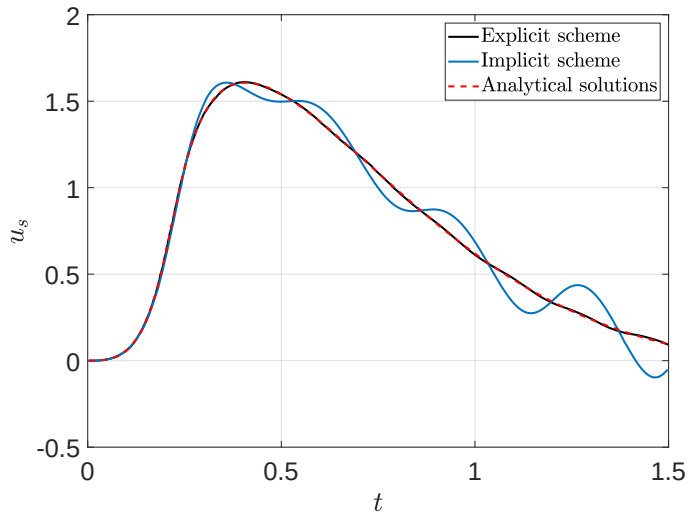


Figure 4.4: *Carrier and Greenspan* [1958] transient solution of u_s vs. t of Explicit scheme (black) and Implicit scheme (blue) without filtering. CG58 solutions: red dashed.

Later, we apply the filtering technique, developed by *Shapiro* [1970] and successfully applied by *Özkan-Haller and Kirby* [1997] in CTM. In order to determine at what degree and what frequency, the filter is applied, we test the filtering technique against *Carrier and Greenspan* [1958] periodic solutions. The numerical solutions are filtered at different frequencies (Fig. 4.5). It is obvious that the filter has successfully eliminated non-physical oscillation and maintained model's stability. It is also clear that the filter does not need to be applied at every time-step or many times consecutively. For filter applied after every period and once, the solutions has similar accuracy as applying filter at every time-step. Thus, we choose to execute filtering once after every cycle (for periodic events such as tidal waves) or every 100 time-steps (for single events such as single swash).

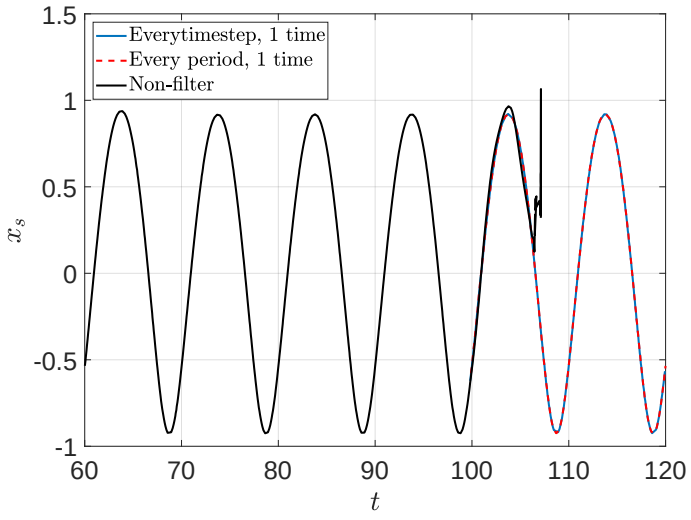


Figure 4.5: Filter test for CG58 periodic test.

CHAPTER 5

Verification Tests

In this chapter, the model is verified against both analytical and numerical results. Following model development stages, the present model will firstly be verified against NSWE hydrodynamics only for fixed bed. Secondly, the advection of suspended sediment concentration equation is considered and verified on a fixed bed. Finally, the performance of fully-coupled model on an erodible bed under either bed load or suspended load transport is verified. The simulation on a fixed bed allows hydrodynamic solutions to be verified against the analytical benchmark of *Carrier and Greenspan* [1958] and *Shen and Meyer* [1963] and the numerical benchmark of *Hubbard and Dodd* [2002]. Performance at the offshore boundary is also investigated through some simple tests. When exact solutions for the fully-coupled model are not available, model results are compared with other numerical solutions obtained by different solvers (*Zhu and Dodd* [2013], *Zhu and Dodd* [2015] and *Dodd et al.* [2008]). These verification cases are mostly developed for swash motion, with the only exception of the test for

tidal motion developed by *Pritchard and Hogg* [2003a] to obtain cohesive sediment concentration on a fixed bed. In another work, they also developed from the same framework to investigate the behaviour for swash motion (*Pritchard and Hogg* [2003b]). Since the hydrodynamics on these tests are those of the NSWEs, we verified against both tests to see the model performance in different type of NSWEs motions. These verification tests allow us to focus on different aspects of the coupled problem and analyse model behaviour to different cases. It is noted that the present model is verified mainly against swash dynamics cases. There are many verification tests for fully coupled model available for the swash rather than tidal motion, and these are often more demanding than those for the equivalent tidal problems.

This chapter is divided into three sections, one for each aspect considered, which also reflects the development stage of this model into fully-coupling. The description of test cases and reason why they are useful for verification purposes will be presented briefly at the beginning of each relevant section.

1. Hydrodynamics-only tests
2. Advection of suspended sediment concentration tests
3. Fully-coupling hydro-morphodynamics tests

5.1 Hydrodynamics only

By setting E, M and σ at zero, the bed is made immobile and the model solutions are compared with hydrodynamic analytical solutions of *Carrier and Greenspan* [1958] and *Shen and Meyer* [1963]. NSWEs models in the nearshore region are associated with wetting and drying of a beach. This is only part of a more

complex problem, which may include breaking or non-breaking waves (see *Liu et al.* [2008]). The tidal motions are considered non-breaking. In non-breaking NSWEs regime, there are some available analytical solutions that can be used for verification. *Carrier and Greenspan* [1958] presented their nonlinear, analytical solutions of the NSWEs equations for runup on an inclined plane. Among their explicit solutions were the nonlinear generalisation of the standing wave, as well as an initial value problem for runup. The main purpose of these verification tests is to see how well the model performs in a single NSWEs runup event (transient solutions of *Carrier and Greenspan* [1958]) and multiple NSWEs wetting-drying events (periodic solutions of *Carrier and Greenspan* [1958]). Furthermore, the model robutness over a long-term simulation can be verified against the periodic solutions of *Carrier and Greenspan* [1958]. Their periodic solutions are somehow similar to the periodic variation of tidal motion. The inclusion of bed shear stress can be verified against the numerical solutions of *Hubbard and Dodd* [2002].

The model behaviour for a highly dynamic case such as single swash event of *Shen and Meyer* [1963] is also verified. The reason for including this verification is due to limitation of the numerical results available for tidal fully-coupled model. However, there are some fully-coupled models available in considering the morphodynamics under *Shen and Meyer* [1963] swash event (see *Pritchard and Hogg* [2005], *Kelly and Dodd* [2009], *Zhu and Dodd* [2013], *Zhu and Dodd* [2015]). In this swash event, there is no shock developed subsequently in the fixed bed case, thus the non-breaking regime can be accommodated. Discontinuity of the flow only occurs during backwash for mobile bed in some particular cases, which is not considered in these verification tests (*Zhu and Dodd* [2013] and *Zhu and Dodd* [2015]). So, for further model verifications when the morphodynamic

equations are included, we also verify the hydrodynamics of *Shen and Meyer* [1963] swash event.

5.1.1 *Carrier and Greenspan* [1958] solutions

Carrier and Greenspan [1958] introduced a hodograph transformation so that the NSWEs were expressed in terms of independent coordinates (σ, λ) instead of the physical ones (x, t). Hereinafter, we use χ to denote *Carrier and Greenspan* [1958] σ to avoid confusion with the present use of σ (bed mobility under bed load transport). Under the hodograph transformation, the results obtained at $\chi = 0$ represent flow properties at the shoreline. *Carrier and Greenspan* [1958] described their solutions as an initial value problem and in standing wave form. These are two well-known analytical solutions of NSWEs hydrodynamic, so-called transient and periodic solutions, respectively.

5.1.1.1 *Carrier and Greenspan* [1958] transient solutions

Carrier and Greenspan [1958] transient case is the analytical solution for a body of fluid that is initially depressed (with respect to the still water level) and held motionless ($u = 0$), then released at $t = 0$. The generated transient wave runs up the plane beach and allows us to see the model performance on the run-up problem. Because the case is transient, it allows us to ignore the offshore boundary by taking the domain far enough away so that its influence can be neglected. The initial surface elevation η versus x is shown in Fig.5.1 and given analytically by *Carrier and Greenspan* [1958]. They introduce a parameter ε related to depression of the initial surface elevation profile. A value of $\varepsilon \leq 0.23$ needs to be selected for non-breaking cases. The initial surface elevation η approaches asymptotically ε

far offshore, and reaches its minimum value of 0 at the shoreline. The analytical solutions are obtained in (χ, λ)-coordinates (see formulas (3.4) - (3.9) in *Carrier and Greenspan* [1958]). The motion of instantaneous shoreline was obtained by setting $\chi = 0$ (see formulas (3.10) - (3.13) in *Carrier and Greenspan* [1958]).

The present model is tested against the transient case with $L = 50$, slope $= 1/50$, $\Delta\bar{x} = 0.1$, $\Delta\bar{t} = 0.01$, $\alpha = 0.01$, $\beta = 0.024375$, and $\varepsilon = 0.1$. There are 500 nodes across the domain and the model simulation is over a time duration of 100. There is no incident wave prescribed, allowing a fully absorbing offshore boundary condition. By comparing against analytical solutions at the offshore boundary, the performance of offshore boundary conditions is also investigated.

The analytical results and model results show excellent agreement in both Fig. 5.1 and 5.2. In Fig. 5.2, a very small difference in u_s can be seen between model and analytical results, as u_s approaches its maximum value. The simulation time is extended to allow waves to exit the domain so that offshore signals of η and u can be compared with analytical solutions. The solutions of absorbing offshore boundary shown in Fig. 5.3 exhibit some discrepancies, which shows inability of the offshore boundary to fully absorb the outgoing waves. The errors can be observed clearly around $t = 350$ when the reflected wave reach the offshore boundary. Performance of the offshore boundary is further investigated quantitatively in the following section.

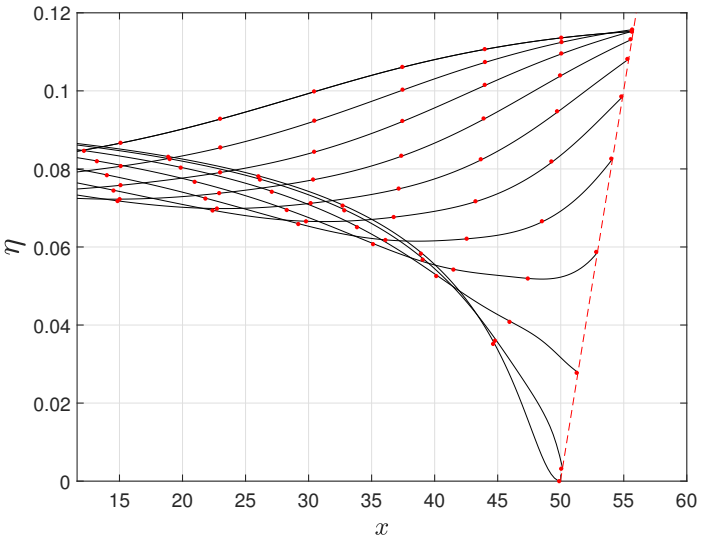


Figure 5.1: Present results (solid line) against analytical *Carrier and Greenspan* [1958] transient solutions (red dotted) of the water surface elevation η versus cross-shore position x at every $\Delta t = 4.4$ from $t = 0$ to $t = 44$. The bottom line corresponds to initial condition, $t = 0$ and the top line corresponds to $t = 44$

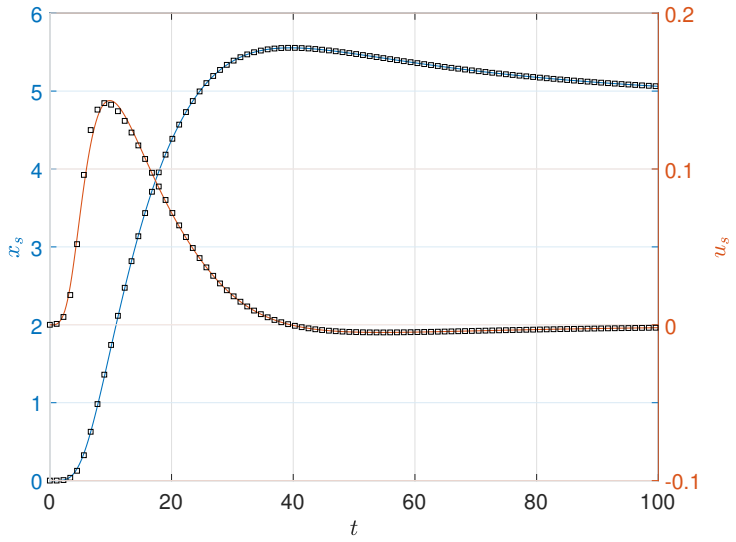
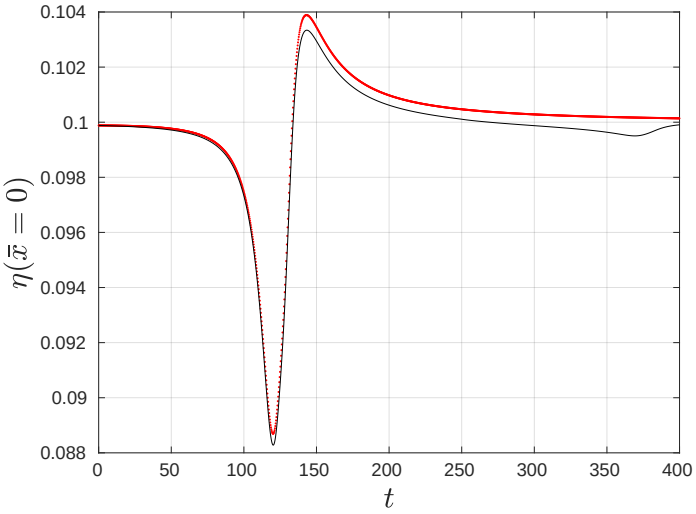


Figure 5.2: Present results (solid line) against analytical *Carrier and Greenspan* [1958] transient solutions (square dotted) of the shoreline position x_s (blue) and the shoreline velocity u_s (red) versus time t

(a)



(b)

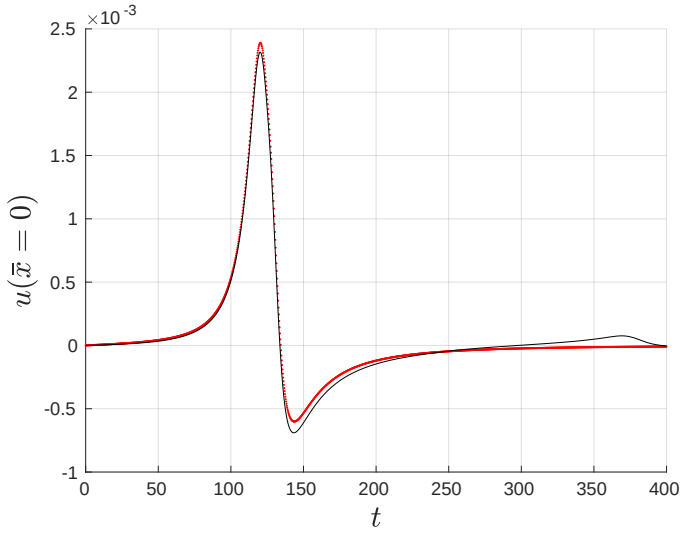


Figure 5.3: Present results (solid line) against analytical *Carrier and Greenspan* [1958] transient solutions (red dotted) of (a): surface elevation η and (b): velocity u at offshore boundary

5.1.1.2 *Carrier and Greenspan* [1958] periodic solutions

Carrier and Greenspan [1958] also presented an analytical solution for periodic non-breaking standing waves on a plane-sloping beach, in which the periodic waves have amplitude A and frequency ω. This periodic behaviour can be interpreted as a sinusoidal tide or non-breaking surface gravity wave in the swash. This also allows for verification of the numerical model's stability for multiple events. Solutions of this type of flow are specified by means of potential function: $\phi(\chi, \lambda) = AJ_0(\omega\chi)\sin(\omega\lambda)$, where J_0 is a zeroth order Bessel function of the first kind. Once the values of A and ω are defined, the analytical solutions of flow properties can be solved for in the (χ, λ)-coordinates and converted back into the (x, t) coordinates (see formulas (2.16) - (2.19) in *Carrier and Greenspan* [1958]) by solving a system of nonlinear equations. It is difficult to obtain accurate solutions, as the process of deriving the equivalent conditions in (χ, λ) from known (x, t) and vice versa is not trivial. Initial conditions at $t = 0$ and shoreline solutions are obtained easily since the nonlinear system is simplified into a linear system (either λ or χ is zero). The system can be solved numerically in a high order of accuracy using *fsolve* in MATLAB and the tolerance of this function is set at 10^{-10}.

At the offshore boundary, the nonlinear system can also be solved numerically to obtain analytical solutions. However, this is time consuming and the performance of the absorbing-generating offshore boundary does not justify this. Instead, a generating-absorbing boundary condition is used (see § 4.2). A sinusoidal incoming signal is specified at the offshore boundary

$$\eta_i = \frac{H_i}{2}\sin\frac{2\pi}{T}t \tag{5.1}$$

where H_i is incoming wave height, T is wave period. *Carrier* [1966] and *Synolakis* [1987] pointed out that nonlinear effects are negligible far from the shoreline.

Thus, the hydrodynamic variables far from the shoreline can be approximated in the uncoupled system of equations and the (χ, λ)-coordinates correspond directly to (x, t)-coordinates. To ensure that nonlinear effects are negligible, we must have $L > 4$ *Carrier* [1966]. Also, L is chosen such that the anti-node is formed at the offshore boundary. As a result, the summation of η at the offshore is actually double the incident wave amplitude. It allows us to quickly investigate how well the performance of the generating-absorbing boundary condition. Following the simplification given in (2.10) of *Synolakis* [1987], A can be approximated by

$$A \approx \frac{4A_{off}}{J_0(\sqrt{16L})} \tag{5.2}$$

where A_{off} is the amplitude of the signal at the offshore boundary for the given domain length L. Once A and $\omega = 2\pi/T$ is known, analytical solutions can be obtained and used as the benchmark. Since an anti-node is formed at the offshore boundary, we describe a train of sinusoidal incident signal of range $H_i = A_{off}$ and frequency of ω.

Here we take slope $= 0.1$, $H_i = 0.0142$, $T = 2\pi$, $L = 12.6$, $\Delta\bar{x} = 0.2$, $\Delta\bar{t} = 0.01$, $\alpha = 0.01$, $\beta = 0.0967$. For given parameters, the corresponding *Carrier and Greenspan* [1958] analytical parameters obtained from above procedure are $A = 0.4, \omega = 1$. We have about 25 nodes over one wavelength, and about 625 timesteps per period. The initial conditions is still water starting from mid-water level. An initial transient is observed but the periodic state quickly achieved after a few cycles.

The comparison of offshore signals shows excellent agreement (Fig. 5.4). A small phase difference between analytical and generating-absorbing offshore signal is observed, indicating also that nonlinear effects are very small at the boundary. There is a small difference in the amplitude (0.2% relative error) which is mainly

due to the outgoing signal not perfectly exiting the domain.

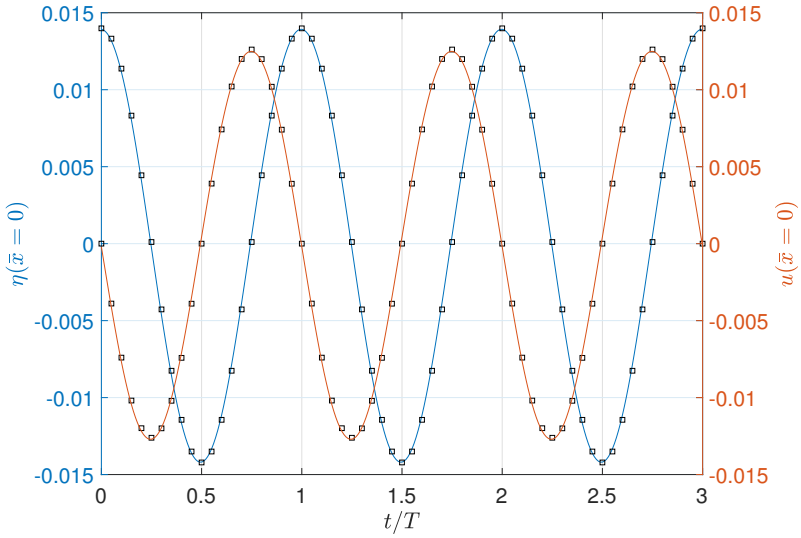


Figure 5.4: Present results (solid line) against analytical *Carrier and Greenspan* [1958] periodic solutions (black squared) of offshore hydrodynamics η_{off} (blue) and u_{off} (red) versus time t/T

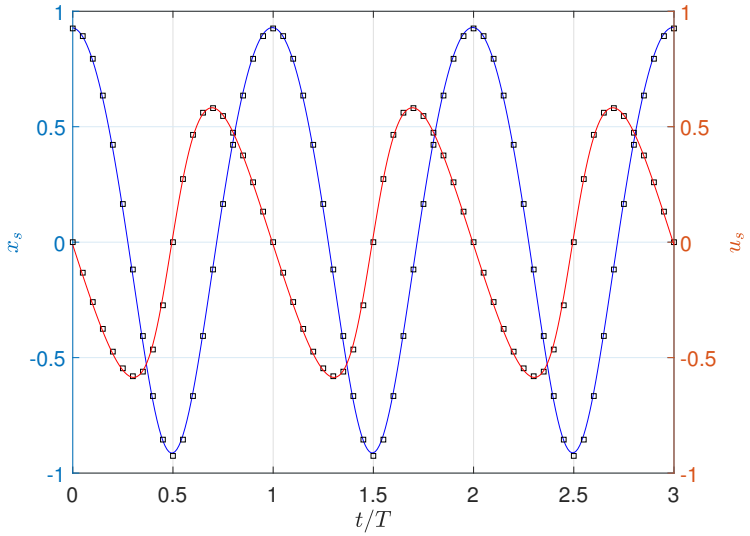


Figure 5.5: Present results (solid line) against analytical *Carrier and Greenspan* [1958] periodic solutions (black squared) of shoreline hydrodynamics x_s (blue) and u_s (red) versus time t/T

The shoreline position x_s and velocity u_s against t/T are shown in Fig.5.5.

The maximum relative error between model and analytical solutions is about 0.5%. The agreement can also be observed in the evolution of η and u over a full period (Fig. 5.6). There are small disagreements at the shoreline, which are similar to those observed in other models. These seem to result from phasing errors rather than numerical difficulties because solutions are smooth in this vicinity. The model stability is also confirmed by running the model for about 100 periods whilst maintaining similar accuracy.

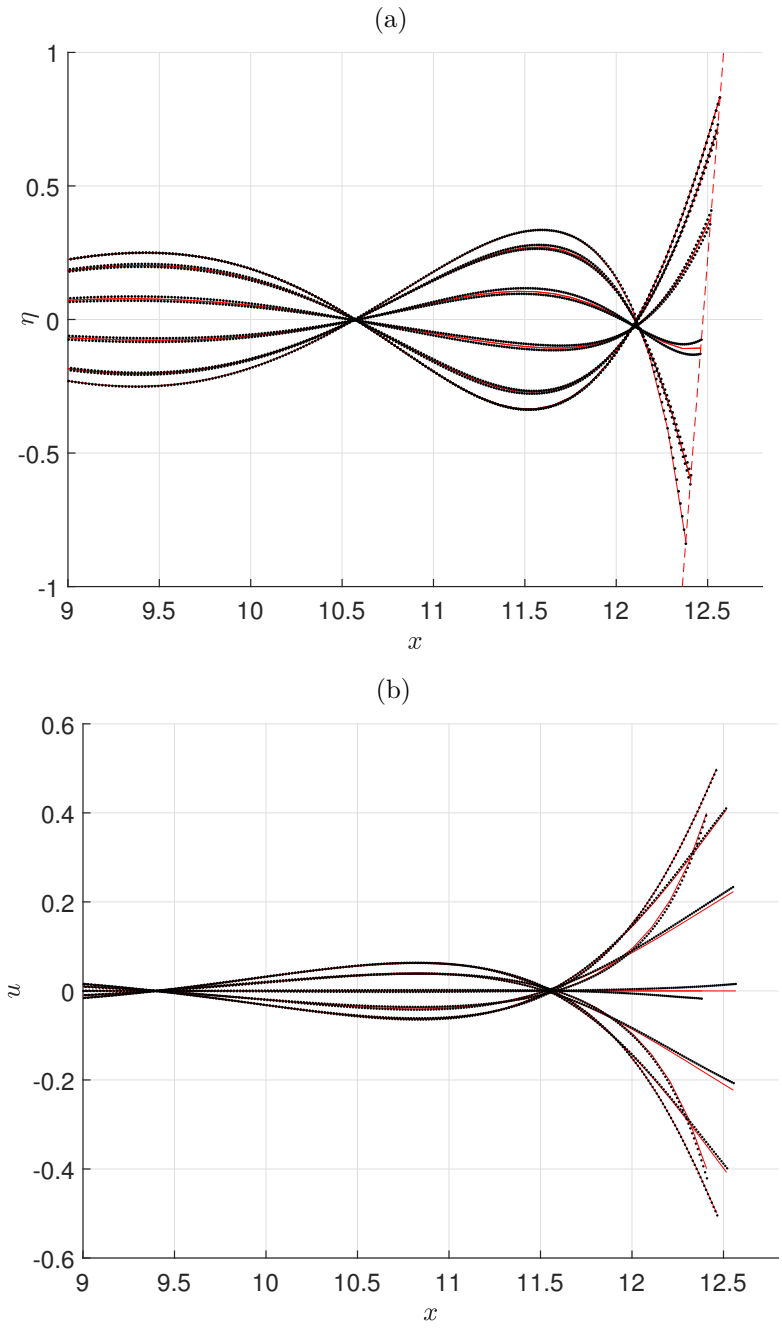


Figure 5.6: Present results (black dotted) against analytical *Carrier and Greenspan* [1958] periodic solutions (red solid line) of (a): η and (b): u evolution for a full period

5.1.2 *Shen and Meyer* [1963] swash solution

Shen and Meyer [1963] presented an analytical solution of the NSWEs corresponding to a bore impinging on a beach and subsequently running up and back down an initially dry slope. This swash motion was subsequently reinterpreted by *Peregrine and Williams* [2001] as an initial value problem. In general, the present model is developed for non-breaking waves, but this solution can be accommodated. Only the initial condition contains a discontinuity and no shock subsequently develops. Although the general behaviour is similar to CG58 transient case, it is still a good test since the hydrodynamics in this case are very dynamic and complex. Moreover, *Zhu* [2012], *Zhu and Dodd* [2013] and *Zhu and Dodd* [2015] implemented the erodible bed conditions under both bed load and suspended load transport and so the numerical solutions can be used as a benchmark for the present model when morphodynamics is included. The test on a frictionless fixed bed for hydrodynamics is compared with the analytical solutions of *Peregrine and Williams* [2001]. The SM63 swash event can be interpreted as initial value problem of *Peregrine and Williams* [2001] as shown in Fig. 5.7, i.e.

$$h(x,0) = h_0 \qquad \text{for all} \qquad x \leq x_0 \tag{5.3}$$

$$h(x,0) = 0 \qquad \text{for all} \qquad x > x_0 \tag{5.4}$$

$$\left.\begin{aligned} u(x,0) &= 0 \\ c(x,0) &= 0 \end{aligned}\right\} \qquad \text{for all} \qquad x \tag{5.5}$$

The domain length extends far enough offshore so that the swash motion is not affected by offshore conditions throughout the simulation and vice versa. The incoming signal at offshore boundary must ensure that the water depth here is maintained to be h_0 throughout simulation.

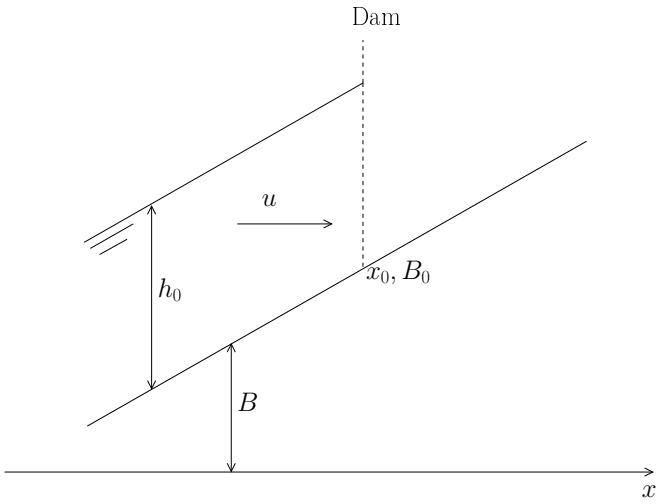


Figure 5.7: Sketch for PW01 initial condition

Following this boundary condition, a domain of $L = 50$, $h_0 = 1.0$ and slope $= 0.1$ is applied. CTM coefficients are $\alpha = 0.01$, $\beta = 0.03$. In this simulation, grid sizes of $\Delta\bar{x} = 0.02$ and $\Delta\bar{t} = 0.001$ are used. It is also noticed that the dynamics of *Shen and Meyer* [1963]'s swash event is much more extreme than these of *Carrier and Greenspan* [1958]'s transient case, thus the grid size must be much smaller for a good result (*Zhu and Dodd* [2013]). The spatial grid size in this simulation is 5 times smaller than the one used in *Carrier and Greenspan* [1958] transient case. The present results of h and u in comparison with analytical solutions are in good agreement as can be seen in the contour plot in Fig. 5.8. The maximum runup of the present model is smaller than the analytical solution, $x_s = 19.8$ instead of 20, and the backwash with the shoreline tip reaches $x = 0$ at $t = 39.6$ instead of $t = 40$. It is found that the errors are much improved by reducing the spatial grid size, together with reducing the temporal grid size to keep the Courant number being always less than 1 for numerical stability. Further investigation on the convergence of the model is presented in the later section.

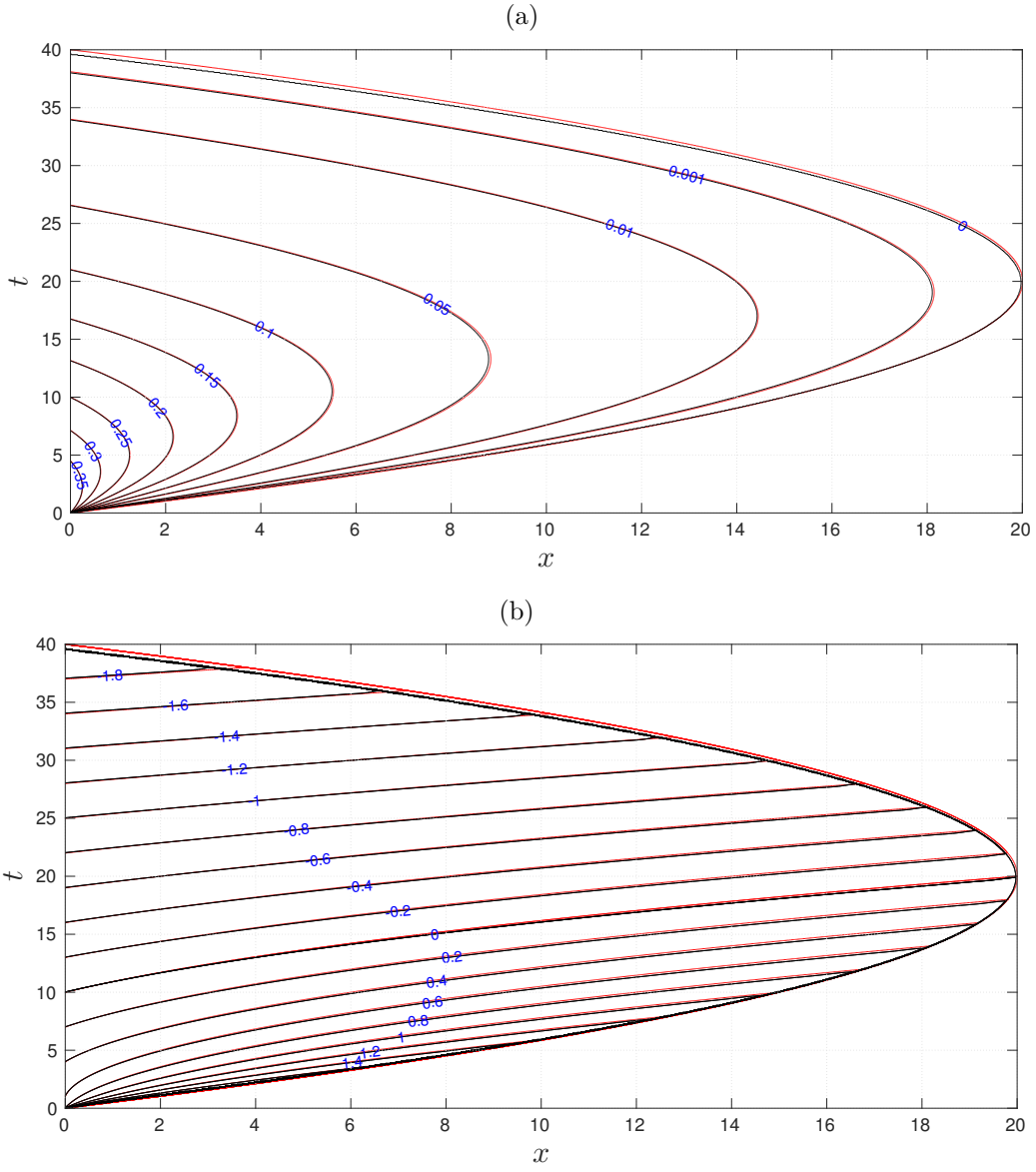


Figure 5.8: Contour plots of the present model solutions (black) of (a): h and (b): u in comparison with analytical solutions (red)

5.1.3 *Hubbard and Dodd* [2002] numerical solutions

We now bring together periodic motion and bed friction, and verify against the NSWEs model of *Hubbard and Dodd* [2002]. Their model simulates the

hydrodynamic behaviour of inner surf zone and swash zone in 2D NSWEs, including the wetting and drying treatment in fixed grid coordinates. Their verifications suggest that this model can be used as a benchmark for bed friction implementation with a high degree of certainty.

A sloping bed of domain length $L = 12.6$, slope $= 0.1$ was used for the simulation. The water level is still initially, $\eta(t = 0) = 0$, $u(t = 0) = 0$ over the whole domain. For the present model, $\alpha = 0.01$, $\beta = 0.0967$, $\Delta\bar{x} = 0.1$, $\Delta\bar{t} = 0.01$. The sinusoidal incoming signal is $H_i = 0.02$, $T = 10$, and $c_d = 0, 0.01, 0.025$ and 0.1. The model of *Hubbard and Dodd* [2002] is a NSWEs model which includes alongshore dimension. The equations are solved in a fixed coordinate system. For both models an identical bathymetry, friction coefficients and driving signal are used. The domain length of 13.0 is used in *Hubbard and Dodd* [2002] model, to allow the maximum run up to be included within the domain.

As presented above in § 3.5, as $h \to 0$ at the shoreline, the term $-c_d\frac{|u|u}{h}$ in (4.12) $\to -\infty$. During uprush, this term is balanced by h_x, which implies that $h_x \to -\infty$ at the shoreline. However, during backwash when $-c_d\frac{|u|u}{h} \to \infty$ for negative u, there is no balance for this term since h_x cannot $\to \infty$. Following *Zhu and Dodd* [2013], the backwash imbalance implies that $u = 0$ during backwash, in which the shoreline will not retreat at all time. In this test, for simplification, a threshold water depth for shoreline is applied, i.e. $h_{min} = 1 \times 10^{-5}$ is used for both models. It will prevent the term $-c_d\frac{|u|u}{h}$ approaching infinity at the shoreline. Therefore, shoreline retreat is still observed during backwash. It is also noted that *Hubbard and Dodd* [2002] also introduce a second depth tolerance h_{TOL} to stabilise the scheme, which defines an 'almost dry' cell (*Hubbard and Dodd* [2002]). To achieve smooth solutions for the *Hubbard and Dodd* [2002] model, we use 1300

cells in the cross-shore direction. The number of cells in alongshore direction is set to be 2 with zero alongshore velocity, thus, alongshore component is neglected in this simulation and the obtained solutions is 1D. The Courant number = 0.8 and $h_{TOL} = 10 \times h_{min}$ are used. The outgoing signal was not provided explicitly in the *Hubbard and Dodd* [2002] model but can be obtained easily from superposition assumption as the incoming and the summation signals are known.

For the frictionless case, $c_d = 0$, the total surface elevation $\eta(\bar{x} = 0)$ and depth-averaged velocity $u(\bar{x} = 0)$ at the offshore boundary are shown in Fig. 5.9. The offshore signals of both η and u are generally in good agreement with obvious disagreement only in troughs of the standing wave. It is also noted that Fig. 5.9 shows the initial generation of the wave and its subsequent complete reflection. The comparison between present and *Hubbard and Dodd* [2002] solutions for x_s for $c_d = 0, 0.01, 0.025$ and 0.1 are also shown in Fig. 5.10. Overall agreement is not perfect, solutions obtained by the present model are smoother. It is noted that the spatial grid of the present model is 10 times larger than *Hubbard and Dodd* [2002] for a similar degree of accuracy. This is mainly due to the fact that transformation functions in CTM obtain a better resolution in the vicinity of the shoreline. Moreover, a second depth threshold is not required for the present model, thus smoother solutions are obtained as can be seen in Fig. 5.10.

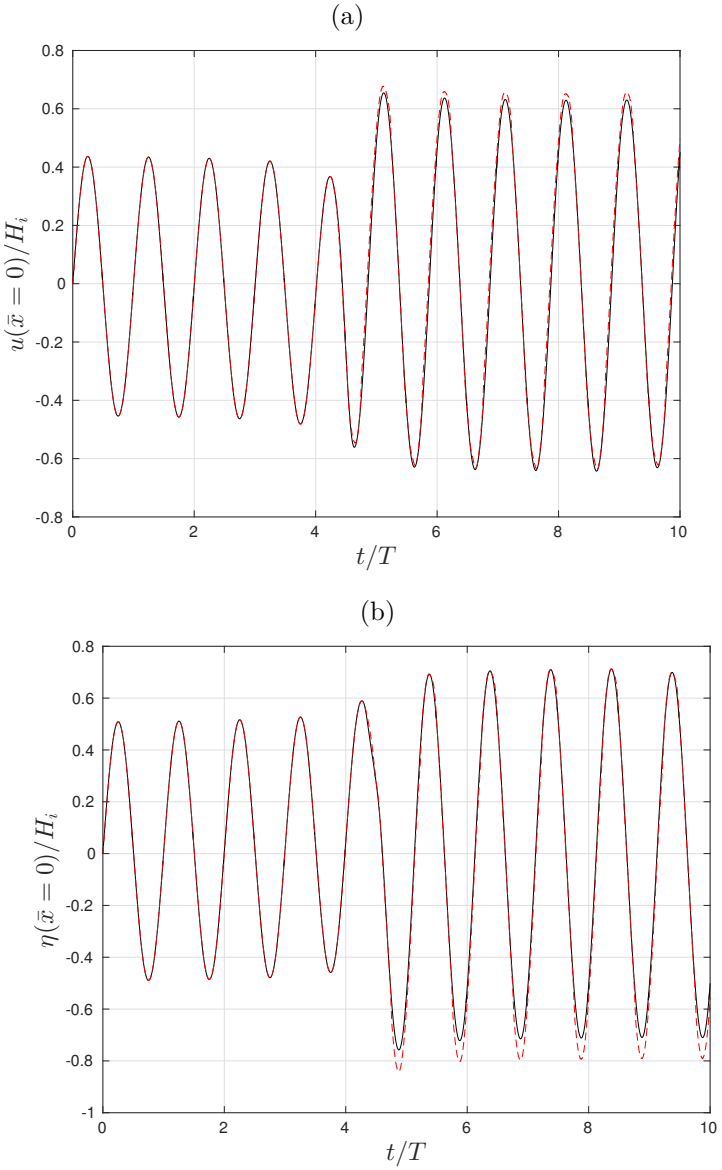


Figure 5.9: Present (solid lines) and *Hubbard and Dodd* [2002] (dashed lines) solutions of (a): the offshore water surface elevation η_{off}, (b): the offshore velocity u_{off} for $c_d = 0$

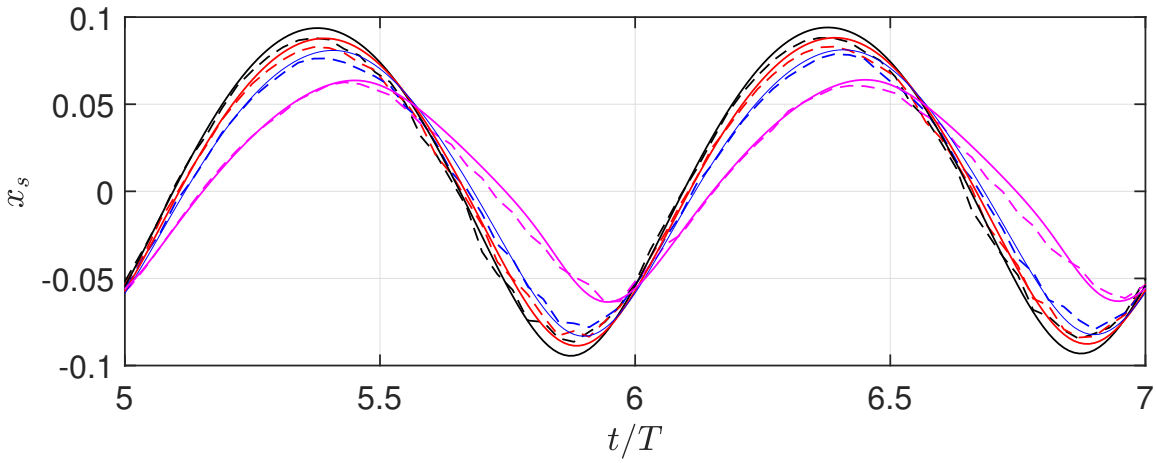


Figure 5.10: Present (solid lines) and *Hubbard and Dodd* [2002] (dashed lines) solutions of the shoreline position x_s versus t/T for $c_d = 0$ (black), 0.01 (red), 0.025 (blue), 0.1(magenta)

5.1.4 Offshore Boundary Verification

In previous verification tests, the performance of the moving boundary treatment is investigated. The full absorption or simultaneous generation and absorption of waves at the offshore boundary is applied in *Carrier and Greenspan* [1958] tests as presented above in § 5.1.1. The results show a small error due to imperfection in absorption. In this section, the error of the offshore boundary condition is investigated quantitatively for both the simultaneous generating-absorbing and the fully-absorbing boundary conditions using the method proposed by *Özkan-Haller and Kirby* [1997] and *Van Dongeren and Svendsen* [1997].

The test involves a specified sinusoidal incoming wave train of wave-height $H_i = 0.02$, wavelength $\lambda = 100$ and wave period $T = 100$ travelling along the domain of constant depth $h_0 = 1$ and length $L = 200$. The landward boundary is fully reflective (solid wall condition). At the offshore boundary condition, simultaneous absorbing-generating boundary condition is applied. The incoming

signal is turned off at $t = 10T$. Since $L = k\frac{\lambda}{4}$ with $k = 8$ is an even integer, a standing wave pattern is formed with an anti-node at the offshore boundary. There are two coefficients which are related to error of the offshore boundary conditions. The first is the error relating to the simultaneous generating-absorbing conditions, ϵ_{ga}. The second is the error relating to the fully absorbing conditions, ϵ_a. Both error coefficients can be examined in this test.

Theoretically, for the given parameter, the wave train reaches the solid wall after $2T$ from the initial of $t = 0$. It fully reflects at the solid wall and interferes with incoming wave. The outgoing wave takes $4T$ to exit the domain at the offshore boundary. Since an anti-node is formed at the offshore boundary, during simultaneous generation and absorption of wave train, the theoretical wave height at the boundary is expected to be double the incoming wave height, $H = 2H_i$. Any difference between the actual H and theoretical wave height is due to error of simultaneous generation-absorption at the boundary, ϵ_{ga}. The error of boundary conditions is quantified by

$$\epsilon_{ga} = \frac{|H - 2H_i|}{2H_i} \tag{5.6}$$

The offshore signals of individual incoming and outgoing water surface elevation, η_i and η_r against simulation time t/T are given in Fig. 5.11. The outgoing signal starts at $t = 4T$, which agrees with the theoretical. The incoming and outgoing signals have similar wave height. The phase difference due to non-linearity between the two signals is also observed.

After turning off the incoming signal at $t = 10T$, the last incoming wave reflects off the wall boundary and leaves the domain completely theoretically at $t = 14T$. Since incoming signal is turned off after this time, any disturbance left within the domain is due only to imperfect absorption at the boundary. Assuming

wave height of the maximum disturbance is H_d, the error of fully absorption boundary condition, ϵ_a is quantified as

$$\epsilon_a = \frac{H_d}{H_i} \tag{5.7}$$

The results of offshore signal is shown in Fig. 5.12. There is good agreement between the solutions and expectations which indicates that offshore boundary conditions were well-described. After $t = 14T$, waves exit the domain nearly completely which again illustrates good absorption capability. There is still a small disturbance left inside the domain which is shown in the magnified plot part of Fig. 5.11. Associated error coefficients, ϵ_{ga} and ϵ_a computed from (5.6) and (5.7) are about 2% and 1.5%, respectively. The error coefficient due to only absorbing ϵ_a is lower than the one due to simultaneous generating-absorbing ϵ_{ga}. It is also noted that the error coefficients are consistent for other tests with different values of H, λ and T. By using this test, error of the offshore boundary conditions can be determined quantitatively. The small error coefficients computed above suggest that offshore boundary conditions can be applied in the present model with high certainty. So, simultaneous specification of incoming signal and absorption of outgoing signal are achieved at the same boundary, which is suitable for describing artificial offshore boundary in shallow water model.

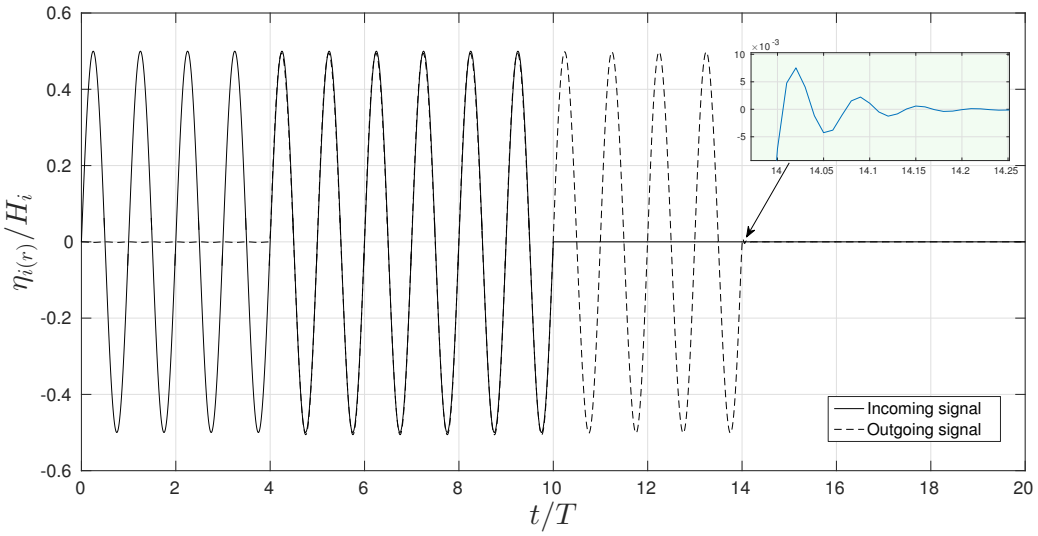


Figure 5.11: Simultaneous generating-absorbing boundary conditions: Time series at $\bar{x} = 0$ for individual signal incoming signal η_i and outgoing signal η_r. The magnified subplot is the disturbance left within the domain after theoretical time elapsed

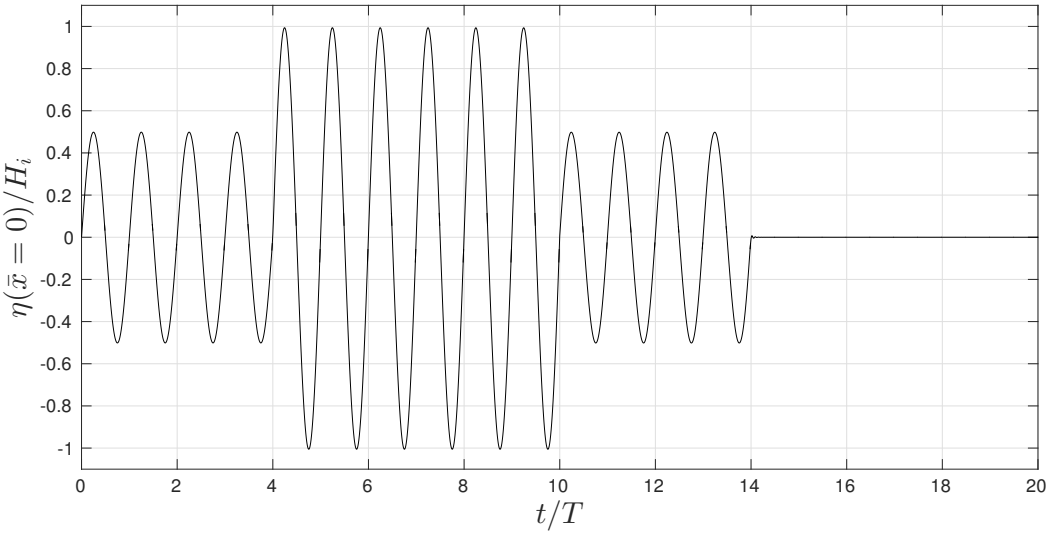


Figure 5.12: Simultaneous generating-absorbing boundary conditions: Time series at $\bar{x} = 0$ for total signal η

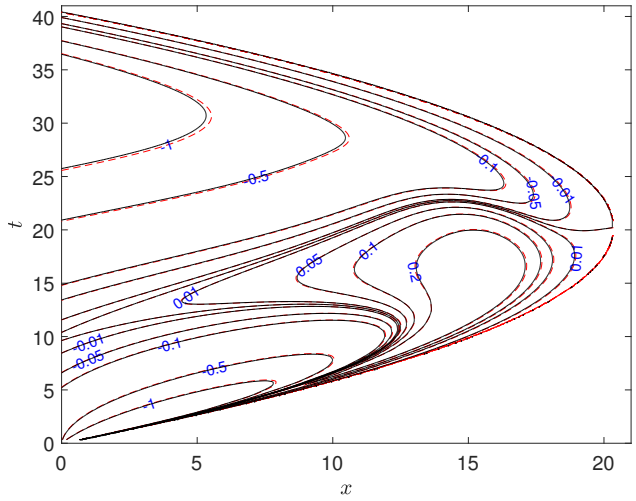
5.2 Advection equation of suspended sediment concentration

In this section, the advection equation of suspended sediment concentration will be included by setting a non zero value of E in (4.13). Although it could be argued that accurate modelling of hydrodynamics ensures accurate modelling of c, because c is passively advected at speed u, it is useful nonetheless as a verification case partly for reassurance and partly as a first step toward full morphodynamic coupling. To this end, we use the hydrodynamics case of *Carrier and Greenspan* [1958] periodic solution and that of *Shen and Meyer* [1963]. *Pritchard and Hogg* [2003a] and *Pritchard and Hogg* [2003b] developed the analytical solution of suspended sediment concentration under *Carrier and Greenspan* [1958] hydrodynamics of tidal and swash events, respectively. *Zhu and Dodd* [2015] obtained numerical solutions for c on a fixed bed for the *Shen and Meyer* [1963] swash event. These tests are obtained for NSWEs hydrodynamics, thus are good benchmarks to verify the present model.

5.2.1 *Zhu and Dodd* [2015] solutions

Zhu and Dodd [2015] developed a numerical model to investigate the suspended concentration under a *Shen and Meyer* [1963] swash event. We apply the same initial condition and the numerical setting presented in the *Shen and Meyer* [1963] hydrodynamics test. In particular, $L = 50$, slope $= 0.1$, and CTM parameters $\alpha = 0.01$, $\beta = 0.024375$. Grid sizes of $\Delta\bar{x} = 0.02$ and $\Delta\bar{t} = 0.001$ are used. The exchange rate parameter E (see § 3.4.1) is chosen to be 0.001 and 0.03, which are consistent with the parameters used by *Zhu and Dodd* [2015].

(a)



(b)

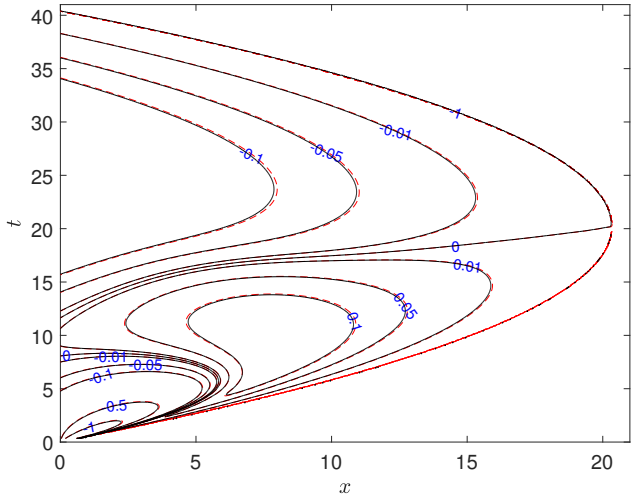


Figure 5.13: Contour plots of present model solution (black) against *Zhu and Dodd* [2015] (red dashed) of $c - u^2$ for exchange rate parameter of (a): $E = 0.001$ and (b): $E = 0.03$

The bed is non erodible by setting both σ and M to be zero. The present results for hydrodynamics are very close to the analytical solutions which are shown in § 5.1.2. The deviation of c from its equilibrium value $c_{eq} = u^2$ for

$E = 0.001$ and 0.03 are shown as contour plots in Fig. 5.13. The quantity $c - c_{eq}$ (or $c - u^2$) is related to the tendency toward erosion or deposition of suspended sediment, in which a positive value of $c - u^2 \Rightarrow$ deposition and a negative value $\Rightarrow$ erosion. The values of c obtained by the present model agree well with those of *Zhu and Dodd* [2015].

5.2.2 *Pritchard and Hogg* [2003b] solutions

The suspended sediment transport under reflected long waves forcing at infragravity frequencies on a plane beach was obtained analytically by *Pritchard and Hogg* [2003b]. They employed NSWEs coupled with the advection of suspended sediment concentration in Lagrangian coordinates. The suspended sediment transport under infragravity waves is localised close to the shoreline and principally directed landward, and so not responsible for the tendency of wave-dominated environment to erode sediment over the long-term. However, their findings provide a useful test case against which to validate the present model.

The suspended sediment transported for dilute, well-mixed suspension was introduced in § 3. The advection equation of suspended sediment concentration is derived for sandy sediment with the assumption of $u_{cr,s} = 0$. In *Pritchard and Hogg* [2003b], however, the formula for erosion and deposition were developed when considering a suspension of mud. In this test, we apply their formula for erosion and deposition for consistency. In particular, the non-dimensional form of erosion and deposition fluxes in (3.36) and (3.37) have been here adapted to include the deposition of flocs (see *Pritchard and Hogg* [2003b] for details), i.e.

$$q_e = \begin{cases} \frac{u^2}{u_e^2} - 1 & \text{for } |u| \geq u_e \\ 0 & \text{for } |u| < u_e \end{cases} \tag{5.8}$$

$$q_d = \begin{cases} \epsilon c & \text{for } |u| \geq u_d \\ c\left(1 - (1-\epsilon)\frac{u^2}{u_d^2}\right) & \text{for } |u| < u_d \end{cases} \tag{5.9}$$

where q_e, q_d represent dimensionless erosional and depositional fluxes of cohesive sediment, respectively; u_e and u_d are dimensionless critical velocities for erosion and deposition; ϵ is in the range of $0-1$, representing the depositional fraction of the cohesive sediment as single particle ($\epsilon = 1$) or purely flocs ($\epsilon = 0$). The advantage of employing $\epsilon > 0$ to describe cohesive sediment deposition are discussed further in *Pritchard and Hogg* [2003b].

Suspended sediment transport across the flat is also described by instantaneous sediment flux $q(x,t)$ and time-integrated net flux $Q(x)$. The instantaneous flux represents the total mass flux of suspended sediment passing a point x at time t, i.e. $q = cuh$. The time-integrated net flux represents the total mass that passes a position x over a duration of time t_1 to t_2, given by $Q = \int_{t_1}^{t_2} q dt$.

We consider a plane beach with domain length of $L = 100$ and gradient of $1/100$. Long low-frequency waves with period of $T = \pi$ and $H = 0.02$ are specified at the offshore boundary. These nondimensional parameters are consistent with the reference values (see section 2.1.1. in *Pritchard and Hogg* [2003b]). The hydrodynamics under these parameters are also consistent with the *Carrier and Greenspan* [1958] periodic hydrodynamics of $A = 0.2$ and $\omega = 1$. Here $\sigma = 0$ and $M = 0$ are used to prevent any bed change occurring. This is consistent with the fixed bed condition used in *Pritchard and Hogg* [2003b]. We used the reference values given by *Pritchard and Hogg* [2003b], i.e., $u_e = 0.08$, $u_d = 0.056$, $\epsilon = 0.05$ and $E = 2 \times 10^{-4}$. It is noted that the exchange parameter of 0.02 applied by *Pritchard and Hogg* [2003b] included the bed slope, which is also equivalent to $E = 2 \times 10^{-4}$ used in the present model.

It is found that regardless of the initial condition for suspended sediment, the concentration field achieves a periodic state after a few cycles. The concentration field is spatially localised, and most apparently found in the very nearshore region.

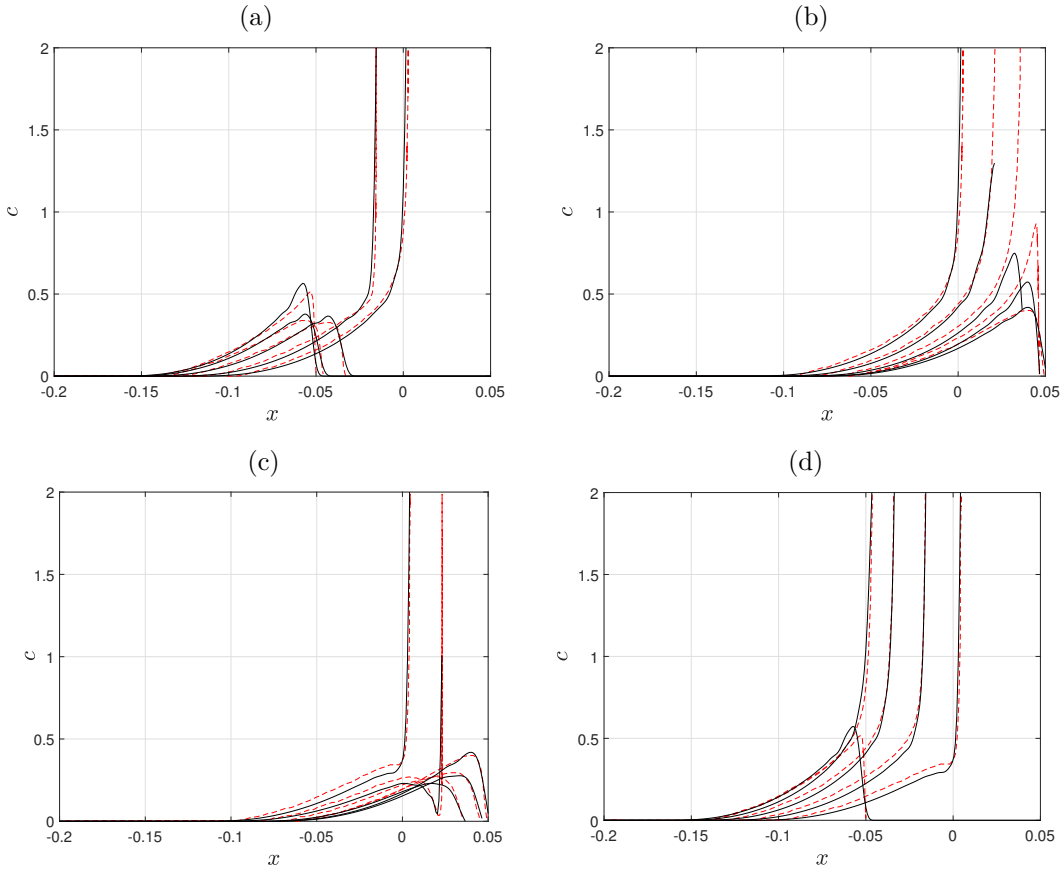


Figure 5.14: Evolution of c for a full period under *Carrier and Greenspan* [1958] flow conditions plotted at every $T/16$. (a): first half of run-up, (b): second half of run-up, (c): first half of run-down and (d): second half of run-down. *Pritchard and Hogg* [2003b] solutions: red dashed; present solutions: black solid

It means that under the conditions of long low-frequency waves, velocities are high enough to entrain sediment only in the nearshore region. This is correlated with high concentration field observed at these positions. The results of periodic concentration field are shown in Fig. 5.14, while the instantaneous and net cross-

shore sediment flux are shown in Fig. 5.15 and Fig. 5.16 respectively. The results are in reasonably good agreement as can be seen in the figures. The delayed response of the concentration field to the variation in velocity (settling and scour lag) are observed.

It is noted that the hydrodynamics are driven by a sinusoidal signal at the offshore boundary instead of *Carrier and Greenspan* [1958] analytical solutions. Thus, there are some small discrepancies in hydrodynamic solutions comparing to *Carrier and Greenspan* [1958]. However, this difference is very small as shown in the hydrodynamics-only test in § 5.1.1, and is thus not the reason for the difference of c. The other possibility is due to the boundary conditions at shoreline. As water depth h approaches zero, the exchange of sediment is rapid so instantaneous equilibrium concentration is achieved immediately. However, it is difficult to describe instantaneous equilibrium conditions due to the inclusion of different threshold velocities and flocs fraction ϵ. *Pritchard and Hogg* [2003b] described the instantaneous equilibrium state but in a Lagrangian fluid parcel, and this therefore has to be numerically interpolated to Eulerian coordinates. It is possible to implement into this model to obtain the boundary condition of c at shoreline. However, due to computational efficiency, instead of describing the solutions at the boundary, we apply a one side finite difference approximation and solve the governing system to obtain value of c at the shoreline boundary. This principally explains the small difference between our model and reference results, and may indicate why the net flux $Q(x)$ is higher in seaward but less in landward sediment movement (Fig. 5.16). Performance of the present model suggests that this coupled model is suitable for prediction of the morphodynamic evolution of an erodible bed under the influence of long waves NSWEs.

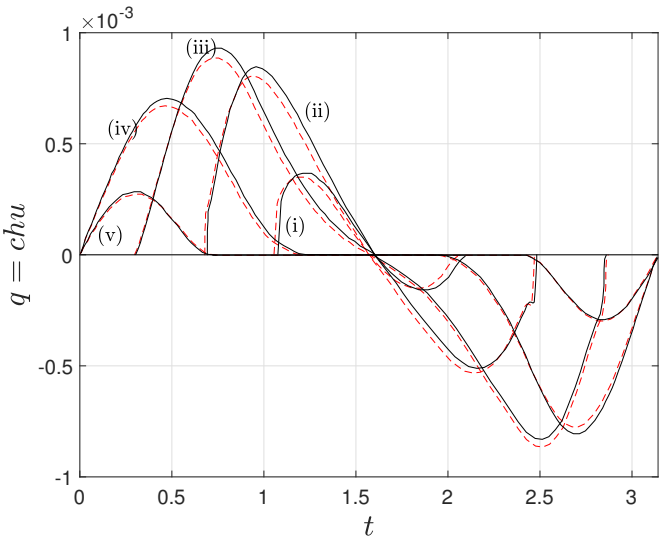


Figure 5.15: Instantaneous sediment flux $q(x,t) = chu$ versus time t at different locations. (i): $x = 0.0325$, (ii): $x = -0.0025$, (iii): $x = -0.0375$, (iv): $x =$ flài0.0725 and (v): $x =$ flài0.1075. *Pritchard and Hogg* [2003b] solutions: red dashed; present solutions: black solid

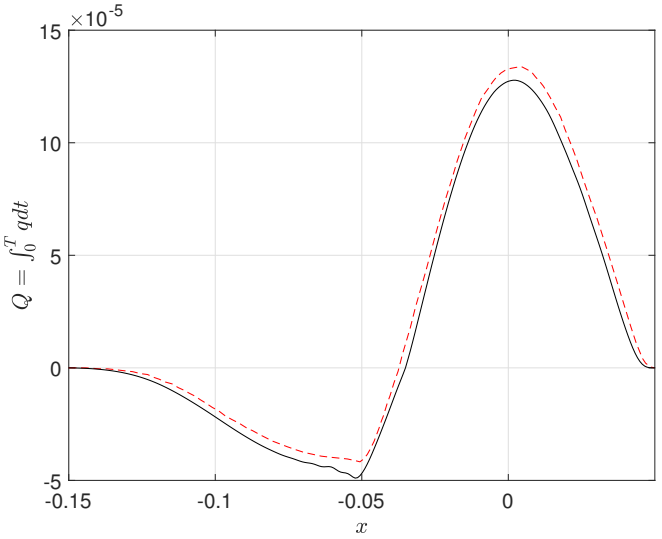


Figure 5.16: Net flux $Q(x) = \int_0^T q(x,t)dt$ over a period. *Pritchard and Hogg* [2003b] solutions: red dashed; present solutions: black solid

5.2.3 *Pritchard and Hogg* [2003a] solutions

Pritchard and Hogg [2003a] applied the same methodology with the same formula of erosion and deposition for cohesive sediment to obtain suspended sediment concentration in tidal motion. *Pritchard and Hogg* [2003a] simplified the hydrodynamics of tidal motions such that the velocity field is spatially constant and only time dependent. This simplification is only appropriate on a plane beach of constant gradient. However, as the bed changes subsequently, this simplified description is questionable, especially in the region close to the shoreline where frictional effects may produce a distinct slope (*Pritchard and Hogg* [2003a]). In this test, we employ the system of equations (4.15)-(4.18), considering the full NSWEs description for tidal motions.

We consider a plane beach with domain length of $L = 10$ and constant gradient of 1. It is noted that this gradient is in dimensionless form which is corresponding to the ratio of the veritcal and horizontal scales in dimensional. Long low-frequency waves with period of $T = \pi$ and $H = 1.0$ is specified at the offshore boundary. These nondimensional parameters are consistent with the reference scale values of tidal motions (see section 2.1 in *Pritchard and Hogg* [2003a]). Here $\sigma = 0$ and $M = 0$ are used to prevent any bed change occurring. Under the given hydrodynamic conditions, the maximum velocity obtained, $u_{max} = 1$, is consistent with the scale of velocity given by *Pritchard and Hogg* [2003a]. We used the reference values given by *Pritchard and Hogg* [2003a], i.e., $u_e = 0.8$, $u_d = 0.4$, $\epsilon = 0.025$ and $E = 1$.

The concentration field achieves its periodic state within the first tidal cycle and the evolution of c during flood and ebb tide is shown in Fig. 5.17. The velocity field is almost spatially constant, thus the exchange of sediment is only significant

in the very nearshore region as h becomes smaller and smaller. The tidal-averaged net flux $Q(x)$ is also shown in Fig. 5.18

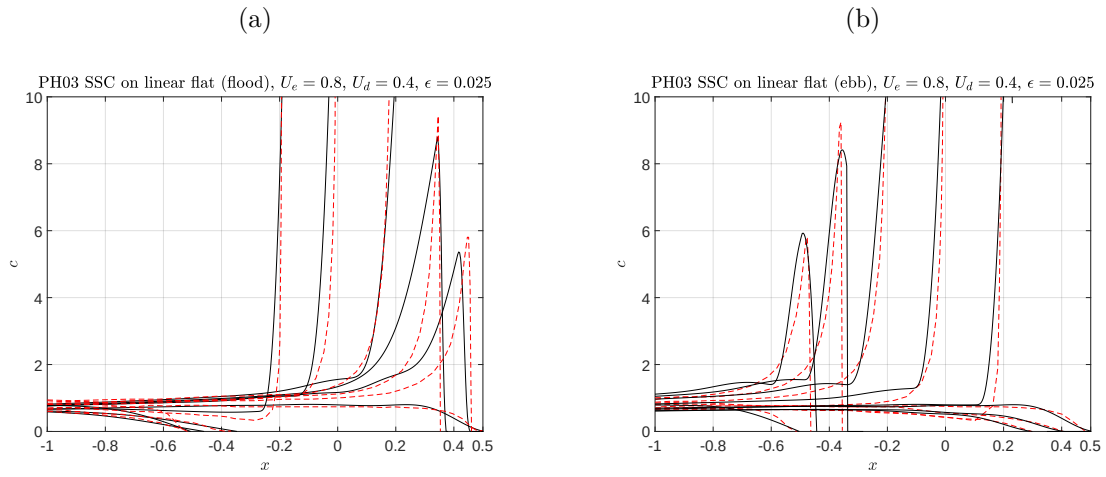


Figure 5.17: Evolution of c for a full period under tidal motion plotted at every $T/16$ during (a): flood; (b): ebb. *Pritchard and Hogg* [2003a] solutions: red dashed, present solutions: black solid

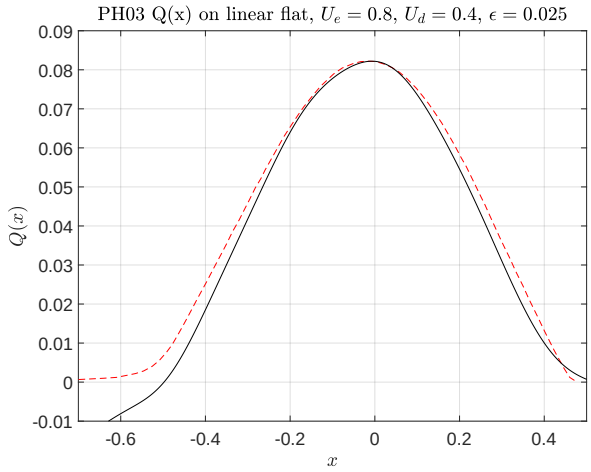


Figure 5.18: Net flux $Q(x)$ over a tidal cycle. *Pritchard and Hogg* [2003a] solutions: red dashed, present solutions: black solid

The same reasons that cause discrepancies in swash tests are also apparent in

tidal tests. Moreover, the global Froude number term is neglected in *Pritchard and Hogg* [2003a] but still considered this model. This suggests the reason why the results in the tidal cases are not as good as swash cases although they both employ the same erosional and depositional descriptions. Seaward of the intertidal region, $x < -0.5$, the net flux Q approaches zero in *Pritchard and Hogg* [2003a] while it becomes negative in the present model, corresponding to seaward movement of suspended sediment. This is due to the assumption of deep-water value of suspended concentration applied in *Pritchard and Hogg* [2003a]. In particular, they assumed that at a large distance from the shoreline, the total deposition from a fluid element over a cycle must equal the total erosion over that cycle. This non import of sediment effect is bounded the offshore boundary and the total flux Q decays rapidly to zero below low water. In the present model, the assumption of deep-water concentration is not applied so the seaward movement of sediment at sub-tidal zone is still observed. In the intertidal region, the landward movement of suspended sediment is similar in both models. This flux tends to move the sediment from the lower to the upper part of the intertidal region (*Pritchard and Hogg* [2003a]).

5.3 Coupled hydro-morphodynamical verification

In this section, the coupled model is applied to test bed evolution under both single and multiple events. The bed change under a *Shen and Meyer* [1963] swash event was introduced by *Kelly and Dodd* [2010], *Zhu and Dodd* [2013] and *Zhu and Dodd* [2015]. *Dodd et al.* [2008] presented the coupled model under storm

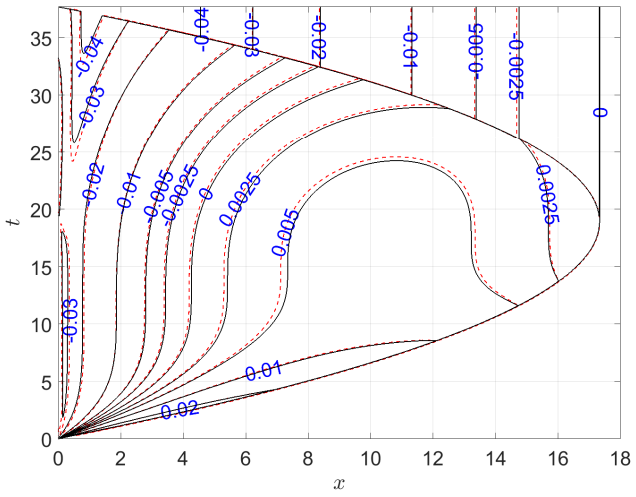
scale duration. Both are good benchmarks for verification of the present model.

5.3.1 Bed change over a single event

We now consider the same initial condition as for § 5.2.2 but now an erodible bed is included, such that $\sigma \neq 0$ and $M \neq 0$. Therefore, we isolate the bed change to be affected by either bed-load only or suspended-load only transport by setting $M = 0$ or $\sigma = 0$, respectively. Again, the same parameters and grid sizes $\Delta\bar{x}$ and $\Delta\bar{t}$ as used in § 5.2.2 are applied. *Zhu and Dodd* [2013] and *Zhu and Dodd* [2015] examined the effect of separate modes of sediment transport toward the final bed change. In this section, we verify our model under each mode of transport against *Zhu and Dodd* [2013] and *Zhu and Dodd* [2015].

We set $M = 0$ and $\sigma = 0.1$. Therefore, although we allow the suspended load to occur ($E \neq 0$), the bed change is only due to the bed load transport. Secondly, we set $\sigma = 0$ and vary both E and M, allowing the suspended load transport and thus bed change due to suspended load only.

(a)



(b)

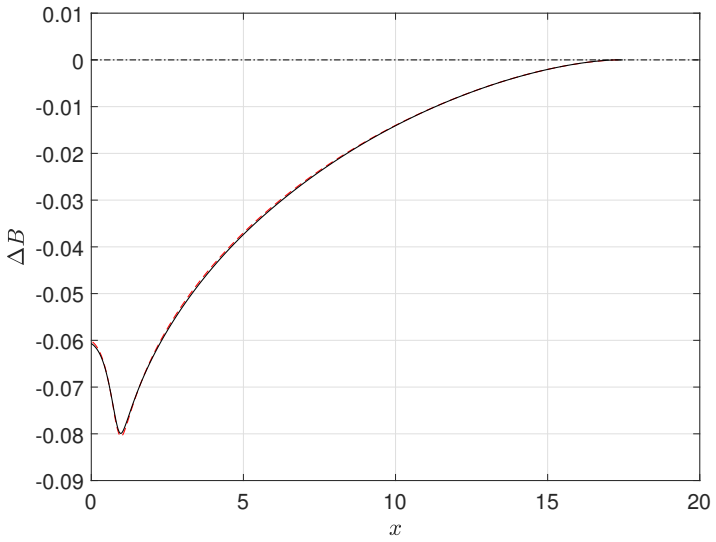
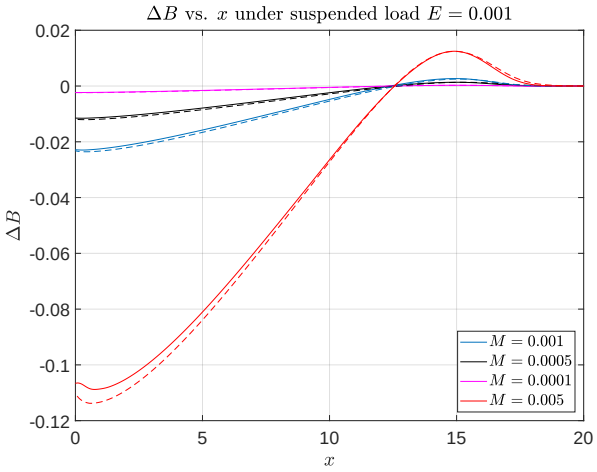


Figure 5.19: (a): Contour plots of ΔB, (b): Final bed change ΔB for *Shen and Meyer* [1963] swash event over a mobile bed of bed load only, $\sigma = 0.01$ and $M = 0$ (present model: black solid line, *Zhu and Dodd* [2013]: red dashed line)

(a)



(b)

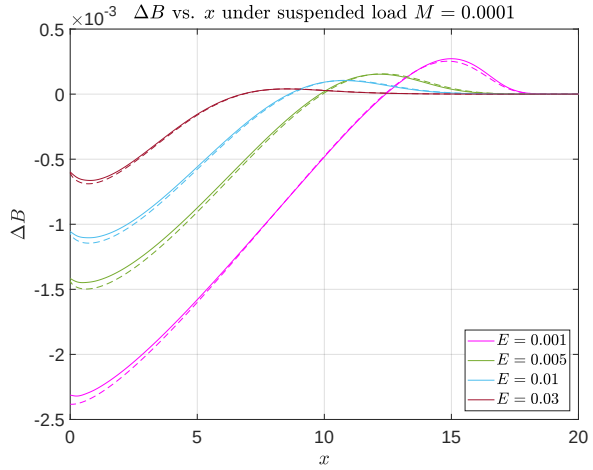


Figure 5.20: Final bed change ΔB for *Shen and Meyer* [1963] swash event over a mobile bed of suspended load only, $\sigma = 0$. (a) $E = 1 \times 10^{-3}$ and varied M; (b) $M = 1 \times 10^{-4}$ and varied E (present model: solid line, *Zhu and Dodd* [2015]: dashed line)

The results of the beachface evolution and final bed change due to bed load only are shown in Fig. 5.19. The final bed change due to suspended load when varying M and E are shown in Fig. 5.20. Overall, the coupled simulation results

agree well in comparison to *Zhu and Dodd* [2013] and *Zhu and Dodd* [2015] with similar patterns of hydrodynamics and bed-change.

5.3.2 Bed change over multiple events

So far, the model performance has been confirmed through hydrodynamics, advection of sediment and bed change verification tests (see § 5.1, § 5.2 and § 5.3.1). The latter tests have been for a single event only. It is desirable to test over a long duration if this approach is able to be used for long-term predictions. However, it is difficult to find benchmark results for long term simulations (i.e. either storm scale for wind waves or annual scale for tides). Cross-shore evolution of an initially plane beach under the action of a train of sinusoidal waves (4000 periods) was presented by *Dodd et al.* [2008] for both an impermeable and permeable bed. Their model includes bottom friction and bed-load transport due to the Grass formula. It is noted that the Meyer-Peter-Múller transportation equation applied in our model and the Grass formula are identical for $u_{s,cr} = u_{b,cr} = 0$ (see § 3). In this test, the bed diffusion with downslope mobilisation, i.e. (4.21) is considered instead of (4.14).

It is noted that *Incelli et al.* [2016] reproduced the validation test for wind waves over storm-scale duration, showing a close agreement with results of *Dodd et al.* [2008]. Hence, we use the cross-shore results of *Incelli et al.* [2016] for an impermeable bed and non-breaking incoming waves as a benchmark for verification. The physical parameter in *Incelli et al.* [2016] are set as follows: $c_d = 0.025$, $A = 0.004 s^2 m^{-1}$, $p = 0.4$ and $\phi = 32^0$, which are equivalent to $\sigma = 0.0654$ in the present model.

In *Incelli et al.* [2016], the domain length is $12m$ with 240 cells. The wet-dry

boundary treatment in this model was proposed in *Hubbard and Dodd* [2002]; a secondary threshold h_{TOL} is used, below which the velocity is considered to be zero (see *Hubbard and Dodd* [2002] for more details). $h_{min} = 0.002m$ and $h_{TOL} = 0.0025m$ are used. The initial bed bathymetry is given by *Dodd et al.* [2008]. In particular, the initial beach slope $= \tan 8^0$, the still water depth at seaward boundary $h(\bar{x} = 0) = 1$ and the domain length is $L = 7.115$. The water is set to be still initially ($\bar{t} = 0$). For the present model, $\alpha = 0.01$, $\beta = 0.171$, $\Delta\bar{x} = 0.03$ and $\Delta\bar{t} = 0.002$ are used. The number of spatial cells between the two models are consistent. The incoming signal is a series of sinusoidal waves with period $T = 5\pi$ and $H = 0.025$ (equivalent to $T = 5s$ and $H = 0.025m$ in *Dodd et al.* [2008] model). The simulation duration is $4,000$ periods. The same absorbing-generating boundary condition for hydrodynamics as *Incelli et al.* [2015] is applied. The bed level at the offshore boundary, $B(\bar{x} = 0)$, is updated and set equal to that at the next node at each time step, following the extrapolation approach proposed by *Dodd et al.* [2008]. The shoreline boundary condition are presented in **??** with the bed level updated from previous time step. Fig. 5.21 shows the evolution of bed profiles in comparison with *Incelli et al.* [2016] model. The formation of a bar can be observed at $x = 5.5$ after 1000 periods in Fig. 5.21. This bar develops and advances seaward, along with the erosive action in the upper part of the beach. Fig. 5.21 also shows a direct comparison of the bed change ΔB between the present model and *Incelli et al.* [2016]. Overall, bed profiles between the two models are in good agreement with some discrepancy in the upper part of the beach. It is not clear what causes this small discrepancy. The secondary threshold in the model of *Incelli et al.* [2016] appears not to be responsible because a similar discrepancy is observed when it is removed.

The conservation of sediment in the present model is also confirmed by checking the difference between the net bed change and the net sediment transport at the offshore boundary due to bed load transport over time from $t = 0 - T_i$ ($T_i = iT$ with i is the number of periods, which range from 0 -4000 in this simulation). Fig. 5.22 shows that the difference between these two values over simulation duration is very small in the order of 10^{-6}, which confirm the conservation of sediment in present model.

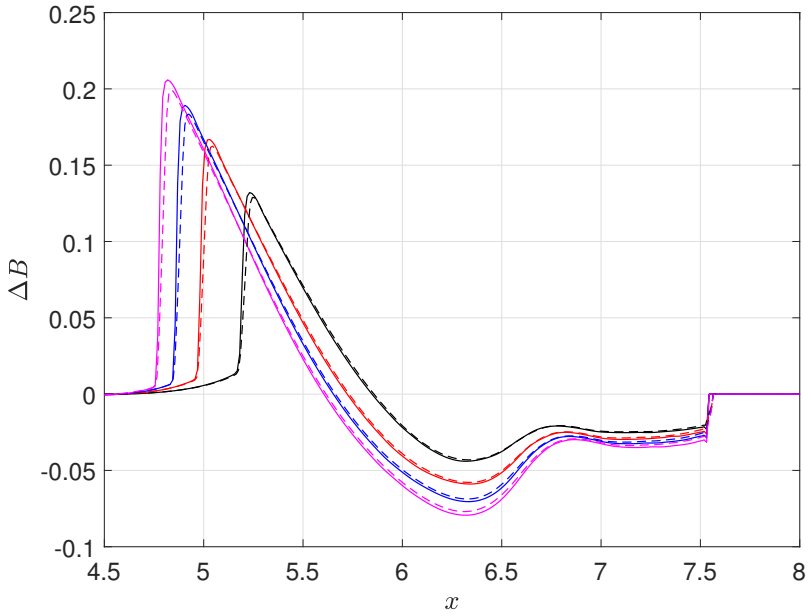


Figure 5.21: Bed change ΔB between present model (dashed line) and *Incelli et al.* [2016] model (solid line) at $t = 1000T$ (black), $t = 2000T$ (red), $t = 3000T$ (blue) and $t = 4000T$ (magenta)

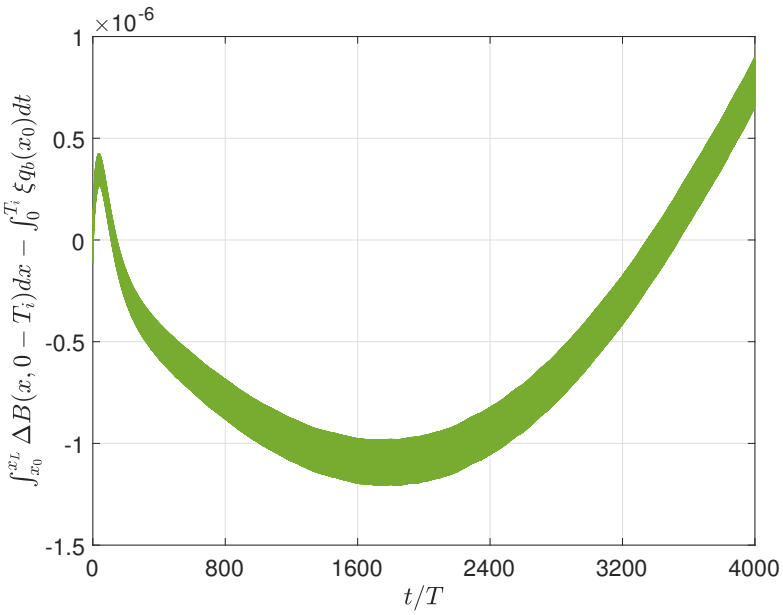


Figure 5.22: Sediment conservation of present model

5.4 Model convergence test

The sizes of $\Delta\bar{x}$ and $\Delta\bar{t}$ are important parameters in the numerical model. The smaller the grid sizes are, the smaller the error is, but the longer the computational time takes. In this section, both spatial and temporal grid sizes are varied to investigate the convergence of error, and the sensitivity of model accuracy to the temporal and spatial grid size. We simulate the *Carrier and Greenspan* [1958] periodic events for hydrodynamics only and *Zhu and Dodd* [2013] for morphodynamics under swash event to see to what extent the results are changed. It is useful to see how the results converge with various $\Delta\bar{x}$ in an acceptable computational time, so a reasonable number of computational nodes for further simulations could be proposed.

In the *Carrier and Greenspan* [1958] periodic test, we simulate the same case

as in §5.1.1.2 with different $\Delta\bar{x} = 0.05$, 0.1, 0.2, 0.3 and 0.6, corresponding to 100, 50, 25, 17 and 8 nodes per wave-length. The size of $\Delta\bar{t}$ is proportional to $\Delta\bar{x}$ such that the fixed Courant number of 0.5 maintained. The tests simulate over a duration of $20T$. At $t = 10T$, the periodic state is already achieved, the root mean square error (e_{rms}) of all computation nodes is computed over a period by

$$e_{rms} = \sqrt{\frac{\sum_i^{N_x} \sum_n^4 e_{i,n}^2}{4N_x}} \tag{5.10}$$

where $e_{i,n}$ is the absolute error of each governing variables at each computational node and each governing variables; i denotes the spatial node number along the computational domain, and n denotes the number of governing equations. Fig. 5.23 shows the relationship of e_{rms} and the number of spatial computational nodes. e_{rms} reduces when N_x increases. The best fit line has a gradient of -2.73, which is not close to the expected value of -4.0 for the fourth-order central finite difference approximation applied. This is probably due to the finite difference approximation applied at the boundary nodes, which are one-sided, and second order instead of the higher order formula employed for central nodes. Moreover, the model is driven by a linear approximation, i.e. the signal at the offshore boundary is assumed to be sinusoidal as illustrated in §5.1.1.2.

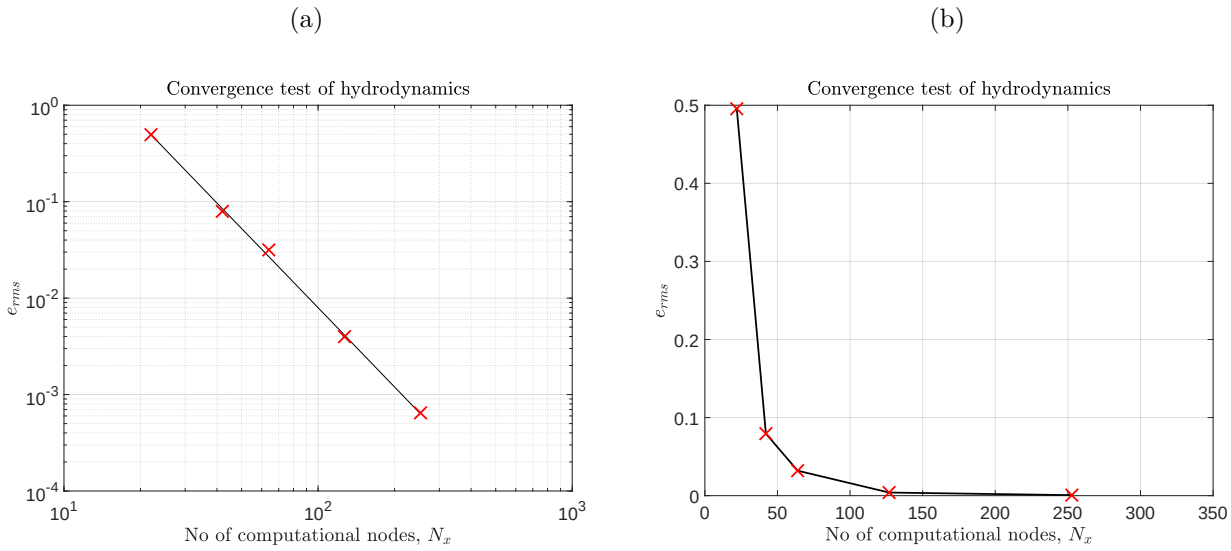


Figure 5.23: Spatial grid convergence test result for hydrodynamics only. (a): in log scale, (b): in linear scale.

The computational times for tests from the smallest to the largest spatial grid sizes are 21653s, 14435s, 3423s, 1643s and 1025s, respectively. It is noted that reducing $\Delta\bar{x}$ results in reducing $\Delta\bar{t}$ to keep Courant number less than 1 in all cases, resulting in the rapid increase of the computational time. For a finer grid size, such as $\Delta\bar{x} = 0.01$, corresponding to 500 nodes per wavelength, the computational time is over a day, which is not practical as the computational time for fully-coupled model is supposed to be much longer.

On the other hand, for a fixed value of $\Delta\bar{x} = 0.6$, we also varied the temporal grid sizes, $\Delta\bar{t} = 0.048$, 0.03 and 0.012, corresponding to the Courant number of 0.8, 0.5 and 0.2 respectively. It is noted that in all cases the Courant number must be smaller than 1 for a stable simulation. Fig. 5.24 shows the variation of the shoreline position in time of different Courant number simulations.

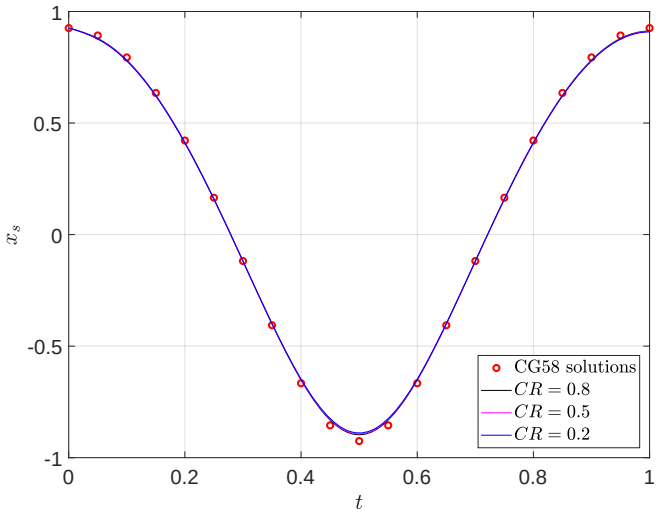


Figure 5.24: Error sensitivity test for different Courant number. The results of x_s versus t for *Carrier and Greenspan* [1958] periodic case

It is apparent that the accuracy obtained by reduction in the spatial grid size is significant. The results improve to a lesser extent by reducing temporal grid size. The effect of spatial grid size on the convergence is more dominant than the temporal grid size.

The next stage is testing the convergence of the fully coupled model. In this test we consider the numerical results of *Zhu and Dodd* [2013] for the *Shen and Meyer* [1963] swash event of bed load only. The reason is the bed change results are more sensitive to σ rather than M (*Zhu and Dodd* [2013]). This is due to highly singular characteristic behaviour near the shoreline as $\sigma \to 0$. We also employ the convergence test with different $\Delta\bar{x}$. In this test, the spatial grid size $\Delta\bar{x}$ is varied while the Courant number is kept constant as 0.5. The bed change results for different $\Delta\bar{x}$ are shown in Fig 5.26. The smaller the spatial grid size is, the better the solutions are. It is noted that the analytical solution for the morphodynamics

test is not available, so that the results of *Zhu and Dodd* [2013] for $\Delta x = 0.01$ (in physical domain) is chosen as the reference value. It is also noted that there is no relation between the spatial grid size and the wavelength in this swash event since the initial condition assume an infinite water column (see *Peregrine and Williams* [2001]). Here, for an inter-comparable against hydrodynamics only, it is noted that the error for $\Delta\bar{x} = 0.02$ is approximate in a same order as 100 numerical nodes per wavelength in hydrodynamics-only test (see Fig. 5.23). The root mean square formula in (5.10) is employed with morphodynamics equations included. Fig. 5.25 shows the relationship of e_{rms} and the number of spatial computational nodes. e_{rms} reduces when N_x increases. The best fit line has a gradient of -3.12, which is not close to the expected value of -4.0 for the fourth-order central finite difference approximation applied. However, the gradient in morphodynamic test is closer to the expected value, comparing to the one in the hydrodynamics-only test.

It is noted that the number or spatial node in this swash event is about 10 times higher than *Carrier and Greenspan* [1958] periodic case for a similar degree of accuracy. The reason is a swash motion is more dynamical than a tidal motion. The spatial grid sizes must be very small to capture all changes in a small time *Zhu and Dodd* [2013]. Such small grid sizes result in significant computational efforts. For a tidal motion, the above convergence test for *Carrier and Greenspan* [1958] periodic case can be applied as the flow behaviour is quite similar. In particular, the spatial grid size of $\Delta\bar{x} = 1/25$ wavelength and a Courant number of 0.8 is applied for periodic *Carrier and Greenspan* [1958] such as tidal simulations. It is also noted that in tidal motion, the wavelength is much longer than the intertidal region length and thus much higher than the computational domain length. Here,

we use $\Delta\bar{x} = 0.05$, which corresponding to approximate 20-30 nodes along the intertidal region.

(a) (b)

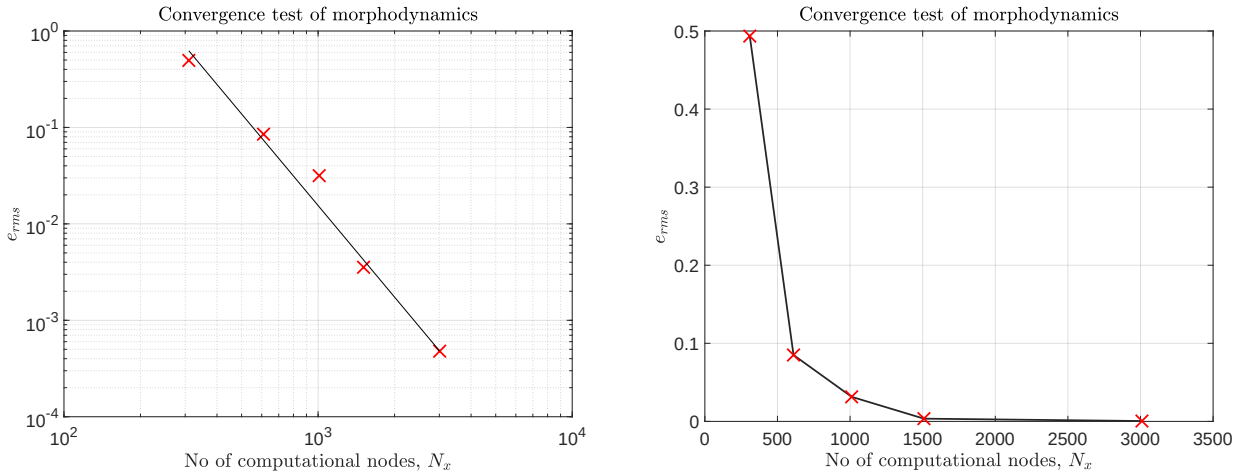


Figure 5.25: Spatial grid convergence test result for fully coupled model. (a): in log scale, (b): in linear scale.

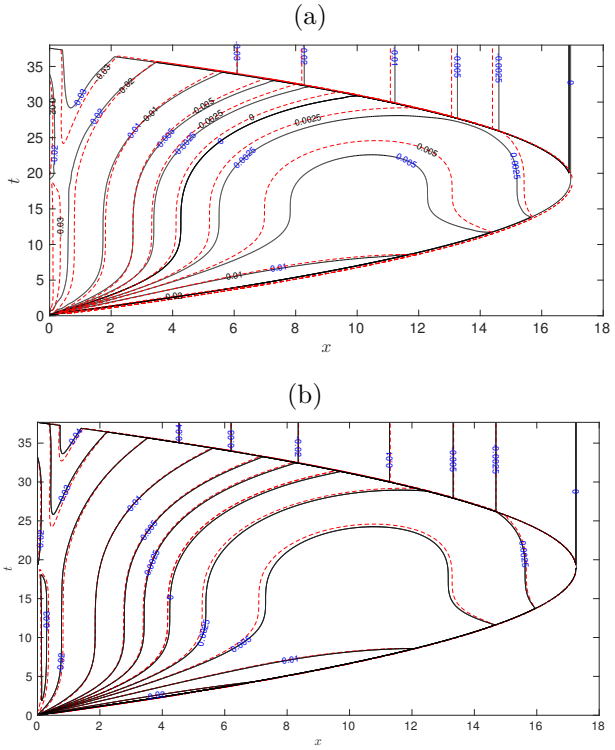


Figure 5.26: Convergence test for morphodynamical simulation of *Shen and Meyer* [1963] swash event (solid black line: present solutions; red dashed line: solutions of [*Zhu and Dodd*, 2013]). The contour plot of ΔB for (a): $\Delta\bar{x} = 0.03125$ and (b): $\Delta\bar{x} = 0.01$

CHAPTER 6

Morphodynamical Evolution of Plane Beach under pure Tidal Currents

In this chapter, we employ the coupled hydro-morphodyanmics model developed in previous chapters to investigate long-term morphodynamics of a macro-tidal sandy beach under pure tidal currents. The main hydrodynamics is tidal currents described by the NSWEs. It is noted that *Friedrichs and Aubrey* [1996] have proposed the equilibrium profile for both tide- and wave-dominant beaches. Here, we impose a plane beach of tidal-dominated environment, composed of non-cohesive sediment and subject to a macro-tidal range. The reason for a plane slope is that we want to avoid any anticipation on the eventual bed profile. It is noted that the early changes in beach profile are likely to have large adjustments to more realistic profile. Here we can ignore these changes on a long-term evolution by using a plane slope configuration. Despite that sandy beaches without waves actions are rare in nature as already mentioned, understanding

tides effect is crucial for a better knowledge of their roles in beach evolution, particularly in a macro-tidal environment. This chapter concerns with sandy beaches which evolve under pure macro-tidal forcing. This idealisation allows us to investigate the influence of bed- and suspended-load on beach dynamics, as well as how much full morphodynamic coupling influences the modelling. The contributions of these modes of transport on the morphodynamics are investigated separately and in combination. This simplification model also provides a starting point for understanding the dynamics of macro-tidal sandy beaches under more complex conditions, i.e. morphodynamics of those beaches when waves are included.

It was noted earlier (see § 2) that shallow water descriptions have been applied to muddy tidal flats (see *Roberts et al.* [2000], *Pritchard and Hogg* [2003a] and *Zhou et al.* [2015]). However, these models are either simplified (see *Roberts et al.* [2000], *Le Hir et al.* [2000], *Pritchard and Hogg* [2003a]) or uncoupled, in which the bed level is only updated after a certain number of tidal cycles (*Roberts et al.* [2000] and *Zhou et al.* [2015]) or even not considered (*Pritchard and Hogg* [2003a]). More importantly, only suspended load developed for cohesive sediment is considered in these models.

Here, we first consider a sandy beach with sinusoidal tidal signal. Physical parameters for the sandy beach and tidal motion are discussed in § 6.1. The values of dimensionless parameters are also given in this section. The bed change under suspended load only is considered in § 6.2. As discussed in previous chapters, the bed change under suspended load transport are dependent on M and E. The effects of parameters M and E on the bed change are investigated by varying these values against reference test. Main findings are presented in comparison

with a reference test.

Bed-load-only transport is considered in § 6.3. The well-known formula MPM are considered (see § 3). We also consider different initial conditions of the flow to see whether or not there is an impact on the final bed change. The combined load simulation is considered in § 6.4. Further comparison on fully-coupled versus weak- (or quasi-) coupled model is presented in § 6.5. In this section, we obtain the tidal averaged of sediment fluxes under bed and/or suspended load transport. The bed evolution equation is only solved after each tidal cycle instead of solving simultaneously as in the fully-coupled model. The difference in final bed change illustrates how the coupling affects the solution of model.

6.1 Physical and corresponding dimensionless parameters; and numerical settings for tidal motion

6.1.1 Physical parameters

Our main interest is the effects of macro-tidal beaches composed of fine to medium sand. The tidal currents are considered as weak flows (*Soulsby* [1997]) and thus only small grain size sediment is mobilised (see Appendix A). *Le Hir et al.* [2000] indicated that tidal long-shore currents are likely to dominate the sediment transport only in deeper water. Thus, we consider cross-shore tidal currents as the main forcing hydrodynamic. Hydrodynamics in a shallow water region such as the nearshore zone can be well described by NSWEs. These equations characterise well water motion in which the velocity can be considered as depth-invariant (see

§ 3). In this study, tidal motion is considered as the only entrainment mechanism.

We consider a rather gently sloping beaches since wave actions are commonly found less active there (*Short* [1991]). Here, an associated slope of tide-dominated muddy flats (*Roberts et al.* [2000]) with gradient of 0.005 is imposed. We also impose sinusoidal semi-diurnal tides of $6m$ range. This tidal range is commonly found in the macro-tidal environment around the British Isle, i.e. East and South Coasts (*BODC* [2013]). The scales for non-dimensionalisation are characterised by tidal period and bed slope as shown in § 3.4.2. The physical parameters and equivalent dimensionless and numerical settings used in the reference case are presented below and summarised in Table 6.1 and 6.2 (see also *Soulsby* [1997]).

Following a similar procedure to *Zhu and Dodd* [2015], we may expect a sediment threshold on both bed and suspended load not to have a significant impact on tidal morphodynamics (see Appendix A). The difficulty is how to estimate erosional rate $\hat{m}_e$ and its equivalent non-dimensional parameter M as it is related to how quickly the bed changes under suspended load. *Zhu and Dodd* [2015] attempted to find a relationship between erosional and depositional rates for given net onshore flux of sediment entrained in the uprush only of a solitary wave swash event. They found that dimensional suspended-load flux $Q(x)$ at a certain position is about linearly proportional to the value of M (see Fig. 16 of *Zhu and Dodd* [2015]). However, it is still uncertain about the validity of their findings in the physical parameters of tidal motion. We assume a further simplification, in which the linear proportionality between M and sediment fluxes Q is still valid in tidal motion. Moreover, *Zhou et al.* [2015] and *Pritchard and Hogg* [2003a] approximated that the average onshore fluxes of cohesive sediment in macro-tidal flats is about $3kgm^{-1}$. We may assume that this value is applicable

Physical Parameters	**Values**	
Friction coefficient (c_d)	0.004	
Bed porosity (p)	0.5	
Gravity acceleration ($\hat{g}$)	9.81	ms^{-2}
Median sediment grain size (D_{50})	4.0×10^{-4}	m
Salt water density ($\hat{\rho}$)	1027	kgm^{-3}
Sediment density ($\hat{\rho}_s$)	2650	kgm^{-3}
Relative density of sediment (s_{rel})	2.580	
Erosional rate parameter ($\hat{m}_e$)	1.0×10^{-3}	ms^{-1}
Bed load mobility parameter (A)	0.0	$m^{-1}s^2$
Critical velocity for bed load ($\hat{u}_{cr,b}$)	0.0	ms^{-1}
Critical velocity for suspended load ($\hat{u}_{cr,s}$)	0.0	ms^{-1}
Effective settling velocity ($\hat{w}_s$)	0.02	ms^{-1}
Bed slope ($\tan\gamma$)	0.005	
Tidal range ($\hat{H}_{tide}$) or vertical length scale ($\hat{h}_0$)	6.0	m
Tidal period ($\hat{T}_{tide}$) or time scale ($\hat{T}_0$)	4.32×10^4	s
Horizontal length scale ($\hat{x}_0$)	1200	m
Velocity scale ($\hat{u}_0$)	0.028	ms^{-1}
Concentration scale ($\hat{c}_0$)	0.035	

Table 6.1: Physical parameters of reference test

to fine sand. Therefore, an approximate value of $\hat{m}_e = 1.0 \times 10^{-3} ms^{-1}$ over a tidal cycle is obtained. Another procedure to determine the value of $\hat{m}_e$ is based on the power-law of concentration under currents, which is described in *Soulsby* [1997]. Following this procedure, the value of $\hat{m}_e = 6.0 \times 10^{-4} ms^{-1}$ is obtained (see Appendix B). This value is smaller than the above estimation of $\hat{m}_e = 1.0 \times 10^{-3} ms^{-1}$ but is still close. It looks reasonable as both fine sand and muddy sediment are easily entrained into the water column, in which the erosional rate of muddy sediment should be higher.

Model descriptions and BCs	
Friction	Chézy approach
Sediment transport	Suspended load only (without threshold)
Bed diffusion and Infiltration	Not included
Shoreline BCs	CTM and L'hôpital's rule
Offshore BCs	Absorbing-generating and extrapolation
Nondimensional Parameters	**Values**
Drag coefficient (C_D)	0.8
Bed-load mobility (σ)	0.0
Suspended-load mobility (M)	10.0
Exchange parameter (E)	144.0
Bed slope	0.005
Tidal range (H_{tide})	1.0
Tidal period (T_{tide})	1.0
Domain length (L)	20.0
Time length	$1 \times 10^2 T_{tide}$
Spatial grid size ($\Delta\bar{x}$)	0.05
Temporal grid size ($\Delta\bar{t}$)	0.002

Table 6.2: Numerical setting of reference test

6.1.2 Justification of numerical settings

Still water applied in initial conditions correspond to either low or high tide. So, we decide to start the simulation at the low-tide phase instead of mid-tide and $u(\hat{t} = 0) = 0$ is applied. However, even at still water (low-tide), the concentration field is not zero in reality. As the velocity achieves its smallest value, it takes a while until the concentration reaches its smallest value. The same behaviour is observed for the maximum velocity. This difference in phase between the velocity and concentration field is called the settling lag, and is also described in *Pritchard and Hogg* [2003a]. This lag effect is inversely proportional to sediment grain size. As a result, a non-zero initial condition of concentration or the so-called pre-suspended concentration should be implied (see *Pritchard and Hogg* [2005]). However, for simplification, we apply a zero concentration as the initial condition,

i.e. $c_{\hat{t}=0} = 0$ is assumed throughout the domain. The pre-suspended sediment concentration is supposed to have a significant effect on the initial bed change as shown in *Pritchard and Hogg* [2003a]. The bed change is either initially deposition or erosion, depending on whether the pre-suspended concentration is either larger or smaller than the instantaneous equilibrium, respectively (*Pritchard and Hogg* [2003a]).

In tidal motions, *Pritchard and Hogg* [2003a] pointed out that the periodic state of concentration field can be achieved shortly after few tide cycles or even within the first cycle. This is because the adjustment time of suspended sediment is short compared to the large scale of tidal period. As a result, the pre-suspended concentration will quickly adjust to achieve its periodic state. The abundance or shortage of pre-suspended sediment concentration will exchange with the bed within a shorter time compared to the tidal scale, leading to initial deposition or erosion. For long-term simulation, this pre-suspended sediment is only important if it is too high; in that case, the amount of settled sediment on the bed and bed deposition becomes significant. This high sediment concentration is only common in cohesive wave-dominated flats where waves are more energetic to erode muddy sediment compared to tides (*Roberts et al.* [2000]). Therefore, high pre-suspended concentration is unlikely to occur in a sandy beach of tide-dominant, except perhaps a large amount of supply sediment is placed such as in beach nourishment.

Following *Kobayashi et al.* [1987], offshore boundary was developed under the assumption of linear wave theory and superposition so that nonlinear effects are neglected. However, this assumption is only true for small nonlinear effects, which means the domain length must be greater than four times the wave-length

(*Titov and Synolakis* [1998]). In this case, such long domain length means that the offshore boundary is far away from the region of interest, which demands more computational efforts. It is also noted that the nonlinear effects in tidal motion are small due to its small global Froude number (see *Pritchard and Hogg* [2003a]). Moreover, this small error does not increase with the time of simulation (see § 5) and it can be assumed negligible. The simulation uses the offshore BCs of *Kobayashi et al.* [1987] for h, u and c derived in § 4.2, while the bed level is updated by setting it equal to that at the first inner node at each time step (see the extrapolation approach proposed by *Dodd et al.* [2008]) (see also § 4.2).

6.2 Suspended load transport only

We consider the reference test of numerical settings given in Table 6.2 and refer to this test as REF case. An equilibrium state for bed change is not achieved within 10^2 tidal cycles. Following *Roberts et al.* [2000], the equilibrium profile for tidal flat of cohesive sediment is only achieved within the order of $10^4 - 10^5$ cycles. *Pritchard and Hogg* [2003a] indicated that a periodic state of the concentration field is achieved after few cycles of hydrodynamics. In this simulation, the periodic states for hydrodynamics and concentration are achieved even more quickly, as shown in contour plots of u and c in Fig 6.1 and 6.2. These plots illustrate the solutions of u and c during 2 tidal cycles right after the initial condition and at the end of simulation, i.e. $0 - 2T$ and $98T - 100T$. The similar patterns in different time levels illustrate that the periodic state of u and c are achieved within the first tidal cycle with the only difference being the transient oscillation observed right after the start of simulation, i.e. around $t = 0$. The intertidal region can also be defined together with temporal variation of the shoreline in both figures.

A similar periodic behaviour of c is observed in cohesive sediment on tidal motion by *Pritchard and Hogg* [2003a]. However, *Pritchard and Hogg* [2003a] stated that this state is achieved within a few cycles which is longer than in the present simulation. This is because muddy sediment takes longer to exchange between the bed and the water column compared to sand. It is also noted that E is a function of sediment grain size and directly affects c (see the advection equation of c in (4.17)). We will discuss the effect of E on c later.

As can be seen in Fig. 6.1 and 6.2, u achieves its maximum absolute value during mid tide of either flooding or ebb phase; while $u = 0$ during high or low tide. u directs landward during flooding and vice versa, seaward during ebb tide. The spatial variation of u at a certain time is small as shown in the contour plot lines, i.e. u lines are almost horizontal lines with respect to time t and thus, the velocity field can be considered spatially constant. The reason is that the spatial derivatives of the momentum equation is restrained by global Froude number F, which is very small in tidal motion (see (3.48)). The term $h_x + B_x$ has to be small to counterbalance the effect of F, resulting in the small variation in space of both u and $(h + B)$. This reflects a very small spatial variation of both velocity and water level in tidal motion.

As discussed above, the still water condition is still applied for c at $t = 0$, i.e. $c(t = 0) = 0$. As a result, initially, the sediment starts to erode into the water column. The relationship between u and c is also shown in the comparison between the two contour plots. The maximum of c occurs around mid-tide where $|u|$ achieves its maximum; and c reaches its minimum value around high tide and low tide. Here the settling lag and effect of water depth on c are also observed. It is noted that c is not spatially constant like u. c is advected by u and is also

dependent on E and h as can be seen in (3.49). As a result, c varies with space as h increases toward offshore. Although the tendency of increase (decrease) in c requires the increase (decrease) in speed $|u|$, there is still a phase lag between them. This is not very clear in the contour plots but can be observed in some specific time and position. For instance, at $u = 0$ during high tide of low tide, a non-zero c is still observed. In fact, c and u are not in the same phase and this lag effect is even more significant seaward. As a result, the rate of entrainment and deposition of suspended sediment is not unique due to the effect of h and settling lag. By analysing the effects of E, h toward the settling lag, the morphodynamics of suspended load on sand beaches under tidal currents can be clarified.

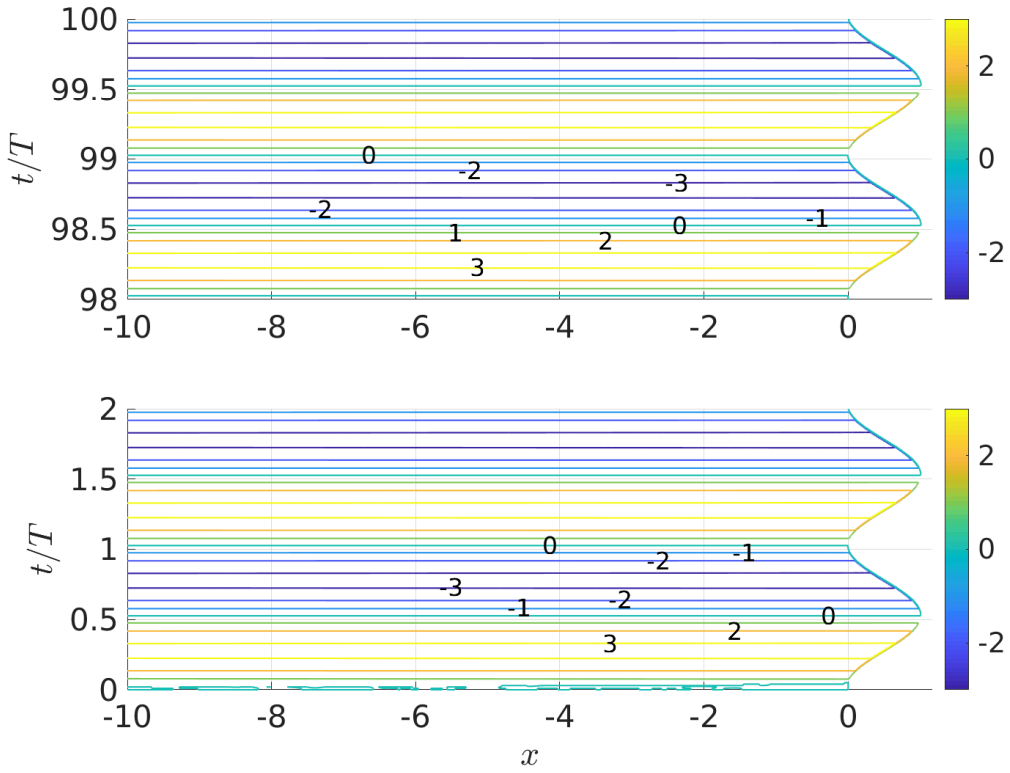


Figure 6.1: Contour plot of u for 2 tides from $0 - 2T$ (bottom) and $98 - 100T$ (top).

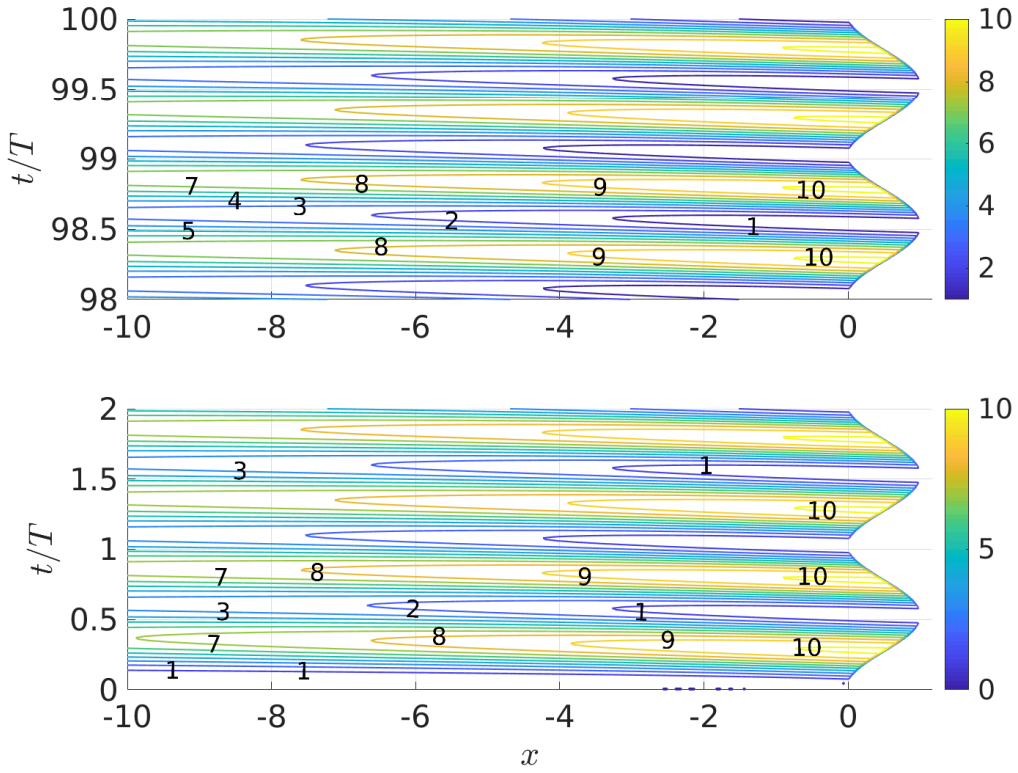


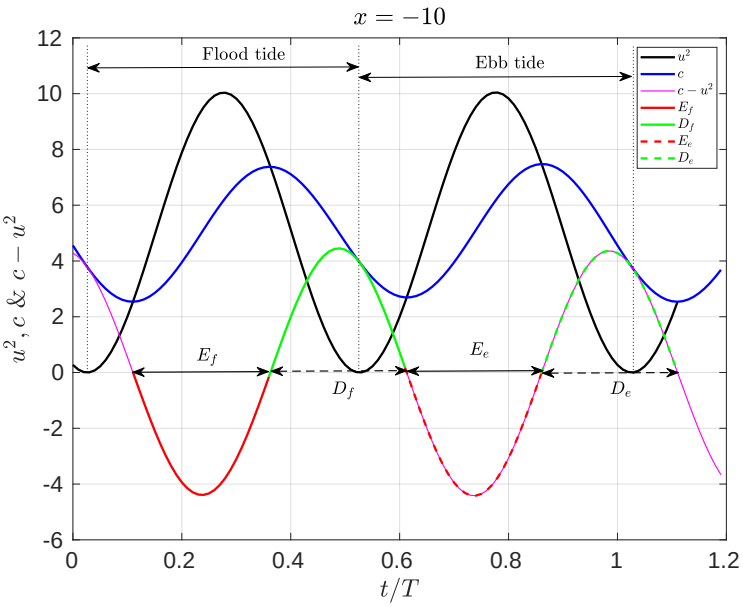
Figure 6.2: Contour plot of c for 2 tides from $0-2T$ (bottom) and $98-100T$ (top).

When considering suspended load transport, the tendency of sediment to settle on (erode off) the bed is expressed in the difference between c and its instantaneous equilibrium state $c = u^2$. The instantaneous equilibrium of concentration is the concentration at which neither erosion nor deposition of bed occurs (*Pritchard and Hogg* [2003a] and *Pritchard and Hogg* [2003b]). In the present model, we investigate the difference between c and u^2. The value of $c-u^2$ is normally defined as the net of deposition. In particular, the bed is accreting if $c - u^2 > 0$ and eroding if $c - u^2 < 0$. As stated above, while u in tidal motion is almost spatially

constant and can be solved by NSWEs, c in tidal motion is more complicated as it depends not only on the hydrodynamics h, u but also the exchange parameter E. Therefore, c and u are in different phases, resulting in the variation of $c - u^2$ with respect to time and space. As a result, the bed change at different location is not the same over time despite of the symmetrical sinusoidal hydrodynamics. We will investigate these factors in the following section.

The nonlinear effects are small in tidal motion with the phases and amplitudes of u being similar between offshore and nearshore regions (see Fig. 6.1). However, the lag effect between c and u leads to a non-zero net of $c - u^2$ over a tide or multiple tides. c, u^2 and $c - u^2$ versus t after the periodic state is achieved are shown for different positions $x = -10$, $x = -6$, $x = -2$, $x = 0$, $x = 0.25$ and $x = 0.75$ (see Fig. 6.3, 6.4 and 6.5). It is noted that under the nondimensional scale, the intertidal region is bounded in $x = 0 - 1$ with $x = 0$ and $x = 1$ being the low tide and high tide limits, respectively. It is also noted that we extend the domain up to $x = -20$, which may be out of the valid range of NSWEs and out of the interest region. However, it may assure that error from the offshore boundary is reduced as much as possible and does not affect the interest region. By comparing these values at different positions x and versus t, we can investigate how sediment is eroded, transported and accreted on the bed under suspended load transport. By investigate how $c - u^2$ varies with space and time, we may understand how the bed changes with space and time under suspended load transport and why there is accretion at this location but erosion at another location.

(a)



(b)

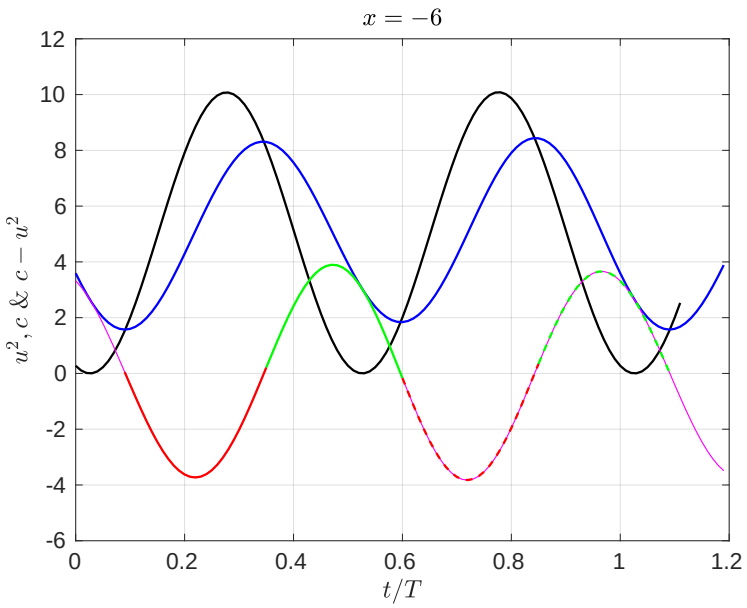
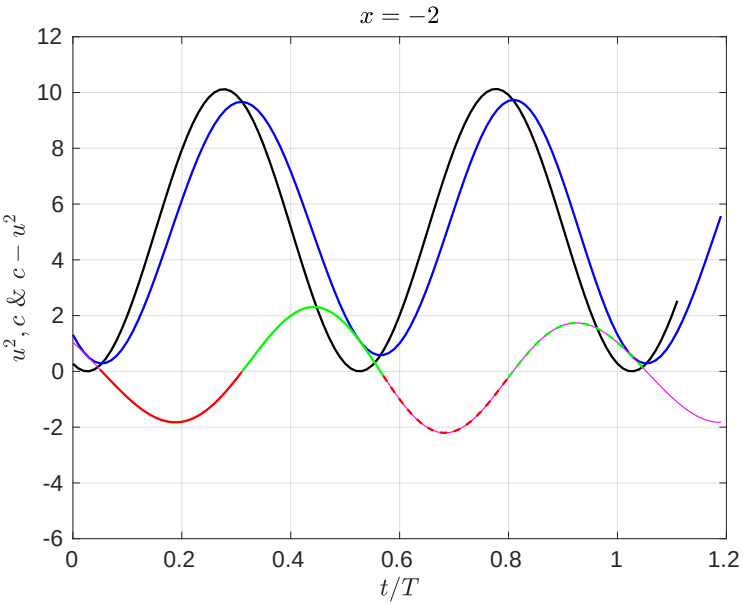


Figure 6.3: Reference test results of c (blue), u^2 (black) and $c - u^2$ (magenta) versus t/T at periodic state (a): $x = -10$; (b): $x = -6$. Morphodynamics phases: E_f (red solid), E_e (red dashed), D_f (green solid) and D_e (green dashed).

(a)



(b)

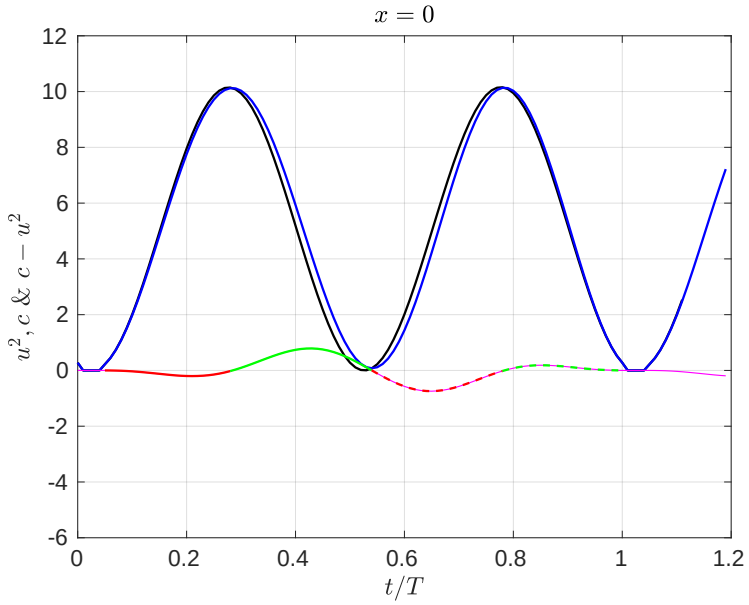
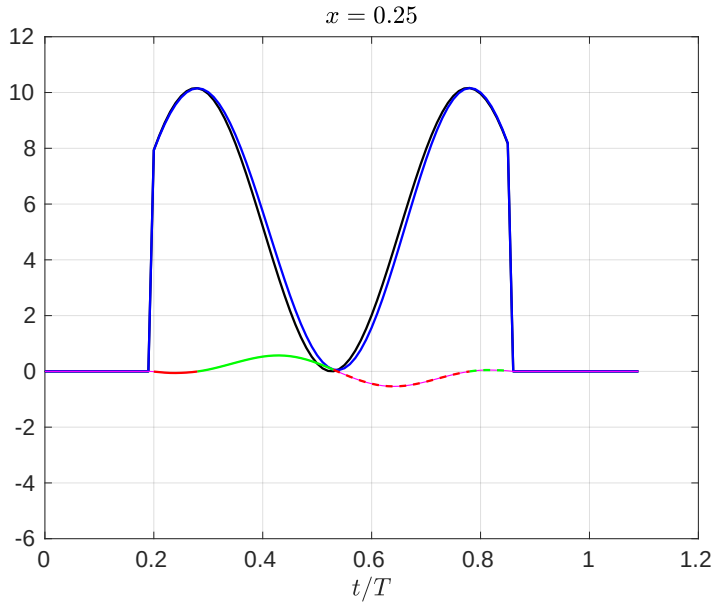


Figure 6.4: Reference test results of c (blue), u^2 (black) and $c - u^2$ (magenta) versus t/T at periodic state (a): $x = -2$; (b): $x = 0$.

(a)



(b)

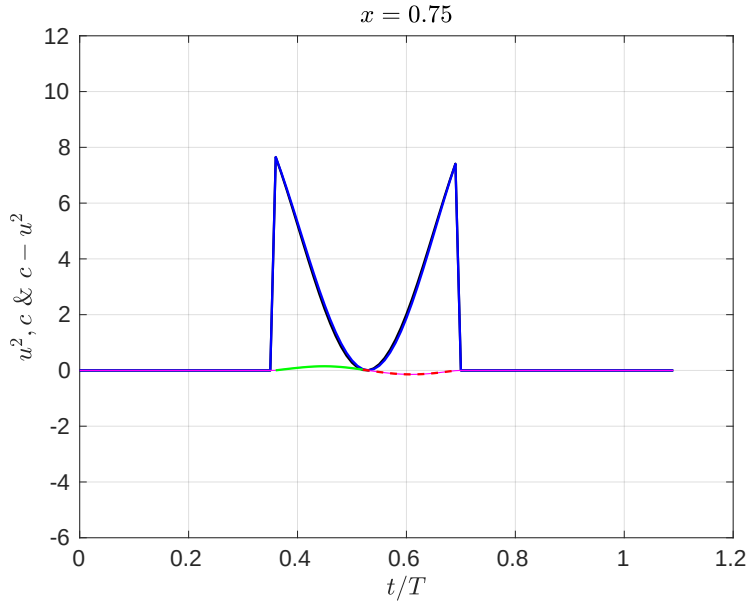


Figure 6.5: Reference test results of c (blue), u^2 (black) and $c - u^2$ (magenta) versus t/T at periodic state (a): $x = 0.25$; (b): $x = 0.75$.

We consider c and u^2 separately and the difference between these two factor $c-u^2$ as the morphodynamics aspect. Regarding u, there are two separate phases corresponding to the tidal hydrodynamics, which are flood tide on the left half (tidal current directs shoreward) and ebb tide on the right half (tidal current directs seaward) (see Fig. 6.3(a) for illustration).

The phase lag between c and u^2 are also shown in these figures. It takes a while during the increase of u^2 to start erode the sediment. And the settling of sediment only occurs after the decrease of u^2 (see c and u^2 at every position x). In comparison between different locations, the change in u^2 is very small while the phase is almost similar. There is a minor increase in the velocity as can be seen in the peak of the line. The maximum of u^2 is around $\pi^2 \approx 10$ at offshore $x = -10$ and slightly increase to more than π^2 toward the shoreline (e.g. at $x = -2$ and 0.25). This variation is very small and reflects the almost spatially constant of hydrodynamics. It again confirms that the nonlinear effects is very small, resulting the small spatial variation in the phase of hydrodynamics along the domain.

Comparing between c and u^2 along the domain, the settling lag becomes smaller toward shoreline with c also being closer to its instantaneous equilibrium state u^2. The difference between c and u^2 gets smaller in its amplitude toward the shoreline. This corresponds to the governing equation (3.49). As h becomes smaller, E/h becomes greater and c is closer to u^2 to counterbalance E/h. This agrees with reality as the suspended sediment is eroded into a small water column and thus the instantaneous equilibrium is achieved much quickly compared to a large water column. As a result, the lag effect and amplitude of $c-u^2$ are smaller toward the shoreline.

Due to the settling lag between c and u, there are two separate bed change

phases which are either deposition ($c - u^2 > 0$) or erosion ($c - u^2 < 0$). During either flood or ebb tide, both erosion and deposition in bed sediment can occur, resulting in four different morphodynamics phases. We define these four different phases based on erosional/depositional and flood/ebb tide as E_f, D_f; E_e and D_e (E and D stand for erosion and deposition of sediment; while subscript f and e stand for flood and ebb phases) as shown in different lines in the plot of $c - u^2$ (see Fig. 6.3(a) for illustration).

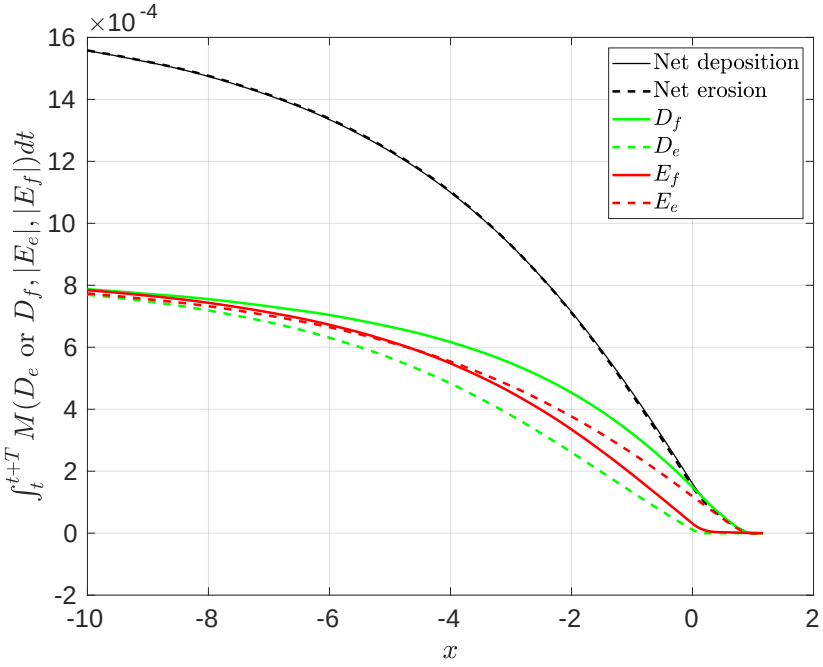


Figure 6.6: Reference test result of each morphodynamic phase over a tide $10T - 11T$ vs. x: D_f (solid green), D_e (dashed green), E_f (solid red) and E_e (dashed red).

It is also noted that due to the lag effect, the phase of these four morphodynamics phases are not the same as phase of u. For example, D_f occurs during the end of flood tide and keeps accreting after the start of ebb tide (see Fig. 6.3(a)).

Toward the shoreline, the lag effect becomes small but the phase of c always lags behind the phase of u since c is advected by u. As a result, the erosional phases always occur within either flood and ebb tide; while the depositional phases always occur during the transition either from flood to ebb or ebb to flood (see the phase difference between u^2 and $c - u^2$ in Fig. 6.3, 6.4 and 6.5).

Moving toward the shoreline, h decreases and the lag effect reduces and c becomes closer to u^2 as can be seen in the reduced gap between c and u^2 in these figures. All four phases reduce their amplitude as c is closer to u^2. However, there is no particular phase that is more dominant than the remaining and the net erosion (deposition) after a tide at offshore is not much higher than at the nearshore. As h decreases toward the shoreline, four morphodynamics phases vary. Moreover, as h decreases, its effect on c is more significant. In particular, when h is small enough, its effect on c becomes significant (see (3.49)). It means when c is closer to u^2 then the amplitude of the morphodynamics phases decrease (see $c - u^2$ in Fig. 6.3, 6.4 and 6.5). It is still unclear on the sub-tidal region since $c - u^2$ is dependent not only on h but also on E. The tidal average of each morphodynamic phase and the net erosional (depositional) flux are given in Fig. 6.6. It is noted that the results in Fig. 6.6 are obtained for one tide, i.e. $10T - 11T$, after the periodic state of c and hydrodynamics are already achieved. These values may change slightly at different tidal cycles as c and u may alter once the bed change is large enough to vary the hydrodynamics. However, within the simulation time of $100T$, the change in c and u due to the bed change is not significant.

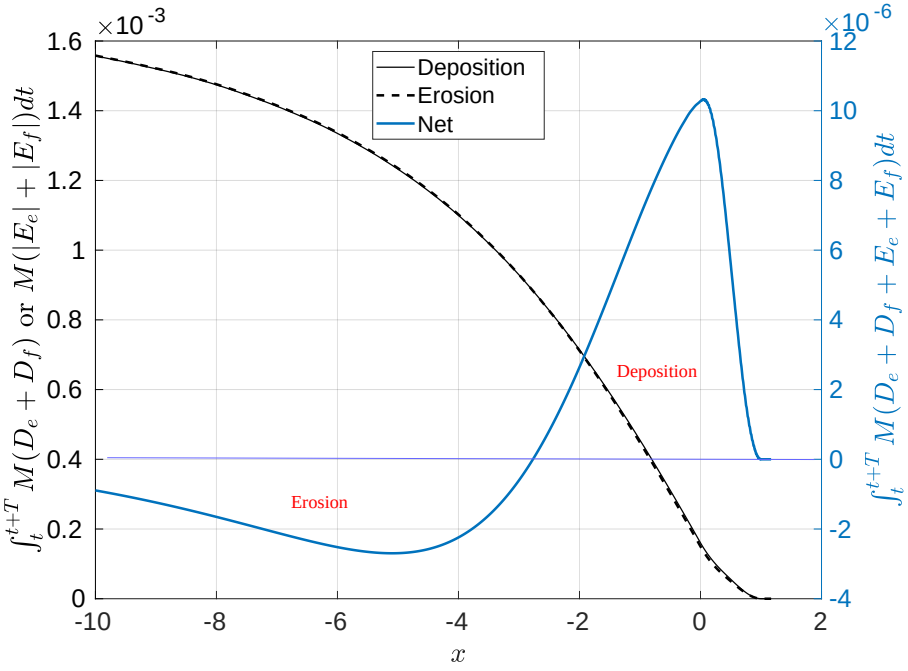


Figure 6.7: Reference test result of depositional (erosional) flux and net flux over a tide $10T - 11T$ vs. x.

As can be seen from Fig. 6.6, tidal average of D_f is the greatest; while D_e is the smallest among four phases. However, the net of erosional and depositional fluxes are quite similar with the net deposition larger toward the shoreline. In the intertidal region $x = 0-1$, D_f and E_e become more dominant than the remaining two phases; E_f and D_e decrease rapidly to zero in the intertidal region. In the intertidal region $x = 0 - 1$ (see $x = 0.25$ and $x = 0.75$, Fig. 6.5), c approaches u^2 at the transition between drying and wetting as $h \to 0$. E_f and D_e become very small in the lower intertidal ($x = 0 - 0.5$) and then disappear in the upper intertidal ($x = 0.5 - 1$) during early flood and late ebb (the region is dry thus $c - u^2 = 0$). D_f and E_e are still active due to the settling lag during submergence. c lags behind u with its peak leaning toward the ebb tide phase (see c in Fig. 6.5).

D_f becomes more dominant than E_e with longer duration and higher amplitude, resulting in sediment deposition after each tide (see $c - u^2$ in Fig. 6.5). E_f and D_e become insignificant and even disappear in the upper intertidal zone. Bed deposition is observed in the intertidal region. It is noted that varying M and/or E may affect the rate of change and/or bed change pattern. However, a depositional bed change should be observed in the intertidal region regardless value of E. We will discuss more on the effect of varying E and M in the following section.

The net of depositional and erosional fluxes over one tide are given in Fig. 6.7. Erosion is more dominant further offshore ($x < -2.5$) while deposition is observed shoreward ($x > -2.5$). It is noted that $c(t = 0) = 0$ so the sediment exchange from the bed to the water column initially; therefore, erosion is observed during the first cycle until periodic state is achieved. There is only exception in the intertidal region with deposition due to the reason discussed above. The initial bed change together with net depositional (erosional) flux over first tide $(0 - T)$ is given in Fig. 6.8. By comparing the bed change and net depositional (erosional) flux, the model's accuracy of the model can be confirmed (as shown in (3.50)). We also compare these two results at $10T - 11T$ and over the whole simulation in Fig. 6.9 and 6.10, respectively. It is noted that the bed change and net depositional (erosional) flux are in excellent agreement. There are some differences between the two lines near the intertidal region, around the peak of these lines. However, it is very small and not visible in the current resolution. This is due to the error of the interpolation and extrapolation applied for B at the shoreline, which can be improve by setting a smaller grid sizes between the interpolation/extrapolation points. The bed change after every 10 tides over 100-tides simulation are shown in Fig. 6.11.

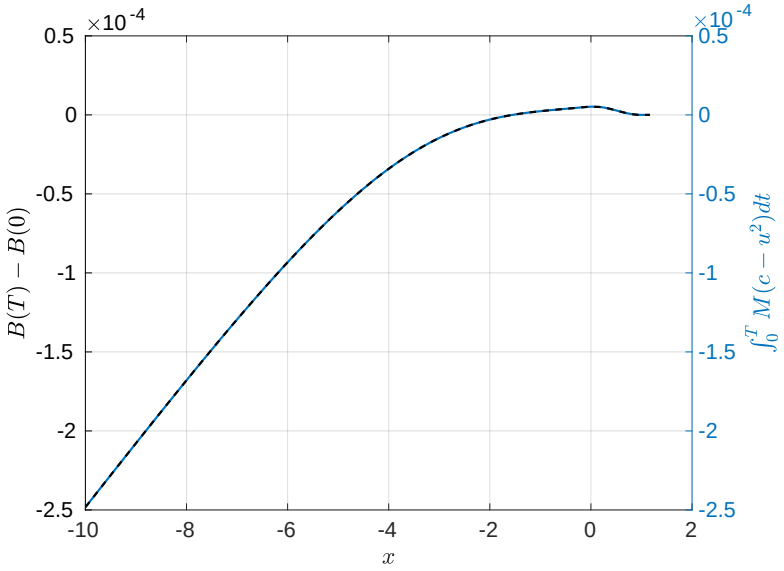


Figure 6.8: Reference test result of bed change and depositional (erosional) flux over initial tide $0 - T$ vs. x.

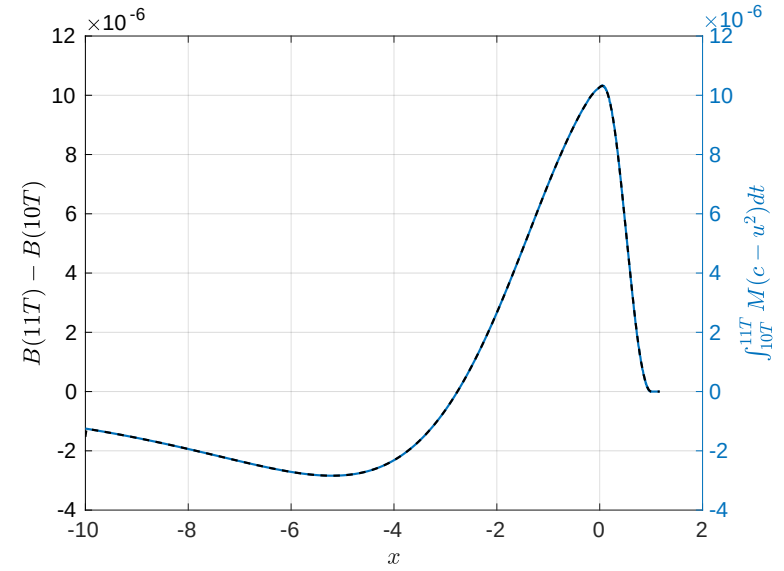


Figure 6.9: Reference test result of bed change and depositional (erosional) flux over a tide $10T - 11T$ vs. x.

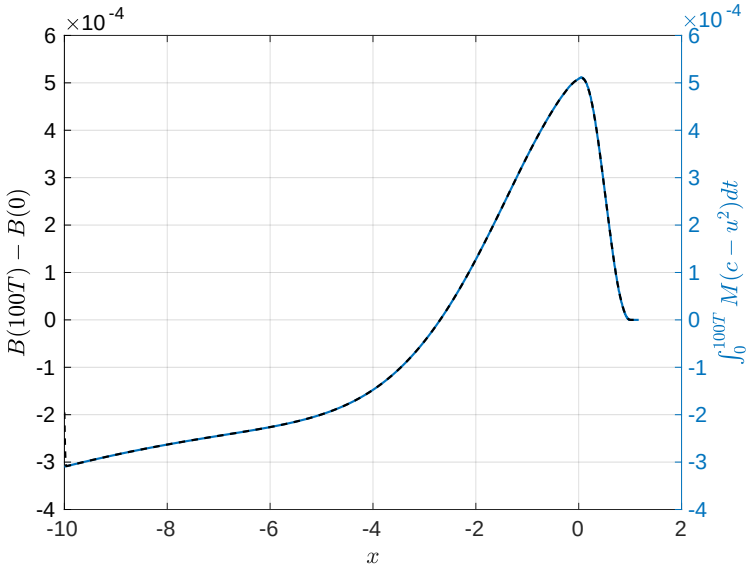


Figure 6.10: Reference test result of bed change and depositional (erosional) flux over whole simulation $0 - 100T$ vs. x.

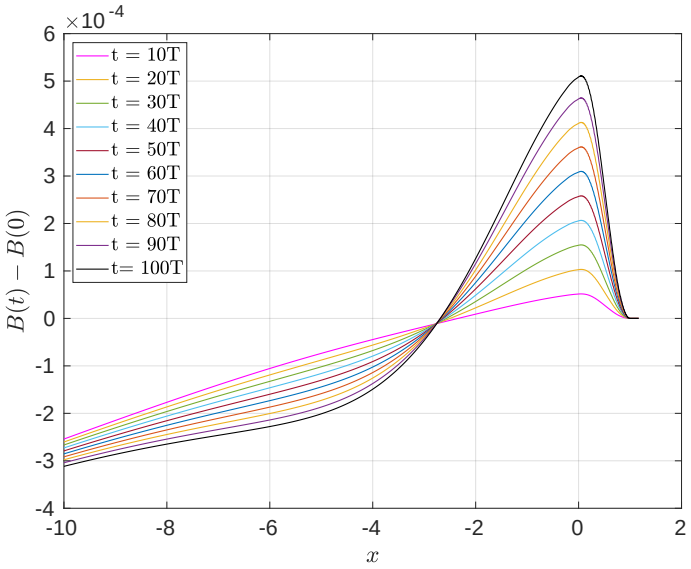


Figure 6.11: Reference test result of ΔB vs. x after every 10 tides. The bed change after 100 tides is given in solid black line.

There is significant erosion initially as sediment starts to entrain to the water column (see Fig. 6.8). ΔB keeps developing with a similar rate as shown in Fig. 6.11. It is noted that the governing dimensionless equations and hydrodynamics scale between the present model and *Pritchard and Hogg* [2003a] are similar. There are only two main differences, that *Pritchard and Hogg* [2003a] neglected spatial variations in hydrodynamics equations and they considered the erosional (depositional) formulae of cohesive sediment instead of sand as in the present model. *Pritchard and Hogg* [2003a] also assume a fixed bed in their model. However, their results on suspended concentration of cohesive sediment still illustrate some interesting findings which can be compared qualitatively to the present model. *Pritchard and Hogg* [2003a] investigated the tidal averaged of suspended sediment flux $q(x,t) = chu$ of cohesive sediment. Their findings were shown in Fig. 3 of *Pritchard and Hogg* [2003a], illustrating that there is a landward movement of muddy sediment in suspension, which decays rapidly to zero below low tide. They also pointed out that the sediment is transported from lower to upper of intertidal flats; while there is no import of sediment from offshore (below low tide level).

In this simulation, overall bed accretion occurs in the sub-tidal and intertidal region, i.e. from $x = -2.5$ to $x = 1$. For $x < -2.5$, erosion is observed. In comparison to *Pritchard and Hogg* [2003a] model, similar landward movement of the suspended sediment is also observed, resulting in erosion in the offshore region and accretion in the sub-tidal and intertidal region. The difference is that while suspended cohesive sediment is only concentrated within the intertidal region and quickly decays to zero below the low tide (see *Pritchard and Hogg* [2003a]); the suspended sand concentration is still significant offshore. The movement of suspended cohesive sediment only occurs in the intertidal region (see *Pritchard*

and Hogg [2003a]). Although *Pritchard and Hogg* [2003a] did not consider the bed change equation as well as the rate of entrainment (deposition), they still illustrate that muddy sediment is shifted from the lower to the upper of the intertidal region. In the sandy beach of this reference case, bed accretion does not limit within the intertidal region. Bed deposition is observed even outside the intertidal region.

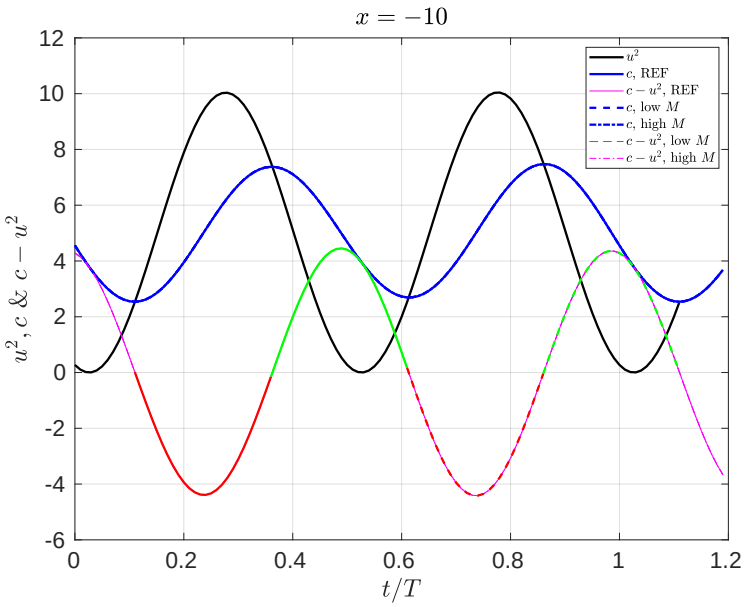
6.2.1 Effect of variation in M and E

In this section, we still consider the bed change under suspended load transport only. However, the parameters of M and E are varied against the reference test by a factor of 10. Value of E reflects the settling velocity of sediment, thus related to the sediment grain size. It also represents the exchange rate between the water column and the bed. Lower and higher values of E may lie outside the range of interest of fine sand. While E directly affects c, thus the settling lag; M only represents the rate of bed change. In particular, varying M only increases (decreases) the rate of bed change without affecting the pattern. The exception perhaps only occurs once the bed change is too significant that the hydrodynamics is varied, then advecting c. However, the main idea is to investigate how sensitive the bed change behaviour is to these parameters, and to compare it with existing literature available for cohesive sediments. These tests are defined as low E, high E, low M and high M, respectively, for further comparison with the reference test (REF).

Suspended concentration c is advected by flow velocity u and also depends on parameter E. Thus, varying M will not directly affect the solution of suspended concentration as long as the hydrodynamics are still not affected significantly

from the bed change. This is confirmed by the results of c, u^2 and $c - u^2$ at different cross-shore positions over one tide $10T - 11T$, after the periodic state is achieved (see Fig. 6.12). Results of c, u^2 and $c - u^2$ of REF, low and high M cases are almost the same as shown in Fig. 6.12. The differences are too small to visualise in the figure resolution. The bed change patterns are the same; while M only affects the rate of bed change (see Fig. 6.13, 6.14 and 6.15). The greater the value of M, the faster and greater the rate of bed change.

(a)



(b)

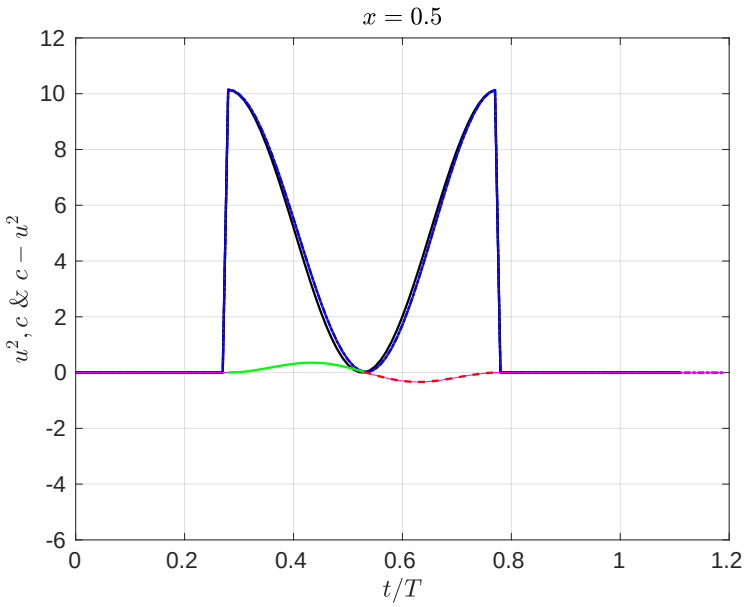


Figure 6.12: Results of c (blue), u^2 (black) and $c - u^2$ (magenta) versus t/T at periodic state of REF, low and high M (a): $x = -10$; (b): $x = 0.5$. Morphodynamics phases: E_f (red solid), E_e (red dashed), D_f (green solid) and D_e (green dashed).

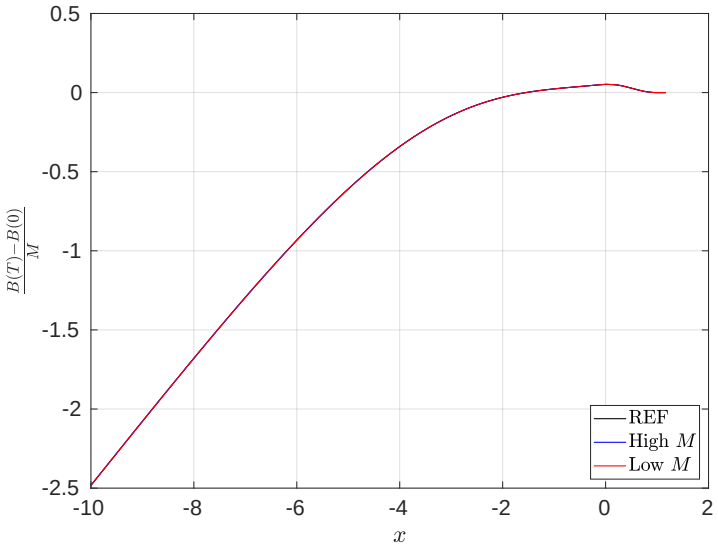


Figure 6.13: ΔB versus x over the initial tide $0-T$ for REF, low and high M

The bed change $0-T$, $10T-11T$ and $0-100T$ of these three cases are compared as function of M in Fig. 6.13, 6.14 and 6.15. The erosion for $x<-2.5$ is still observed in both M values, comparing to REF. Similarly, there is deposition of the bed for $x>-2.5$. There is only small difference in high M case; while $\Delta B/M$ in REF and low M cases are almost the same. The similarity between the three cases are due to the fact that sediment flux $c-u^2$ is not different between these cases. Varying M does not affect the bed change patterns but only increases (decreases) the rate of bed change (see (3.50)). Bed change may affect the hydrodynamics, resulting in a small difference as in high M case (see Fig. 6.14 and 6.15). However, the similarities between these three cases also illustrate the effect of bed change on the hydrodynamics being still small for 100 tides simulation. For longer simulations, bed change patterns may be different once the bed change is large enough to affect the hydrodynamics.

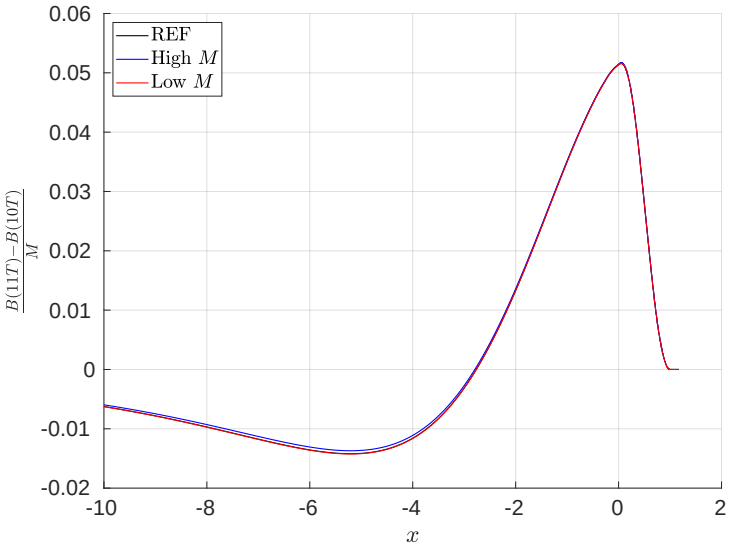


Figure 6.14: ΔB versus x over a tide after the periodic state achieved $10T - 11T$ for REF, low and high M

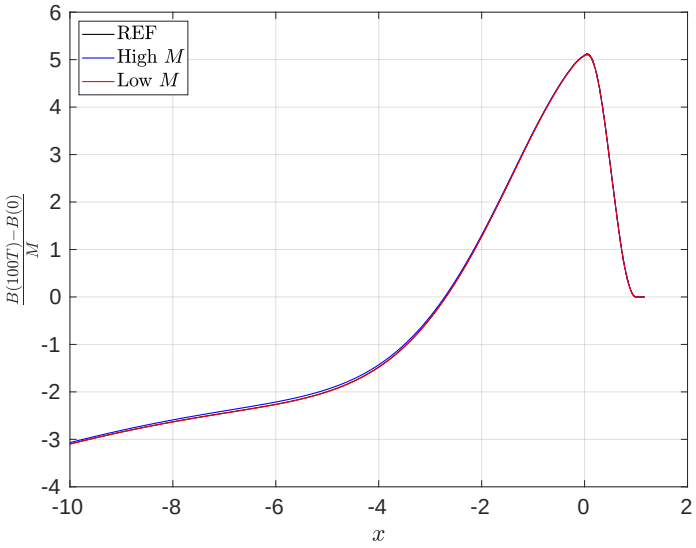


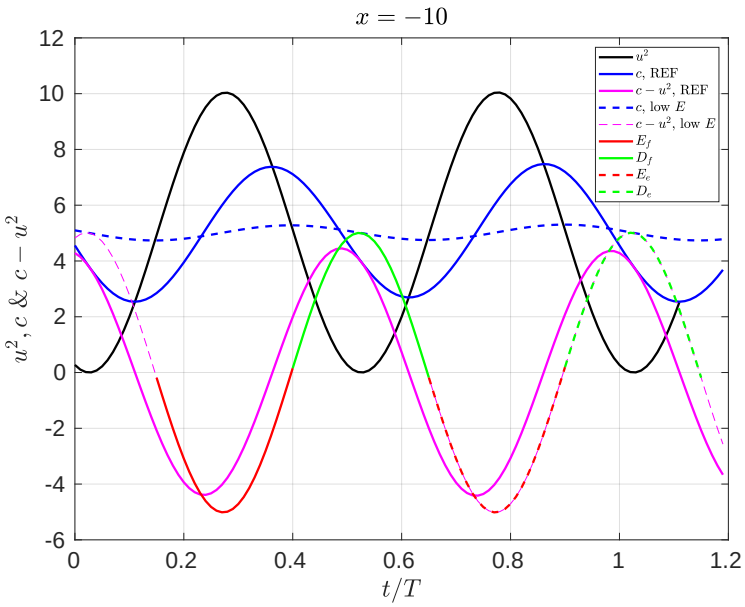
Figure 6.15: ΔB versus x over the whole simulation $0 - 100T$ for REF, low and high M

Varying E will have direct impact on c and thus the bed change patterns through $c - u^2$ (see (3.49) and (3.50)). The results of c, u^2 and $c - u^2$ for one tide from $10T - 11T$ at $x = -10$, $x = -2$, $x = 0$, $x = 0.5$ for REF and low E are shown in Fig. 6.16 and 6.17; while the results between REF and high E are shown in Fig. 6.18 and 6.19. It is also noted that we only highlight the morphodynamics phases of low and high E in these figures.

At the same position x, the larger the value of E, the smaller the lag effect observed (as can be seen in the reduced gap between c and u^2). As a result, the sediment flux curve $c-u^2$ of high E case has smaller amplitude compared to REF case. On the other hand, $c - u^2$ of low E case has larger amplitude. Since the lag effect between c and u is small in high E case, $c - u^2$ is closer to a sinusoidal pattern. D_e, D_f, E_e and E_f are more symmetrical, resulting in a very small bed change (see Fig. 6.18 and 6.19).

In low E case, c lags more behind u compared to REF and high E cases. D_e, D_f, E_e and E_f are more significant than in other cases at the same position. However, since E is small, spatial variation of c is also small (see c and $c - u^2$ lines at $x = -10$ and $x = -2$ in Fig. 6.16). As a result, the four morphodynamics phases are quite similar in both duration and amplitude. Therefore, the net of these four phases over a tide and corresponding bed change are also small. The difference in these four phases becomes significant in the nearshore region as h is more effective on c (see c and $c - u^2$ at $x = 0$ and $x = 0.5$ in Fig. 6.17).

(a)



(b)

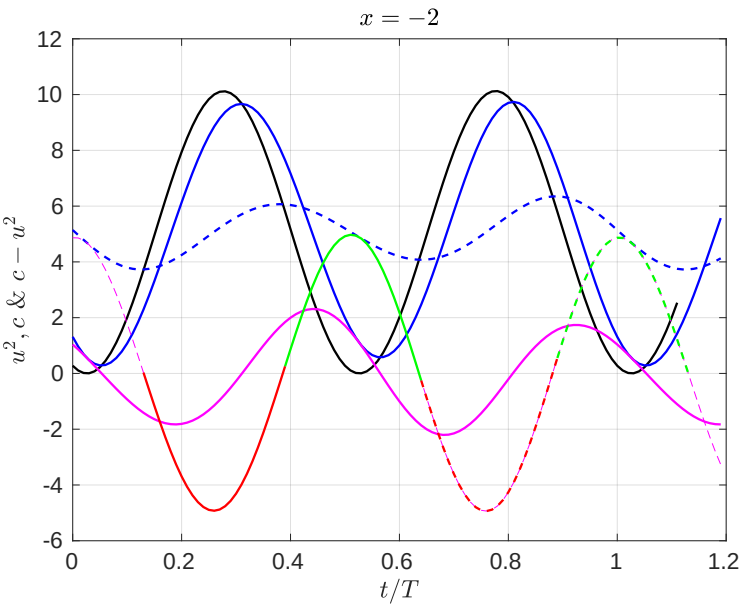
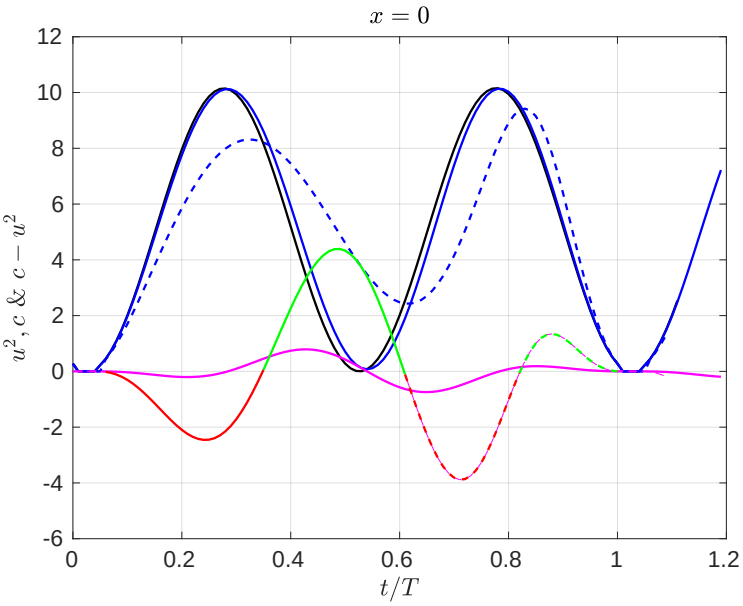


Figure 6.16: Results of c (blue), u^2 (black) and $c - u^2$ (magenta) versus t/T at periodic state of REF (solid), low E (dashed) (a): $x = -10$; (b): $x = -2$. Morphodynamics phases: E_f (red solid), E_e (red dashed), D_f (green solid) and D_e (green dashed).

(a)



(b)

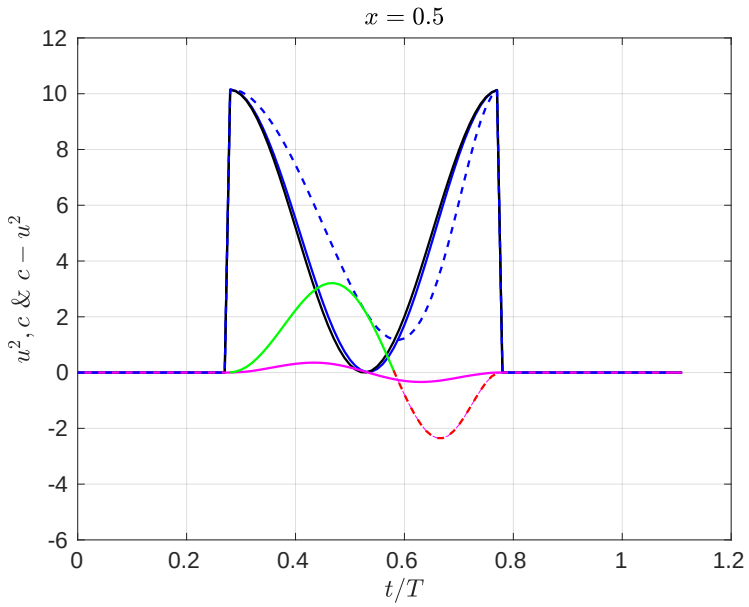
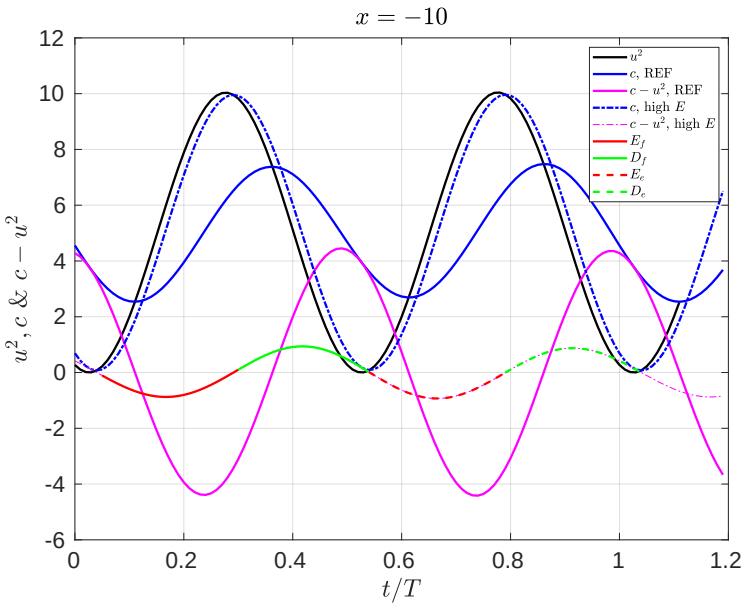


Figure 6.17: Results of c (blue), u^2 (black) and $c - u^2$ (magenta) versus t/T at periodic state of REF (solid), low E (dashed) (a): $x = 0$; (b): $x = 0.5$.

(a)



(b)

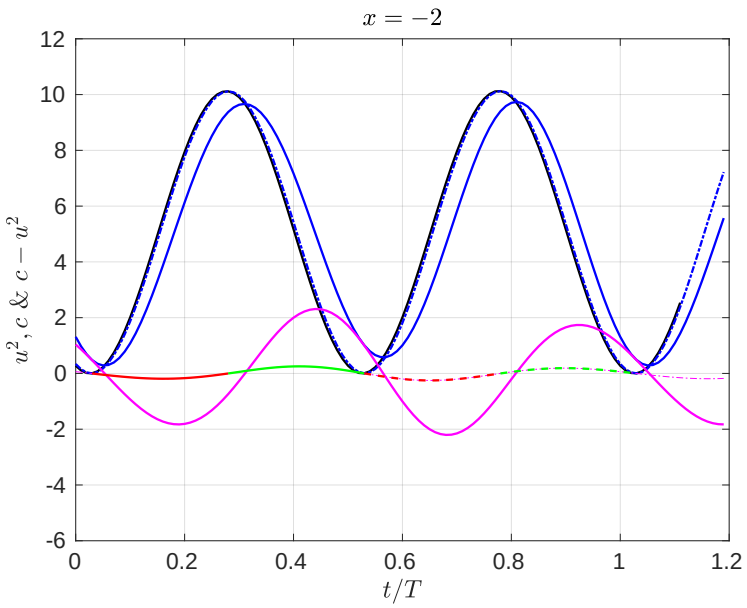
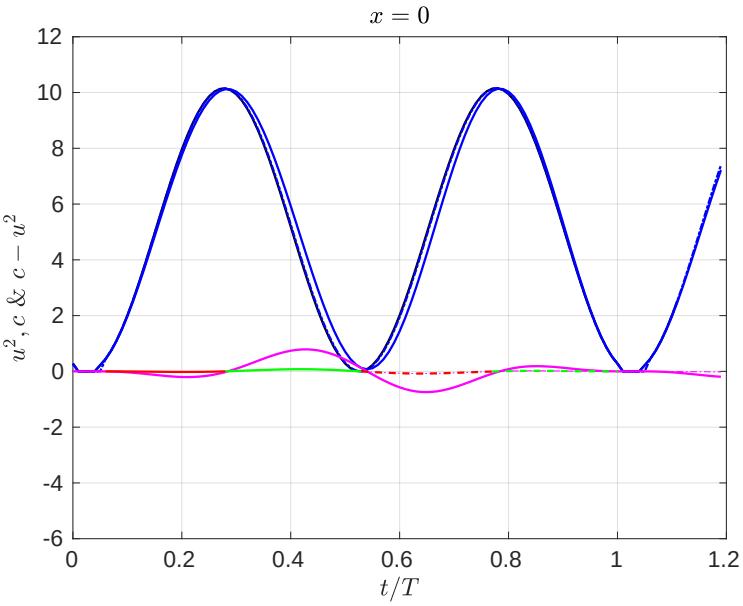


Figure 6.18: Results of c (blue), u^2 (black) and $c - u^2$ (magenta) versus t/T at periodic state of REF (solid), high E (dashed-dot) (a): $x = -10$; (b): $x = -2$. Morphodynamics phases: E_f (red solid), E_e (red dashed), D_f (green solid) and D_e (green dashed).

(a)



(b)

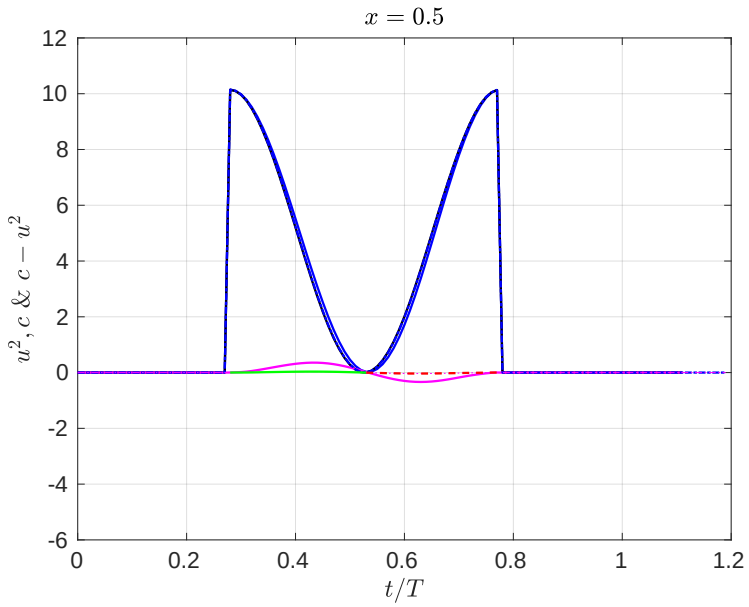


Figure 6.19: Results of c (blue), u^2 (black) and $c - u^2$ (magenta) versus t/T at periodic state of REF (solid), high E (dashed-dot) (a): $x = 0$; (b): $x = 0.5$.

Here, similar to REF case, we investigate D_e, D_f, E_e and E_f of each E case over a tide. It is noted that similar to REF case, erosion is observed initially in all cases. Sediment is eroded from the still condition. Here, we are only interested in the bed change after the periodic state of hydrodynamics and c are achieved. c, $c - u^2$ and morphodynamics phases over a tide, i.e. $10T - 11T$, are considered. The results of morphodynamics phases of low E and high E over $10T - 11T$ are shown in Fig. 6.20 and 6.21, respectively; while the net of four phases over or corresponding bed change over a tide of these two cases are shown in Fig. 6.22 and 6.23, respectively.

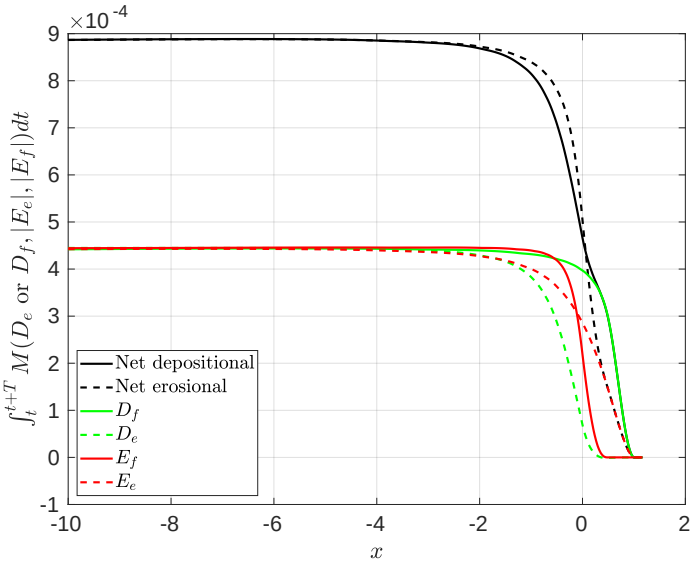


Figure 6.20: Morphodynamics phases versus x over a tide after the periodic state achieved $10T - 11T$ for low E.

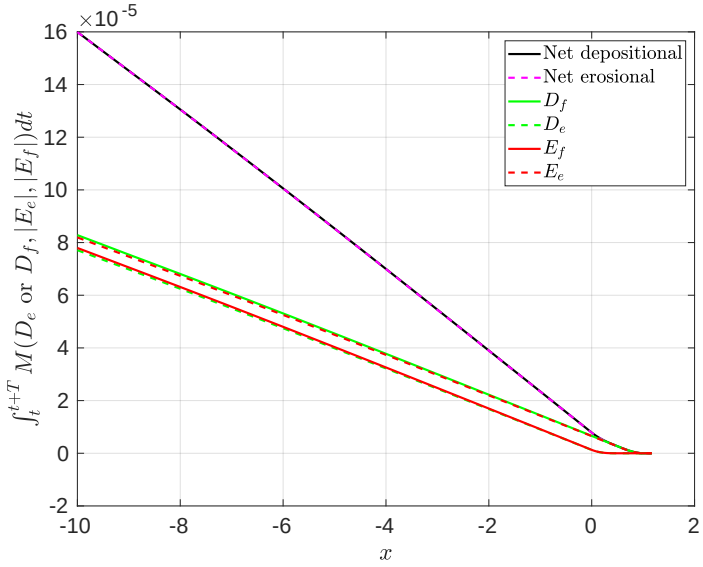


Figure 6.21: Morphodynamics phases versus x over a tide after the periodic state achieved $10T - 11T$ for high E.

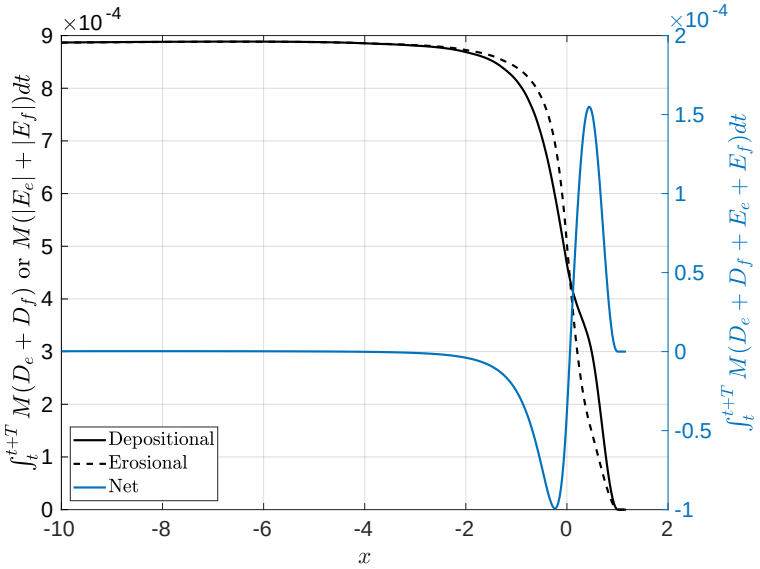


Figure 6.22: Erosional (depositional) flux and net bed change versus x over a tide after the periodic state achieved $10T - 11T$ for low E.

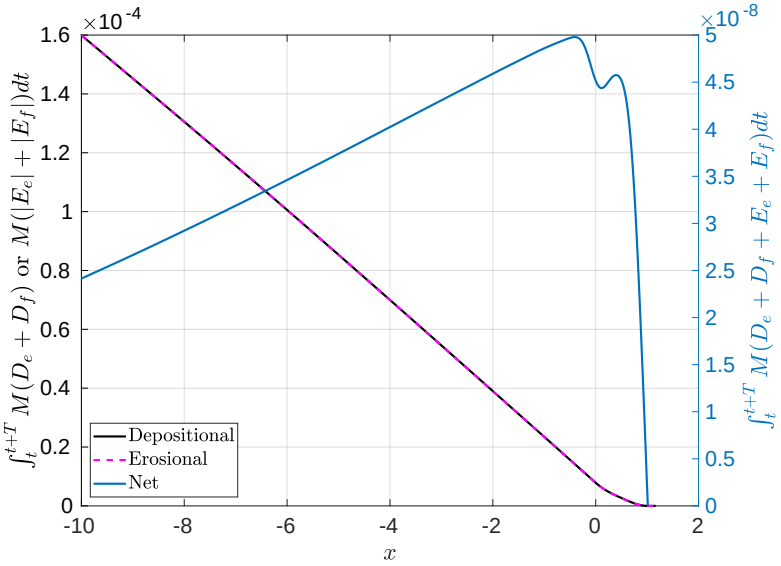


Figure 6.23: Erosional (depositional) flux and net bed change versus x over a tide after the periodic state achieved $10T - 11T$ for high E.

For lower E case, the effect of E on c is small, thus the periodic sate requires longer to achieve. The periodic state of c is only achieved after the second tide; while the others reach their periodic state within the first cycle. It is noted that c is not only advected by u but is also affected by h (see (3.49)). The effect of h on c is more significant toward the shoreline. However, at the offshore region, its effect is still small. This is shown in the small change of both amplitude and phase of $c - u^2$ at different position x (see Fig. 6.16). As a result, each morphodynamic phases are quite similar as shown in Fig. 6.20. The net depositional and erosional over a tide $10T - 11T$ at the offshore are also quite similar. The net bed change is very small at the offshore (see Fig. 6.22). Although depositional and erosional fluxes reduce rapidly toward the shoreline from $x > -2.5$ (see Fig. 6.21), the difference between depositional and erosional fluxes becomes more significant.

The net bed change over a tide is significant from $x > -2.5$. As can be seen in Fig. 6.20, E_f and D_e reduce more quickly toward the shoreline than the other two phases and even disappear in the upper intertidal region ($x > 0.5$). D_f and E_e are still dominant in the intertidal region with D_f being higher in both phase duration and amplitude (e.g. see Fig. 6.17(b) and 6.20). Bed deposition is observed in the intertidal region. In the sub-tidal region $x = -2 - 0$, while D_e reduces rapidly, E_f is still dominant and does not reduce until $x \approx -1$ (see Fig. 6.20). Bed erosion is observed in this sub-tidal region instead of deposition as in REF case.

Compared to REF case (Fig. 6.7 and 6.9), the difference in depositional and erosional flux at the offshore is smaller in low E case. Suspended sediment seems to cause significant bed change from $x > -2.5$. The change of c with space is small in low E case and the morphodynamics phases are similar in both duration and magnitude. In the REF case, sediment is shifted from the offshore ($x < -2.5$) toward the sub-tidal and intertidal region ($x > -2.5$). The depositional pattern is wider in REF case ($x = -2.5 - 1$). In low E case, bed change in offshore is insignificant, bed erosion is observed in the sub-tidal region ($x = -2.5 - 0$); while deposition occurs in the intertidal region ($x = 0 - 1$). Most of erosion offshore happens after the start of simulation as sediment starts to be eroded toward the water column. After the periodic state is achieved, the net depositional and erosional fluxes over a tide at offshore is small compared to the sub-tidal and intertidal region (see Fig. 6.22). Most of sediment is shifted from the sub-tidal toward the intertidal region.

For higher E case, the effect of E on c now becomes more significant. The periodic state is achieved after a very short time, nearly immediately after the start of simulation. c is very close to u^2, even in the offshore region (see $x = -10$

in Fig. 6.18(a)). Toward the shoreline, the lag effect becomes smaller, as does the gap between c and u^2. Compared to the REF and low E cases, the net depositional and erosional fluxes of high E is very small (see Fig. 6.23). The depositional and erosional fluxes are almost similar, with the net bed change over a tide in order of 10^{-8}, which is almost constant and can be considered as the numerical tolerance rather than a practical result. Although the bed change in high E is too small to be considered, a deposition bed change is always observed in the intertidal region. The reason is that c always lags behind u even for high E case. The higher the value of E, the closer the gap between c and u. However, the settling lag between c and u still exists as long as the region is submerged. u changes very little since non-linearities and spatial variations of hydrodynamics in tidal motion are very small. Therefore, u^2 is nearly symmetrical as u does not change much from the sinusoidal signal prescribed at the offshore. D_f is always greater than E_e while E_f and D_e decrease toward zero in the lower intertidal zone ($x = 0 - 0.5$) and disappear in the upper intertidal zone ($x = 0.5 - 1$). Deposition is observed in the intertidal region no matter what the value of E is. The smaller the value of E is, the greater the rate of bed change in the intertidal region is. The bed change for REF, low and high E over 100 tides are shown in Fig. 6.24.

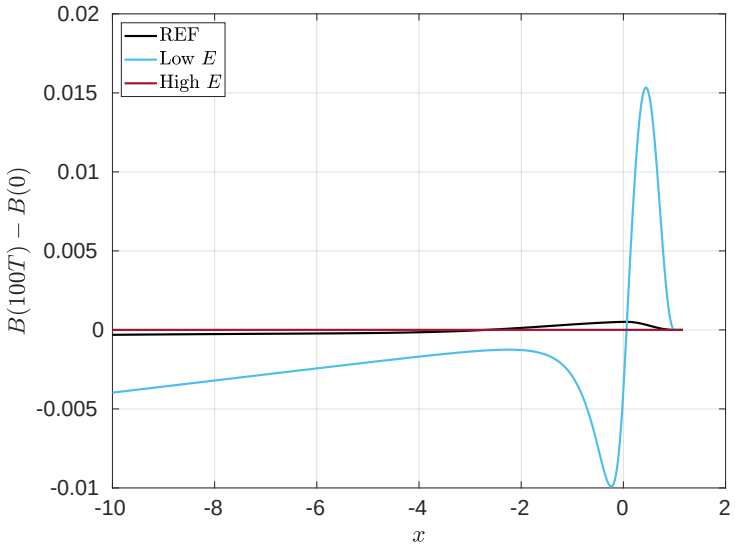


Figure 6.24: ΔB versus x after 100 tidal cycles for REF, low and high E

Bed change of high E case is too small and negligible. The bed change after 100 tides is in order of $10^{-}7$, which requires 10^4 years to obtain a significant bed change. This is impractical and thus, the effect of tidal currents on high E case is insignificant. The bed in high E can be considered as fixed as shown in Fig. 6.24. On the other hand, the smaller the value of E, the greater the bed change. Erosion is observed offshore in both REF and low E cases. However, while the offshore erosion keeps developing in REF case over the simulation time, erosion in the low E case only occurs during the first few tides as sediment starts eroding from still initial conditions. Excluding these initial cycles, the bed change in low E is only significant in the nearshore region (i.e. $x > -2.5$). In REF case, sediment is shifted from the offshore ($x < -2.5$), toward the nearshore region ($x > -2.5$). In lower E case, sediment is also shifted shoreward. However, the pattern of erosion and deposition is more narrow, with the depositional bed change being limited

within the intertidal region.

6.3 Bed load transport only

In this section, the same bathymetry and sediment physical settings are applied. However, we are now only interested in bed-load transport, i.e. $M = 0$. Here we use the MPM formulae (see *Soulsby* [1997] for more details) with and without a threshold, to investigate its effects. It is noted that *Zhu and Dodd* [2015] also point out that the velocity threshold has less effect on the sandy beach except perhaps for shingle or coarse sediment. The amount of sediment movement in both dimensional and dimensionless requires choosing value of A (see (3.25)) and thus σ (see 3.50) in a calibration to measured data. There is a relationship between A, also σ, and specific grain size. By varying the value of σ, we can relate the bed mobility to grain size and thus the bed change. It is noted that the value of A can be approximated as shown in (3.25). In the case of no velocity threshold, i.e. $u_{cr,b} = 0$, sediment is transported immediately under tidal currents as long as the flow is non-zero of velocity. As a result, the obtained q_b is probably more conservative, but does not lead to unrealistical bed change since the spatial derivatives of q_b is very small. This is due to the fact that the hydrodynamics are almost spatially constant in the tidal motion (as shown above in § 6.2). It also should be noted that in the case $u_{cr,b} = 0$, MPM is consistent with Grass formula. The physical parameters and corresponding numerical settings are given in Table 6.3 and 6.4, respectively.

The value of $\sigma = 5.0 \times 10^{-4}$ is approximated from (3.25). It is noted that this value is much smaller than values used for swash events by *Zhu and Dodd* [2015]. But swash hydrodynamics are more dynamical and also happen in much smaller

Physical Parameters	**Values**	
Friction coefficient (c_d)	0.004	
Bed porosity (p)	0.5	
Gravity acceleration (g)	9.81	ms^{-2}
Median sediment grain size (D_{50})	4.0×10^{-4}	m
Salt water density (ρ)	1027	kgm^{-3}
Sediment density (ρ_s)	2650	kgm^{-3}
Relative density of sediment (s_{rel})	2.580	
Erosional rate parameter ($\hat{m}_e$)	0.0	ms^{-1}
Critical velocity for bed load ($u_{cr,b}$)	0.0, 0.044 and 0.070	ms^{-1}
Bed load mobility parameter (A)	0.4	$m^{-1}s^2$
Bed slope ($\tan\gamma$)	0.005	
Tidal range ($\hat{H}_{tide}$) or vertical length scale ($\hat{h}_0$)	6.0	m
Tidal period ($\hat{T}_{tide}$) or time scale ($\hat{T}_0$)	4.32×10^4	s
Horizontal length scale ($\hat{x}_0$)	1200	m
Velocity scale ($\hat{u}_0$)	0.028	ms^{-1}
Concentration scale ($\hat{c}_0$)	0.035	

Table 6.3: Physical parameters of bed load test

Model descriptions and BCs	
Friction	Chézy approach
Sediment transport	Bed load only (with & without threshold)
Bed diffusion and Infiltration	Not included
Shoreline BCs	CTM, L'hôspital's rule and bed shock condition
Offshore BCs	Absorbing-generating and extrapolation
Nondimensional Parameters	**Values**
Drag coefficient (C_D)	0.8
Bed-load mobility (σ)	5×10^{-4}
Critical velocity for bed load ($u_{cr,b}$)	0.0, $\frac{\pi}{2}$ and $\frac{4\pi}{5}$
Suspended-load mobility (M)	0.0
Exchange parameter (E)	144.0
Bed slope	0.005
Tidal range (H_{tide})	1.0
Tidal period (T_{tide})	1.0
Domain length (L)	20.0
Time length	$1 \times 10^2 T_{tide}$
Spatial grid size ($\Delta\bar{x}$)	0.05
Temporal grid size ($\Delta\bar{t}$)	0.002

Table 6.4: Numerical setting of bed load test

time scale compared to tidal events. As a result, the bed sediment flux under a swash motion is much higher than that under a tidal motion. We first set $u_{cr,b} = 0$, i.e. use Grass formula, and also two non-zero thresholds. It is noted that $u_{max} = \pi$ under the prescribed sinusoidal tide. Therefore, the two threshold velocities are $u_{cr,b} = \frac{\pi}{2.0}$ (lower threshold) and $\frac{4\pi}{5}$ (higher threshold). It is also noted that for fine sand, bed load transport is not a dominant factor in tidal motion (*Soulsby* [1997]). For small sediment grain size, $u_{cr} \to 0$ as sediment is immediately suspended into the water column and most of sediment is transported under the mean of suspended load. However, the contribution of bed load transport becomes more important as D_{50} increases. For grain size $D_{50} = 4.0 \times 10^4$ (Table 6.3) the Shields diagram indicates sediment transport by bed and suspended load (*Allen* [1985]). Although most of the sediment transport in the range of fine sand is suspended load, we still retain bed load transport to investigate its contribution toward the final bed change and the effect of velocity threshold on the bed change.

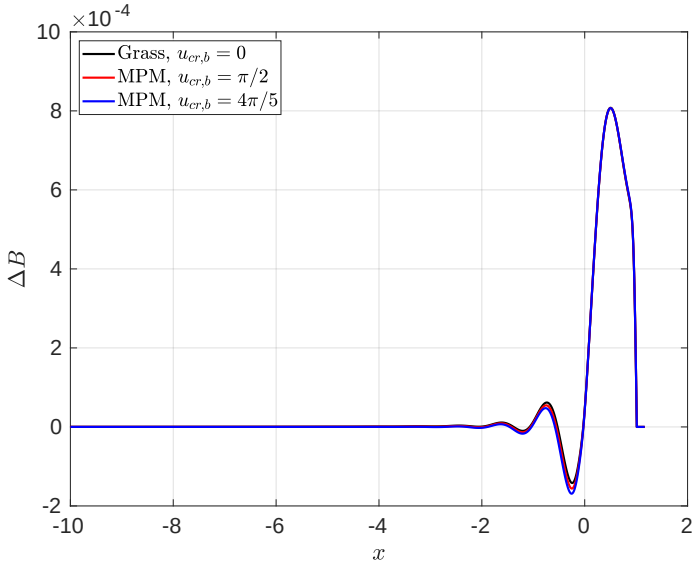


Figure 6.25: ΔB vs. x over 100 tides under bed load only, different velocity thresholds.

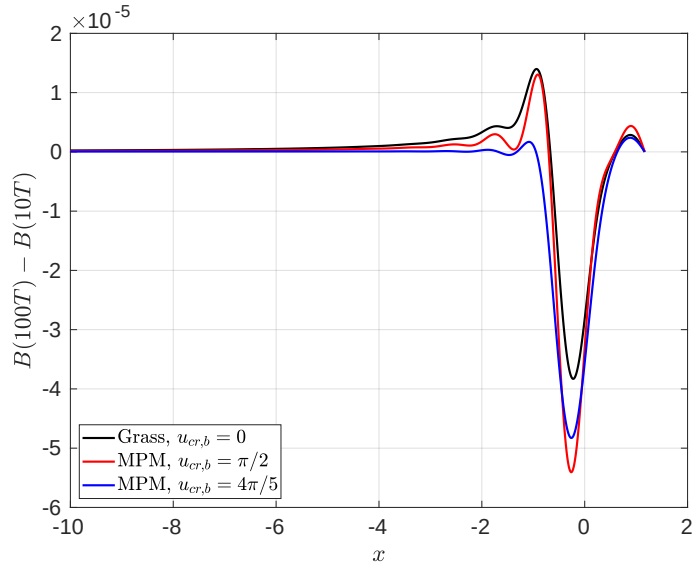


Figure 6.26: $B(100T) - B(10T)$ vs. x under bed load only, different velocity thresholds.

We make further investigation on the bed change due to bed load transport. Fig. 6.27 shows the bed change after a tide, i.e. $0 - T$, $T - 2T$ and $10T - 11T$. It is also noted that we only investigate the bed change under Grass formula since the velocity threshold has no significant effect on the bed change. Here, bed change after the first tide is much higher than the remaining. It is due to the transient from still condition, which leads to some small oscillation in the velocity field. As a result, the bed change under bed load transport during the first cycle is much higher than the remaining.

We make further comparison of the bed change after a tide from $10T - 11T$, $50T - 51T$ and $99T - 100T$ of Grass formula. The rate of bed change due to Grass bed load transport reduces its magnitude tides after tides as shown in Fig. 6.28. This is different from the suspended load case. Bed change under suspended load occurs due to the settling lag effect between c and u. Since bed change is not significant enough to cause a great effect on c and u, bed change keeps developing at a similar rate tide after tide, as in the REF case. Here, if we only consider the bed change after $10T$, i.e. the periodic state of c and hydrodynamics are already achieved, the bed change under bed load transport is much smaller than that for suspended load (comparing between Fig. 6.10 and 6.28). The bed change over a tide is in order of 10^{-5} in suspended REF case and of 10^{-7} in Grass formula case. It means the bed change under bed load transport is about ten to hundred times smaller than under suspended load regarding fine non-cohesive sediment. Bed erosion occurs at the lower intertidal region under bed load; while deposition is always observed within the intertidal region under suspended load.

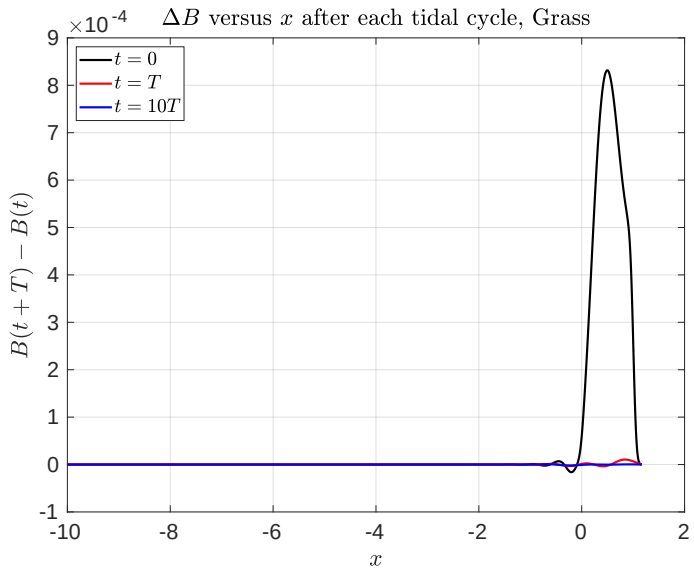


Figure 6.27: Bed change vs. x over a tide under bed load only, Grass formula: $0 - T$, $T - 2T$ and $10T - 11T$.

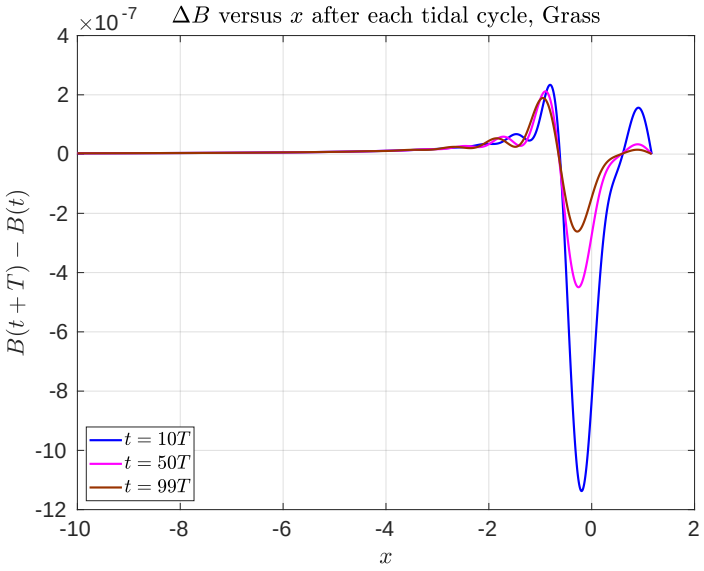


Figure 6.28: Bed change vs. x over a tide under bed load only, Grass formula: $10T - 11T$, $50T - 51T$ and $99T - 100T$.

It is also noted that most of the bed change due to bed load occurs near the intertidal region. Most of the bed change due to bed load transport occurs within the first few cycles, while bed change after each tide is very small (i.e. bed change at $10T - 11T$ is about 1000 times smaller than that at initial tide) and also decreases with time (see Fig. 6.28). As a result, the bed change due to bed load transport develops toward its equilibrium in a very short time compared to the suspended load. This is because u is almost spatially constant in the tidal motion. The nonlinear effects seems to be very small and thus the spatial derivative of bed load sediment fluxes $\xi q_{b_x} = 3\sigma(u^2 - u_{cr,b}^2)u_x \approx 0$, resulting in very small bed change throughout the domain. Due to a spatially constant velocity field, the power-law based sediment transport formula such as Grass, Van Rijn or MPM formulae (see *Soulsby* [1997]) yield a constant value throughout the domain at any specific time. As a result, the bed change due to bed load transport are very small throughout the domain. The bed change is due mostly to the shock condition applied to bed level at the wetting-drying interface (see § 4).

It is also noted that the equilibrium state of bed level develops quickly in bed load transport cases. The bed change after each tide is non-zero but very small compared to that over initial tides as shown in Fig. 6.27. Moreover, bed change over each tide keeps decreasing as shown in Fig. 6.28. Here, we compare the contour plots of ΔB at $19T - 20T$ and $99T - 100T$ (see Fig. 6.29). The difference is very small. It suggests that shock conditions develop the bed shape right after the initial tidal event as can be seen in the bed change during $0 - T$ (Fig.6.27). After that, the bed change is very small and reduces tides after tides (Fig. 6.28). The equilibrium state is quickly achieved under bed load transport.

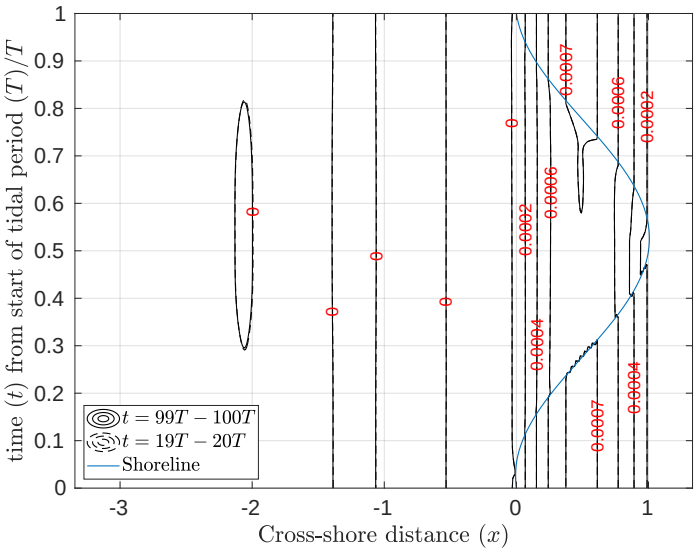


Figure 6.29: Contour plot of ΔB over a tidal cycle $19T - 20T$ and $99T - 100T$

The bed change due to bed load transport occurs mainly after first few cycles under the bed shock condition, in which bed deposition is observed together with the flooding process initially. Here, we test whether or not the bed change patterns is dependent on initial tidal level. It is noted that the initial tidal level does not affect the bed change under suspended load but the pre-suspended sediment concentration. Here, we test the effect of different initial tidal level and in all cases, there are some difference in the final bed changes but not significant. The bed level in all cases are quite similar as shown in Fig. 6.30. Results indicates that bed change is affected by the initial tidal level, but not significantly.

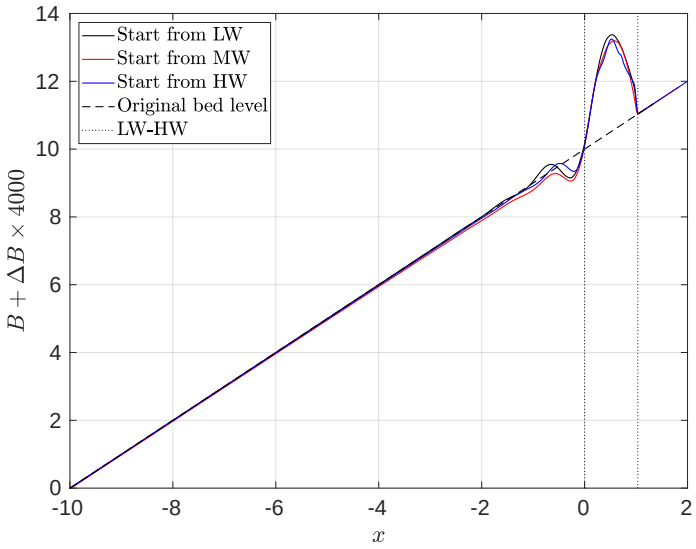


Figure 6.30: Bed level at $t = 100T$ due to bed load transport only (Grass formula) with different initial conditions ($\sigma = 5 \times 10^{-4}$).

6.4 Combined load transport

We consider both bed-load and suspended-load transport to see how each mode contributes to ΔB in 100 tidal cycles. Since the velocity threshold of bed load $u_{cr,b}$ has little effects on the bed change, we employ Grass formula as bed load transport. We define these combination modes as Grass + REF, Grass + low(high) E and Grass + low(high) M (see § 6.2 and § 6.3 for details of numerical settings). The final bed change after 100 tidal cycles for all cases is given in Fig. 6.31.

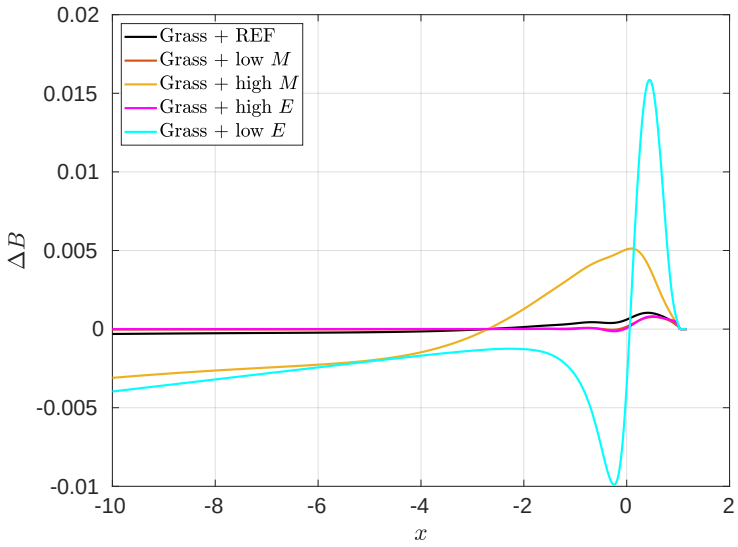


Figure 6.31: ΔB vs. x at $t = 100T$ under combined load transport.

As can be seen from Fig. 6.31, bed change in (Grass + low M) case and (Grass + high E) are very small. It is noted that bed change under suspended load only of low M and high E cases are very small (see § 6.2). Most of the bed change in combined mode of these two cases occurs near the intertidal region and mainly due to bed load transport.

We now consider the combined mode of Grass + REF only to see how each mode contributes to the final bed change (Fig. 6.32). It is noted that the numerical settings in Grass and REF are derived for fine sand. Here, the bed change in upper intertidal region ($x = 0.5 - 1$) under combined load is controlled by the bed load transport as the bed change in this region is similar to that under bed load transport only. Outside the intertidal region, the suspended load becomes more dominant and its contribution to the bed change becomes more important.

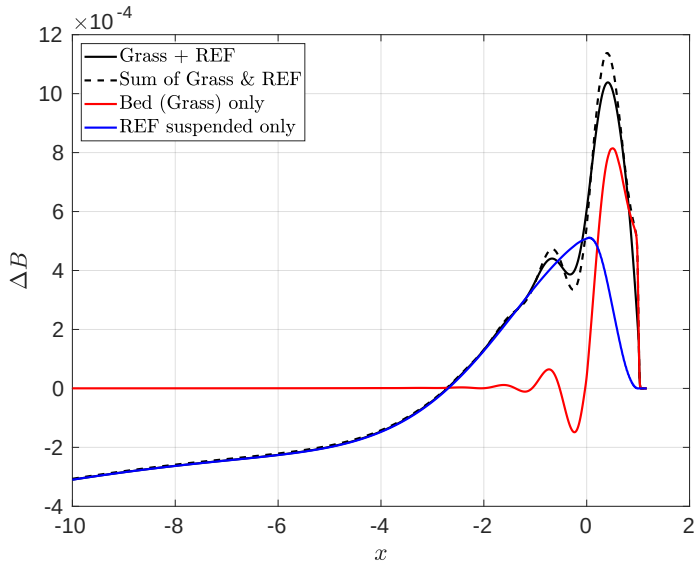


Figure 6.32: Combined load of Grass and REF: ΔB vs. x at $t = 100T$.

For each case, we also compare the bed change under combined mode vs. the sum of separate modes. In the fully coupled model, the hydrodynamics and bed change are altered simultaneously. As a result, the bed change is not in general the same under combined load and sum of separated modes. The difference may be significant if bed mobility is high (i.e. large value of M or σ) so that the feedback of morphodynamics toward hydrodynamics is high (see *Zhu and Dodd* [2015] for more details). Here, we only compare these loads for Grass + REF, Grass + high M and Grass + low E cases in Fig. 6.33. As can be seen from Fig. 6.32, the difference between the combined load and sum of individual loads is only visualise near the sub-tidal and intertidal region (i.e. $x = -1 - 1$). Although the difference is small, it still suggests that the summation of individual modes is greater that the combined load transport, resulting in a higher bed change in the nearshore region.

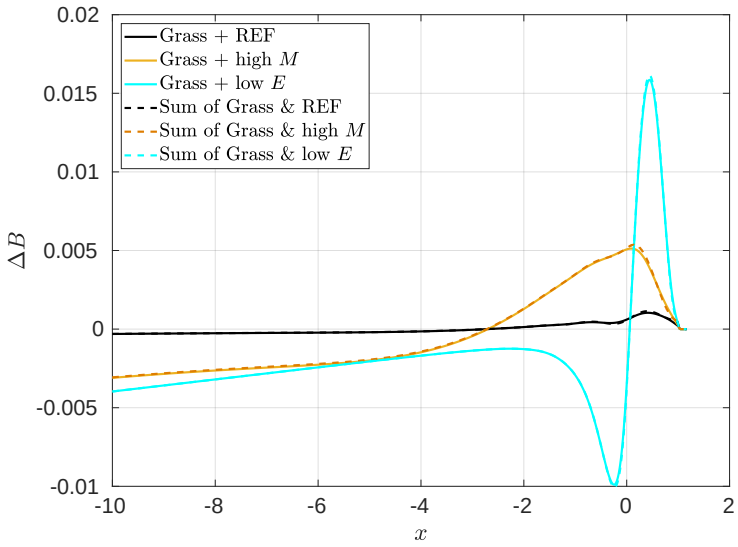


Figure 6.33: Comparison between combined and the sum of individual modes of transport: ΔB vs. x at $t = 100T$.

6.5 Fully-coupled versus quasi-coupled hydro-morphodynamics model

The present model is fully-coupled. Therefore, feedback of the morphodynamics onto the hydrodynamics occurs at every time step. Here we compare the fully-coupled model against the quasi-coupled, in which B is updated after every tidal cycle, to investigate how the coupling affects bed change. It is noted that a quasi-coupled model is applied in study of cohesive sediment of *Roberts et al.* [2000]. The bed change is only updated after every tidal cycle. In *Pritchard and Hogg* [2003a], they only focus on suspended sediment concentration without taken effects of the bed change into account.

As discussed above, the bed change under bed load transport is only significant

in the intertidal region. Moreover, most of the bed change is likely due to shock conditions applied at the shoreline boundary. This requires the bed level along with the shoreline position to be updated at every time step and thus is only appropriate with fully-coupled model. Here, we still calculate $\int_t^{t+T}(q_b)_x$ and only update B after each tide to obtain the result under bed load transport only. However, the shock condition is not applicable in bed level at the shoreline after a tide. The hydrodynamics along with the advection equation for suspended concentration are solved. The entrainment/deposition flux is averaged every tidal cycle and bed change is updated then only.

The bed change under all five cases of suspended load, i.e. REF, low (high) M and low (high) E, after 100 tidal cycles by fully and quasi coupled model are given in Fig 6.34, 6.35, 6.36, 6.37 and 6.38, respectively. As can be seen in all cases, qualitative agreement is observed for bed changes under both quasi and fully-coupled models. Either erosion or deposition are predicted similarly by quasi coupled as well as by fully coupled model. There are not much difference between the prediction by both models, particularly for low M and high E cases (Fig. 6.35 and 6.38, respectively). The reason is that the bed changes in these cases are very small so that the feedback onto hydrodynamics are small too.

The greater the bed change, the greater the difference between the two models, as can be seen in the cases of high M and low E (see Fig. 6.36 and 6.37). The difference becomes significant toward shoreline. The bed change in this region is greater so that its feedback onto hydrodynamics is also more significant than that offshore. It is noted that the quasi-model is overestimated in high M and REF cases, but underestimated in low E case compared to fully-coupled results. The difference between these two models suggests that feedback from the bed change

onto hydrodynamics is significant, particularly in the sub-tidal and intertidal regions. Moreover, for the case of high bed mobility, the coupling effect becomes more important.

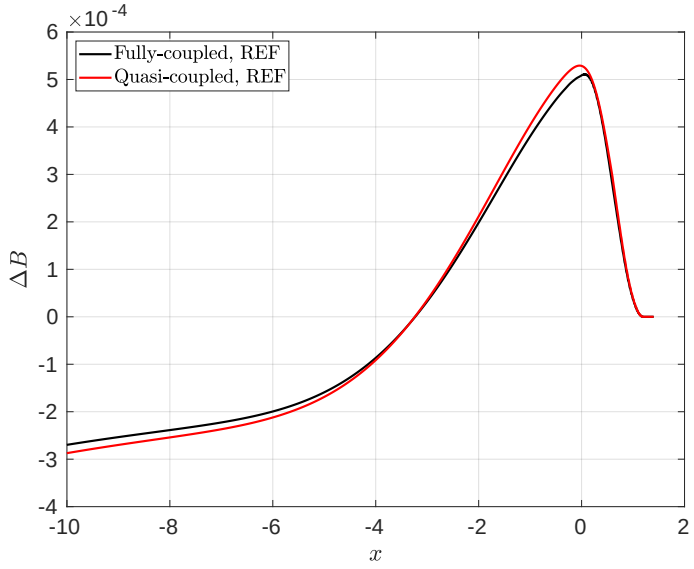


Figure 6.34: Coupling test: ΔB vs. x after 100 tides under REF case.

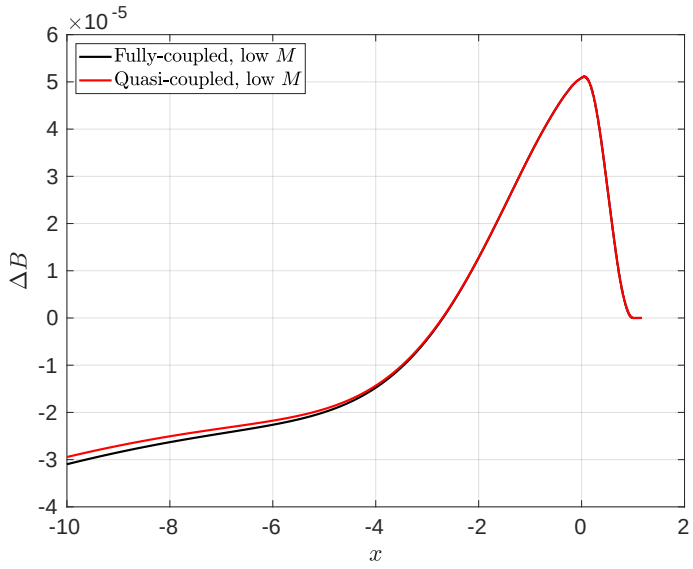


Figure 6.35: Coupling test: ΔB vs. x after 100 tides under low M case.

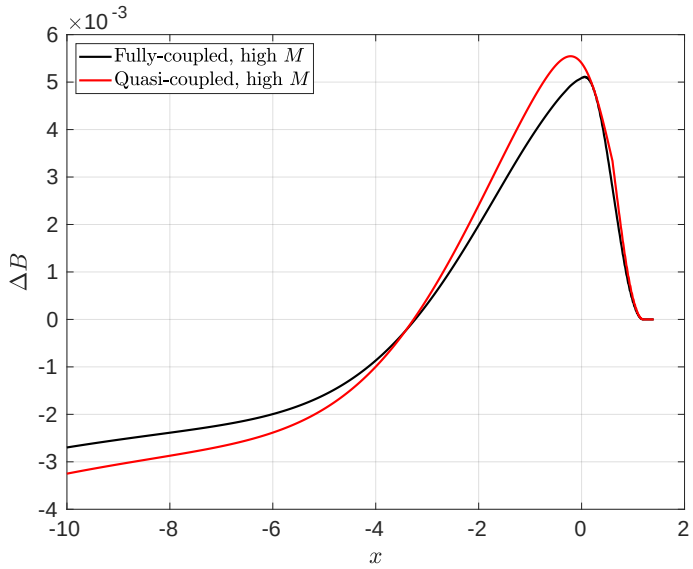


Figure 6.36: Coupling test: ΔB vs. x after 100 tides under high M case.

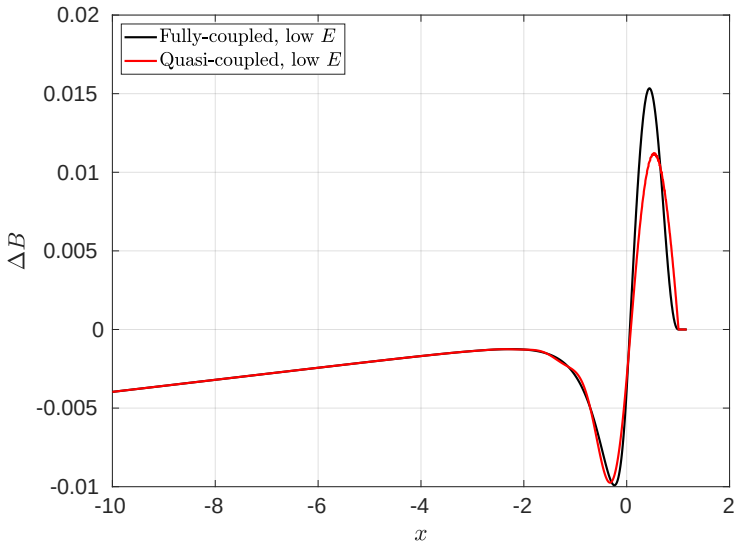


Figure 6.37: Coupling test: ΔB vs. x after 100 tides under low E case.

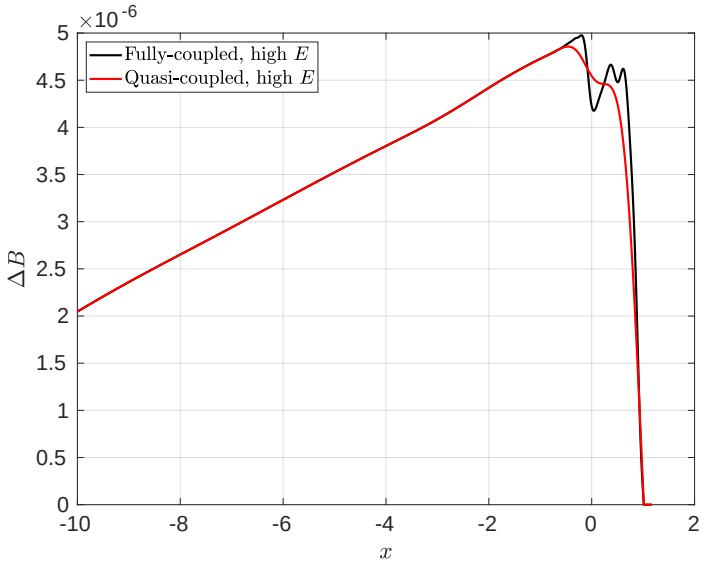


Figure 6.38: Coupling test: ΔB vs. x after 100 tides under high E case.

Regarding bed load transport only, we compare the fully-coupled and quasi-

coupled models for Grass formula only. The results of two models are shown in Fig. 6.39. Bed changes obtained by fully- and quasi-coupled models are much different, with that of the former being about 100 times larger than the latter. In tidal motion, bed flux $q_b = u^3$ is almost spatial constant due to very small spatial variation of u (see §6.2). As a result, the bed change due to bed load transport (function of $(q_b)_x$) is small too. Most of the bed change under bed load occurs near wetting-drying boundary due to shock condition applied at the shoreline. It is noted that the shock condition in bed level is applicable in the fully-coupled model, at every time step, once the shoreline velocity and position are known. The shock in bed level at the shoreline is not included since the bed level is not considered at every time step. This is difficult to implement into quasi-coupled model since the bed flux and bed level are only updated after each tide. The agreement between two models in bed load is much less than in suspended load.

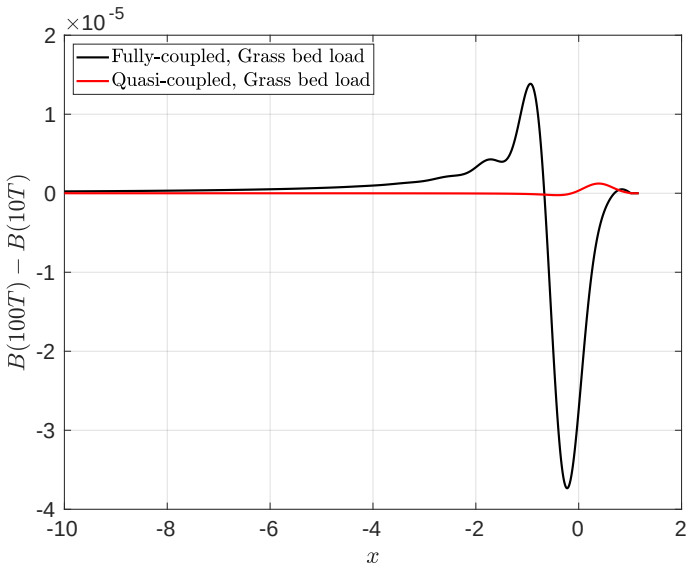


Figure 6.39: Coupling test: ΔB vs. x after 100 tides under bed load transport only, Grass formula.

CHAPTER 7

Conclusions and Recommendations

This work has focused on simulating and understanding the flow and bed evolution under macro-tidal current during multiple tidal events using fully-coupled simulations. The first step was developing fully coupled models by coupling the 1D NSWEs with the suspended sediment advection equation and bed evolution equation. For the first time, the coordinate transformation method has been employed in morphodynamic model to deal with the moving boundary in wetting-drying of the shoreline. The model has been verified in many aspects including both hydrodynamics and morphodynamics of single and multiple events. The robustness and stability of the model have been confirmed against well-known analytical and numerical solutions available from previous studies.

The offshore boundary conditions are also developed to allow absorption and generation of both hydrodynamic and morphodynamic waves. Performance of the offshore boundary conditions and CTM have been verified and confirmed against

numerical solutions.

The bed evolution under tidal currents is caused by sediment transport in the form of bed and suspended load. The fully coupled model allows us to investigate these modes of transport separately and in combination. Therefore, the contribution of these modes on bed change is investigated.

7.1 Suspended-load only

The bed evolution due to suspended load under sinusoidal tidal signals is examined with a series of different bed mobility M and exchange rate E parameters. Bed change patterns are also similar to the cohesive sediment case of *Roberts et al.* [2000], with bed deposition being observed in the intertidal region over tides. These are mutually proportional with varying M. However, high M case yields a slightly different pattern at offshore compared to REF and low M cases. This is primarily because high M results in significant bed change and thus the feedback on hydrodynamics is also more significant than REF and low M cases. The difference keeps increasing with time, however it is still small over simulation time of $100T$.

While M only affects the rate of bed change, bed change patterns vary with E. Erosion is observed in the sub-tidal region in the low E case, but not in REF and high E cases. However, bed deposition always occurs in intertidal region, no matter what the value of E is. It is also noted that the magnitude of bed change in the low E case is in the same order as high M case although the value of M is ten times smaller.

There are some interesting findings in the results of suspended-load transport. Firstly, the hydrodynamic is almost spatially constant. The spatial variation of

phase and magnitude of h and u is very small. This is because of the global Froude number in non-dimensional form, reflecting the flow regimes, which is very small. Therefore the spatial derivatives of $(h + B)_x$ approach zero to balance the term $1/F^2$.

The tidally averaged bed change due to suspended-load under sinusoidal hydrodynamics, however, is non-zero. It is due to the lag effect of suspended sediment concentration with respect to velocity. c lags behind u and this lag effect is a function of both E and h. Since h varies within cross-shore locations, the lag effect changes with E and x. In particular, the smaller the value of E, the greater the lag effect. In contrast, the smaller the water depth, the smaller the lag effect.

The settling lag effect is the main reason for a non-zero bed change over tides. There are four different morphodynamics phases, corresponding to the deposition/erosion during flood/ebb tide. The variation of these four morphodynamic phases are also function of E and h. During early flood and late ebb tide, the sediment starts to be eroded into the water column and settled down onto the bed. In the nearshore region, since h is small, the lag effect gets smaller toward the shoreline. This lag effect increases together with rising h during flooding. As a result, two phases during early flood and late ebb become smaller toward the shoreline while those phases in late flood and early ebb are still active. Moreover, since c always lags behind the nearly sinusoidal u, the depositional phase in late flood is always more dominant than the erosional phase in early ebb, resulting in bed deposition in the intertidal region.

Bed change patterns after one tide and multiple tides are the net of these four difference phases. It is noted that for REF and low(high) M cases, since the value of E is unchanged, the lag effect between c and u is almost the same. This

is true for simulation time of $100T$. However, for longer simulation time, once bed change significantly affects the hydrodynamics, lag effect between c and u is different in these cases, resulting in a different bed change pattern. This variation will occur in high M case much earlier than REF and low M case as bed change rate is proportional to M. In fact, a small difference in c and u in high M case compared to REF and low M case is already observed within $100T$ simulation time.

The variation of E directly affects the lag effect between c and u, resulting in the difference of four morphodynamic phases. Compared to REF case, low E has a greater lag effect, and thus a higher bed change magnitude. On the other hand, in high E case, the lags of c and u are very small even further offshore. Although lag effect still exist, it is close to sinusoidal phase of u, thus the four morphodynamic phases are balanced together, resulting in a very small bed change over each tide and thus, over simulation time.

7.2 Bed-load only and Combined mode

Bed change under bed-load only is also examined under the same hydrodynamics and bathymetry conditions. In contrast to the considerable and continuously developing bed change over tides of suspended-load only, bed change under bed-load only of considered grain is much smaller, with the contribution over a tide being about 100 times smaller than that of suspended-load only (after the periodic state is achieved). Moreover, we examined the effect of bed load threshold on the bed change. Effect of the threshold on the bed change over a tide and simulation time of $100T$ is very small. Bed change magnitude and pattern are similar with different threshold cases.

Bed change under bed load only is only significant during first few cycles with the rate decreasing rapidly after the first tide. Bed load transport formula of MPM is a function of u. The small spatial variation of u results in a small spatial derivative of q_b. Therefore not only is the bed change due to bed load only over a single tide small, but so is that over whole simulation. Most of the bed change is due to shock condition applied at the shoreline after the first few tides. Bed change in the intertidal region is much more significant compared to the other region. After the first few tidal cycles, bed change under bed load only is mainly due to the small spatial variation of u. This is primarily because of the non-linearity effect of NSWEs, which still exists in tidal motion. Bed change under bed load only decreases gradually over time and seems to be converged toward an equilibrium state; while bed change under suspended load only continues developing over time. Moreover, if excluding the first few cycles, in which bed change is mostly due to the transient from still water condition, bed change due to bed load only is much smaller than that due to suspended load (in comparison between REF and Grass cases).

Bed change under combined mode of load transport is quite similar to the summation of bed change under individual mode, but not exactly the same. There is still some small difference between bed change under combined mode and the sum of separated modes. The difference is proportional to the rate of bed change, i.e. high M and low E cases compared to the other cases. The difference, however, is not significant and illustrates that the summation of individual modes are lightly overestimated with greater erosional and depositional peaks compared to those under combined mode.

7.3 Coupling effect

We also investigate the coupling effect on morphodynamical modelling of tidal motions. The results of the fully coupled model is compared to that obtained by the quasi-coupled model. In the quasi-coupled model, the hydrodynamics and concentration are solved simultaneously as in fully-coupled model, with the only difference being that the bed level and any feedback on the hydrodynamics are only updated after every tide. Bed change patterns in both models with erosion and deposition are predicted quite similarly. In small bed change rate, i.e. low M and high E cases, the difference between the two models is very small. This is because the feedback onto hydrodynamics due to bed change in these cases are minimal. The difference, however, becomes significant in REF, high M and low E cases as the bed change after each tide is significant and so is the feedback to hydrodynamics. These alterations in hydrodynamics are updated simultaneously in fully-coupled model but not in quasi-coupled model, resulting in the difference. This difference is more significant in the nearshore region, i.e. the intertidal and sub-tidal region. This is probably because of the effect of bed change on the hydrodynamics and then c becomes noticeable toward the shoreline when water depth becomes smaller.

In bed load only cases, the results of two models are very different. Bed change under bed load only is mostly due to shock condition, and most of bed change occurs during first few cycles. However, the shock condition is not applicable in quasi-coupled model. Any bed change due to shock condition is not included in quasi-coupled model. Comparing these two models, it is shown that the shock condition results in a significant difference between two models. In quasi-coupled model, bed change is non-zero, which also illustrates that the spatial variation of

u still exists but is small. Variation of u is due to nonlinear effect, which is only significant in the nearshore region. Therefore, most of the bed change in both models occurs within the intertidal and sub-tidal regions.

7.4 Recommendations

The numerical morphodynamics of tidal motion in the present work, despite of the inclusion of both bed and suspended load and fully coupled, is still limited and idealised in the assumption of shallow water and the exclusion of some physical factors, such as simple sinusoidal signal and simple formula of entrainment and depositional flux of suspended load with the simplification of suspended threshold velocity. Furthermore, the numerical model is designed for CTM in morphodynamics for the first time. The dry bed level, which is currently outside the computational domain but already submerged and altered during the previous tides, has to be stored in the computer memory and will be interpolated if needed. Therefore, the bed within wetting-drying region has to be stored in a good spatial resolution so that the interpolation/extrapolation error is maintained small. There remains considerable work to be done not only for better understanding of the macro-tidal beach morphodynamics but also for better computational efficiency and optimisation.

Firstly, the driven tidal signal prescribed at offshore in § 6 is sinusoidal with constant tidal range and tidal period. While the analysis presented in these cases is a useful starting point to understand the morphodynamics of a macro-tidal beach, most beaches experience a more complex tidal regime. The tidal signal curve experienced by most macro-tidal envrionment is affected by the propagation of tidal wave in the surrounding coastal region, and is generally not sinusoidal

(see *Le Hir et al.* [2000]). In addition, the most significant longer-term variation (in weeks and months scale) in the tidal signal (see *Dyer* [1986]) is the spring neap cycle with an approximate period of two weeks. This variation is even more significant in macro-tidal environment as the neap-spring variation in tidal range may be as large as several meters, with corresponding variations in the cross-shore currents. We therefore should consider both asymmetrical tides and tides which experience a spring-neap cycle.

Secondly, suspended load transport has a great effect on the bed evolution, with bed change due to this mode of transport continuing to develop after many tides. Here, the threshold velocity for suspended load is neglected. The fine sediment mobilisation threshold for suspension, $u_{cr,s}$, could have a greater effect on the bed change as most sediment is transported under suspension rather than bed load (*Soulsby* [1997]). It has been confirmed in § 6.3 that the threshold velocity for bed load has no significant effect on the final bed change for long-term simulation. However, whether or not the same conclusion on bed load can be applied for suspended load is questionable. We therefore could include a threshold in the erosional flux formula to see how this parameter would affect the final bed change.

Thirdly, in tidal motion, a periodic state of hydrodynamics and c is quickly achieved from initial still conditions after the first few cycles. Therefore, any pre-suspended sediment is quickly exchanged between the bed level and the water column, resulting in a higher bed change in the first few cycles. However, for long-term simulation, this pre-suspended sediment concentration value is not very important due to its quick adjustment in the tidal motions. The numerical studies of *Pritchard et al.* [2002] and *Roberts et al.* [2000] impose a constant concentration

at the seaward boundary during flood tide. This represents a uniform sediment supply source at some distance offshore. This is a considerable simplification of the real system, in which the sediment input is controlled by longshore currents and offshore mixing processes, and also is time dependent (*Roberts et al.* [2000]). An input sediment source may represent an estuarine supply source or engineering works such as sand nourishment offshore. It is noted that in the present model, we do not implement any sediment source at the offshore boundary. An instantaneous equilibrium state of suspended sediment is assumed at the offshore boundary during flooding (i.e. neither erosion nor deposition of sediment occurs). As a result, suspended sediment is able to exit the domain but there is no input source, and any exchange of sediment only occurs within the computational domain. A time dependent offshore sediment supply source should be implemented into the model to investigate how a sediment supply source could affect the final bed change.

Additionally, the present model has focused on fine sand sediment. However an alternative erosion formulation could be employed with respect to different sediment types or even the same sediment type. Different quantitative forms of $\hat{E}$ and $\hat{D}$ could be utilised to see whether the solutions are consistent, especially with regard to bed change in the intertidal and sub-tidal regions.

It is noted that a beach of tide-only actions is not commonly found in nature. The contribution of waves into sediment suspension and thus bed change is very important, even in small wave conditions as shown in *Zhou et al.* [2014] and *Roberts et al.* [2000]. However, the wave entrainment mechanism employed in these models is very simple and the sediment is transported under the mean of tidal currents. The interactions in hydrodynamics between waves and tides are

not considered. Therefore, a wave model should be implemented and a simple interaction between waves and tides should be included. This development will increase computational effort since a wave model with different time and length scales will be included. However, the morphodynamics of macro-tidal beaches could be better understood.

It is noted that the equilibrium bed profile is not achieved in the present simulation. Although bed change under bed-load-only decreases and converges toward an equilibrium as shown in § 6, its contribution under tidal currents is not significant compared to suspended load. Within a simulation of $100T$, bed change under suspended load continues developing. An equilibrium profile is obtained after decades in the numerical studies of cohesive sediment in *Roberts et al.* [2000]. Therefore, longer-term simulation should be applied, may be in a similar time length as in *Roberts et al.* [2000] to see if an equilibrium profile could be achieved.

The initial profile may anticipate and lead to big adjustment to the realistic profile. So alternative initial bed profiles can be imposed to compare different initial profiles over a long-term evolution.

Finally, the alongshore current is also an important factor for transporting sediment and thus morphodynamic. Therefore, a development on 2D model including alongshore component should be considered.

APPENDIX A

Appendix A: Sediment motion threshold for bed-load and suspended load

For a slow current in tidal motion, the sediment remains immobile until a certain velocity is reached at which the sediment begins to move either under bed-load transport or mixed into suspension (see *Soulsby* [1997] for clarification between bed load and suspended load transport). This is defined as the threshold of motion, and corresponds to a critical Shields parameter, θ_{cr}. In this appendix, we apply the same procedure as *Zhu and Dodd* [2015] on tidal motions to determine the effect of threshold on sediment movement in both bed and suspended load.

Following *Soulsby* [1997] (eq. SC(77), p.106), the Shields threshold are given empirically as

$$\theta_{cr} = \frac{0.30}{1 + 1.2D_*} + 0.055[1 - \exp(-0.020D_*)] \tag{A.1}$$

where D_* is dimensionless grain size given by

$$D_* = \left[\frac{\hat{g}(s_{rel}-1)}{\hat{\nu}^2}\right]^{1/3} \hat{D}_{50} \tag{A.2}$$

where $\hat{\nu} = 1.36 \times 10^{-6} m^2/s$ is kinematic viscosity of salted water at 10^oC. We take the range of sediment grain size such that $0.1mm < \hat{D}_{50} < 0.4mm$ (very fine to fine sand, see *Soulsby* [1997]). We obtain $D_* = 2.03 - 10.16$ and $\theta_{cr} = 0.033 - 0.089$.

Allen [1985] introduced an approach based on Shield parameter that incorporates critical Shields parameter of suspended load, $\theta_{cr,s}$. The augmented Shields Diagram in Fig. A.1 represents both critical values of Shields parameter θ_{cr} and equivalent critical values for suspended sediment entrainment $\theta_{cr,s}$ as a function of D_*. For small enough sediment grain size, eventually $\theta_{cr,s} = \theta_{cr}$, which means below this grain size, the suspended threshold is meaningless as sediment is immediately entrained into the water column. Following *Van Rijn* [1993], the suspended load threshold and bed load threshold are distinct for $\hat{D}_{50} > 0.25mm$. Below this value, the sediment is immediately entrained into the water column transported under the mean of suspended load.

There is more uncertainty surrounding the equivalent critical threshold for suspended load $\theta_{cr,s}$. Physically, if the sea bed is composed of single grain size, we can expect that $\theta_{cr,s} \geq \theta_{cr}$. The suspended threshold can be obtained empirically through the settling velocity $\hat{w}_s$ (*Van Rijn* [1993])

$$\theta_{cr,s} = \frac{0.16\hat{w}_s^2}{(s_{rel}-1)\hat{g}\hat{D}_{50}} \tag{A.3}$$

$\hat{w}_s$ for all D_* is given by (see *Soulsby* [1997], eqn SC(102), p.134)

$$\hat{w}_s = \frac{\hat{\nu}}{\hat{D}_{50}}[-10.36 + \sqrt{10.36^2 + 1.049D_*^3}] \tag{A.4}$$

The empirical formula (A.3) is applicable for steady flows and the range of fine to medium grain size is considered here. Although the above formulae were

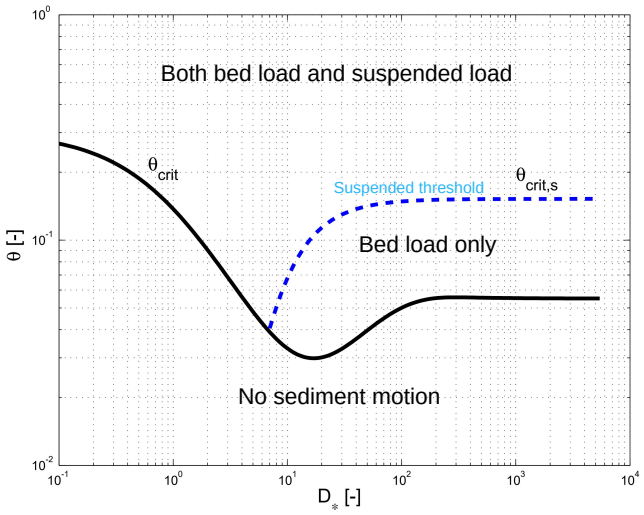


Figure A.1: The augmented Shields Diagram as function of dimensionless grain size (*Allen* [1985]).

developed for steady flows, they can be used on an instantaneous basis in tidal flows because the response time of sand grain in bed load motion is very short compared to tidal periods (*Soulsby* [1997]). The corresponding $\hat{w}_s$ for given grain size is $5.647 \times 10^{-3} - 66.27 \times 10^{-3} ms^{-1}$. Thus, the critical threshold for suspended sediment is $\theta_{cr,s} = 0.032 - 0.091$.

The Shields parameter of a flow is given by

$$\theta = \frac{\hat{\tau}_0}{(\hat{\rho}_s - \hat{\rho})\hat{g}\hat{D_{50}}} \tag{A.5}$$

where $\hat{\rho}_s = 2650 kgm^{-3}$ and $\hat{\rho} = 1027 kgm^{-3}$ are representative sand and salted water densities, $\hat{\tau}_0$ is the bed shear stress, which can be obtained as $\hat{\tau}_0 = \hat{\rho} c_d |\hat{u}| \hat{u}$. The typical value of macro-tidal current $\hat{u}$ is ranged between $0.3 - 0.5 ms^{-1}$ (*Le Hir et al.* [2000]). There is some uncertainty surrounding the value of c_d in the tidal motions. Here we take the rough estimation of $c_d = 0.004 - 0.008$, which is the range of fine cohesive to non-cohesive sediment beaches (see *Roberts et al.* [2000] and *Le Hir et al.* [2000]). It is noted that the lower limit of c_d is consistent

with measurements of *Roberts et al.* [2000] applied on muddy flat. The correct value of c_d for fine sand is not very different from this range (*Roberts et al.* [2000]). Alternatively, the friction velocity, $\hat{u}_*$ is a quantity to express the friction in velocity units and given through experimental data as power-law (see eqn.SC(34), p.54 in *Soulsby* [1997])

$$\frac{\hat{u}_*}{\hat{u}} = \frac{1}{7}(\frac{\hat{D}_{50}}{\hat{h}})^{1/7} \tag{A.6}$$

Then, the bed shear stress can be expressed in term of $\hat{u}_*$ as

$$\hat{\tau}_0 = \hat{\rho}\hat{u}_*^2 = \hat{\rho}c_d\hat{u}^2 \tag{A.7}$$

The bed friction coefficient c_d can also be approximated from (A.7). For the given parameters, $c_d \approx 0.0036$, which is close to the chosen value of 0.004 applied in § 6. From these reference ranges and given grain size, we obtain

$$0.08 < \theta < 1.29 \tag{A.8}$$

The range of θ in (A.8) mostly lies outside the critical range of both θ_{cr} and $\theta_{cr,s}$. This implies that the effect of threshold of movement might be significant only for coarser sand and small tidal currents and small friction. For further simplification, we take $u_{cr,b} = u_{cr,s} = 0$. These simplifications will not significantly affect beach morphodynamics. This has been confirmed for the thresholds applied in bed load transport.

Moreover, the range of $\theta_{cr,s}$ and θ_{cr} are quite similar. This confirms the suggestion of Shields curve in Fig. A.1 that the sediment of given grain size is mostly transported under suspension. From the Shields curve, bed load transport becomes important for coarser sand and smaller tidal currents. Although suspended load transport is more dominant under tidal currents, we still retain bed load transport to investigate its effects, and also for further applications when larger grain size

may be included and the contribution of bed load transport becomes more and more important.

APPENDIX B

Appendix B: Bed mobility under bed load and suspended load transport

The exchange parameter E of (3.44) (or (3.49)) is well determined since there are many available formula to accurately predict $\hat{w}_s$. However, there is still significant uncertainties in determining $\hat{m}_e$ and A and thus, the bed mobility parameter M and σ in non-dimensional form. The bed mobilities under suspended load M and bed load σ need to be estimated carefully to guarantee a reasonable numerical result.

Nielsen [1992] proposed a empirical formula by considering various bedload transport data of different sand grain size for steady currents. The formula was also independently derived by *Soulsby* [1997]. The bed load transport rate as a function of Shields paramters are derived for the considered grain size. The bed mobility parameter A in MPM formula can be approximated from (3.25) once c_d is known. Otherwise, A can be approximated from the procedure given in

section 9.2, p.158 in *Soulsby* [1997]. In both ways, we obtain the approximation of $A = 4.0 \times 10^{-1} s^2 m^{-1}$. We take bed porosity $p = 0.5$, corresponding to $\sigma = 5.0 \times 10^{-4}$.

Regarding the bed mobility under suspended load transport, it is difficult to approximate the value of $\hat{m}_e$ due to insufficient field and experimental data. Moreover, while the settling velocity $\hat{w}_s$ of sand is strongly dependent on the grain size, thus can be approximated accurately (*Soulsby* [1997]); the erosional rate $\hat{m}_e$ is more complicated as there are many factors that can affect the values and this requires more data to calibrate with.

In order to approximate a reasonable value of $\hat{m}_e$, we assume the nearshore concentration being around the instantaneous equilibrium state. At this state, the settling of grains towards the bed is counterbalanced by the entrainment of sediment upwards due to turbulent water motions. This is reasonable as the water depth decreases toward the shoreline and thus the exchange of the sediment between the bed and water column happens in a very short time compared to the tidal motion. The instantaneous equilibrium concentration can be found empirically and thus $\hat{m}_e$ can be approximated. Here we introduce the procedure based on the assumption of instantaneous equilibrium concentration. The equilibrium concentration in vertical direction $\hat{z}$ is given by power-law profile (see eqn. SC(106), p.138 in *Soulsby* [1997])

$$\hat{c}(\hat{z}) = \hat{c}_a \left(\frac{\hat{z}}{\hat{z}_a} \right)^{-b} \tag{B.1}$$

where b is Rouse number or suspension parameter given by

$$b = \frac{\hat{w}_s}{\kappa \hat{u}_*} \tag{B.2}$$

where $\kappa = 0.4$ is von Karman's constant and $\hat{u}_*$ is total friction velocity given in (A.6). The reference concentration $\hat{c}_a$ and reference height $\hat{z}_a$ are empirical values obtained from calibration of a large data set (see section 8.4, p.137 in *Soulsby* [1997]). The most recent expression of $\hat{c}_a$ and $\hat{z}_a$ are given by *Zyserman and Fredsøe* [1994] which seems to give good results

$$\hat{c}_a = \frac{0.331(\theta - 0.045)^{1.75}}{1 + 0.72(\theta - 0.045)^{1.75}} \tag{B.3}$$

$$\hat{z}_a = 2\hat{D}_{50} \tag{B.4}$$

We apply Shields parameter θ in (B.3) instead of the skin-friction Shield parameters θ_s in the original formula (eqn. SC(111), p.142 in *Soulsby* [1997]) because the skin-friction Shields parameter θ_s is only meaningful when the bed is rippled. For the given concentration field, the depth-averaged equilibrium concentration is

$$\hat{c}_{eq} = \frac{1}{\hat{h}} \int_0^{\hat{h}} \hat{c}(\hat{z}) d\hat{z} \tag{B.5}$$

Substituting (B.1) into (B.5) yields

$$\hat{c}_{eq} = \frac{\hat{c}_a \hat{z}_a^b}{\hat{h}} \left[\frac{\hat{h}^{1-b}}{1-b} - \frac{0^{1-b}}{1-b} \right] \tag{B.6}$$

It is noted that $\hat{c}_{eq}$ obtained by (B.6) is a depth-averaged value. The value of $\hat{c}_{eq}$ is derived straightforwardly if $b < 1$. However, the problem occurs as b approaches or gets larger than 1 as both $\frac{\hat{h}^{1-b}}{1-b}$ and $\frac{0^{1-b}}{1-b}$ in (B.6) approach infinity when $x \to 1^+$. The suspended sediment for large b is concentrated mainly near the bed instead of well mixed through the water column. The tidal motion is weak current so only fine sediment is mobilised. Although the tidal current is capable to entrain medium sediment, it is only concentrated near the bed instead of well mixed throughout the water column. The depth-averaged concentration

applied for sediment of $b \geq 1$ is meaningless. Here we make further simplification by assuming that $b < 1$.

It is noted that by applying (B.6) in equilibrium concentration profile, there are two inconvenient properties. Firstly, the equilibrium concentration is a function of θ (included in formula of $\hat{c}_a$) and $\hat{h}$, thus varying with both space and time. It is noted that tidal velocity is nearly spatially constant at a certain time. This is true as the tidal wavelength and period are very large compared to the considered region. We also take further simplification by using the maximum value of velocity. This simplification makes the equilibrium concentration is now only a function of $\hat{h}$. These simplifications also lead to more conservative results. Secondly, as the value of b approaches or becomes larger than 1, the problem occurs as discussed above. Recall that in the governing dimensional model, at equilibrium, the entrainment rate $\hat{E}$ and depositional rate $\hat{D}$ are equal and given by (3.36) and (3.37), respectively. $\hat{m}_e$ at the instantaneous equilibrium state is given by

$$\hat{m}_e = \hat{w}_s \hat{c}_{eq} \left(\frac{\hat{u}_0^2}{\hat{u}^2 - \hat{u}_{cr,s}^2}\right) \tag{B.7}$$

The value of $\hat{u}_{cr,s} = 0$ is assumed (see Appendix § A); thus $\left(\frac{\hat{u}_0^2}{\hat{u}^2 - \hat{u}_{cr,s}^2}\right)$ in (B.7) is assumed unity. The value of $\hat{m}_e$ can be obtained by calculating at some different locations then taking the average value. Otherwise, we can integrate (B.7) over space to obtain the average value. In this case, the latter method will be applied. We only limit to the nearshore region, where the assumption of instantaneous equilibrium is valid. Therefore, the intertidal and sub-tidal regions are considered. For the plane beach given in§ 6, the limit region is set over a distance of $\hat{L} = 2400m$, which is twice the intertidal region. Thus, the

domain-averaged of the depth-averaged concentration, $\hat{C}_{eq}$ is given by

$$\hat{C}_{eq} = \frac{1}{\hat{L}}\frac{1}{\hat{h}}\int_{\hat{x}=0}^{\hat{x}=\hat{L}}\int_{\hat{z}=0}^{\hat{z}=\hat{h}} \hat{c}_{eq} d\hat{x} d\hat{z} \tag{B.8}$$

Here, we note that $\hat{z}$ is related to $\hat{x}$ through bed slope of $\tan\gamma$, i.e. $\hat{z} = (\hat{L} - \hat{x})\tan\gamma$. Therefore, (B.8) over the domain from $\hat{x} = 0$ to $\hat{x} = \hat{L}$ becomes

$$\hat{C}_{eq} = \frac{\hat{c}_a \hat{z}_a^b}{(1-b)^2 \hat{L}^b} \tag{B.9}$$

Here we take the reference parameters applied in § 6, the averaged $\hat{m}_e = 1 \times 10^{-3} ms^{-1}$ is obtained, corresponding to $M = 10.0$ in tidal scales as given in § 3.4.2. In § 6, we also test the morphodynamics of different values of M and E. It is noted that the range of M and E in these tests cover all the ranges of sediment in very fine to fine sand. It is noted that M is not only dependant on sediment properties, but is also a function of bed configurations such as horizontal length scales and bed slope as shown in (B.9).

Bibliography

Allen, J. R. L., editor (1985). *Principles of Physical Sedimentology*. Springer US, Boston, MA.

Antuono, M., Soldini, L., and Brocchini, M. (2012). On the role of the Chezy frictional term near the shoreline. *Theoretical and Computational Fluid Dynamics*, 26:105–116.

Balzano, A. (1998). Evaluation of methods for numerical simulation of wetting and drying in shallow water flow models. *Coastal Engineering*, 34:83–107.

Bassoullet, P., Le Hir, P., Gouleau, D., and Robert, S. (2000). Sediment transport over an intertidal mudflat: field investigations and estimation of fluxes within the Baie de Marenngres-Oleron (France). *Continental Shelf Research*, 20(12–13):1635–1653.

BODC (2013). The british oceanographic data centre annual report 2013/14. Technical report, National Oceanography Centre.

Briganti, R., Dodd, N., Kelly, D. M., and Pokrajac, D. (2012a). An efficient and flexible solver for the simulation of the morphodynamics of fast evolving flows on coarse sediment beaches. *International Journal for Numerical Methods in Fluids*, 69:859–877.

Briganti, R., Dodd, N., Pokrajac, D., and O'Donoghue, T. (2012b). Numerical and experimental description of the flow, boundary layer and bed evolution in bore-driven swash on a coarse sediment beach. *Coastal Engineering Proceedings*, 1.

Brocchini, M. and Dodd, N. (2008). Nonlinear shallow water equation modelling for coastal engineering. *Journal of Waterway, Port, Coastal and Ocean Engineering*, 134(2):104–120.

Brocchini, M., Svendsen, I., Prasad, R., and Bellotti, G. (2002). A comparison of two different types of shoreline boundary conditions. *Computer methods in applied mechanics and engineering*, 1991:4475–4496.

Carrier, G. F. (1966). Gravity waves on water of variable depth. *J. Fluid Mech.*, 24:641–659.

Carrier, G. F. and Greenspan, H. P. (1958). Water waves of finite amplitude on a sloping beach. *J. Fluid Mech.*, 4(1):97–109.

Castro Diaz, M. J., Fernandez-Nieto, E. D., and Ferreiro, A. M. (2008). Sediment transport models in shallow water equations and numerical approach by high order finite volume methods. *Computers & Fluids*, 37:299–316.

Coco, G., Zhou, Z., van Maanen, B., Olabarrieta, M., Tinoco, R., and Townend, I. (2013). Morphodynamics of tidal networks: Advance and challenges. *Marine Geology*, 346:1–16.

Davis, R. A. and Hayes, M. O. (1984). What is a wave-dominated coast? *Marine Geology*, 60:313–329.

Deloffre, J., Lafite, R., Lesueur, P., Lesourd, S., Verney, R., and Guezennec, L. (2005). Sedimentary processes on an intertidal mudflat in the upper macrotidal Seine estuary, France. *Estuarine, Coastal and Shelf Science*, 64(4):710–720.

Dodd, N., Stoker, A. M., Calvete, D., and Sriariyawat, A. (2008). On beach cusp formation. *Journal of Fluid Mechanics*, 597:145–169.

Dyer, K. R. (1986). *Coastal and Estuarine Sediment Dynamics*. Wiley.

Fagherazzi, S. and Wiberg, P. L. (2009). Importance of wind conditions, fetch, and water levels on wave generated shear stresses in shallow intertidal basins. *Journal of Geophysical Research: Earth Surface*, 114(F3).

Falissard, F. (2015). Uneven-order decentered Shapiro filters for boundary filtering. *Journal of Computational Physics*, 292:168–178.

Falqués, A., Montoto, A., and Iranzo, V. (1996). Bed-flow instability of the longshore current. *Continental Shelf Research*, 16:1927–1964.

Fredsøe, J. and Deigaard, R. (1992). *Mechanics of Coastal Sediment Transport*, volume 3 of *Advanced Series on Ocean Engineering*. World Scientific, 1 edition.

Friedrichs, C. T. (2011). Tidal flat morphodyamics: a synthesis. In Wolanski, E. and McLusky, E. D., editors, *Treatise on Estuarine and Coastal Science*, volume 3, pages 137–170. Academic Press, Waltham.

Friedrichs, C. T. and Aubrey, D. G. (1996). *Uniform Bottom Shear Stress and Equilibrium Hyposometry of Intertidal Flats*, volume 50, pages 405–429. American Geophysical Union.

Garnier, R., Calvete, D., Falqués, A., and Dodd, N. (2008). Modelling the formation and the long-term behavior of rip channel systems from the deformation of a longshore bar. *Journal of Geophysical Research*, 113:1–18.

Gjevik, B. and Pedersen, G. (1981). *Run-up of long waves on an inclined plane*. Department of Mathematics, University of Oslo.

Goto, C. and Shuto, N. (1980). Run-up of tsunamis by linear and nonlinear theories. In *Coastal Engineering Proceedings: Proceedings of 17th Conference on Coastal Engineering, Sydney, Australia, 1980.*, volume 17, pages 670–695. Coastal Engineering Research Council.

Grass, A. (1981). Sediment transport by waves and currents. Technical Report FL29, Ma. Tecnol., SERC London Cent.

Hibberd, S. and Peregrine, D. H. (1979). Surf and run-up on a beach: a uniform bore. *J. Fluid Mech.*, 95(2):323–345.

Hubbard, M. E. and Dodd, N. (2002). A 2D numerical model of wave runup and overtopping. *Coastal Engineering*, 47:1–26.

Huynh, V. L., Dodd, N., and Zhu, F. (2017). Coastal morphodynamical modelling in nonlinear shallow water framework using a coordinate transformation method. *Advances in Water Resources*, 107.

Incelli, G. (2016). *A fully-coupled coastal hydro-morphodynamical numerical solver*. PhD thesis, University of Nottingham.

Incelli, G., Briganti, R., and Dodd, N. (2015). Absorbing-generating seaward boundary conditions for fully-coupled hydro-morphodynamical solvers. *Coastal Engineering*, 99:96–108.

Incelli, G., Dodd, N., Blenkinsopp, C. E., Zhu, F., and Briganti, R. (2016). Morphodynamical modelling of field-scale swash events. *Coastal Engineering*, 115:42–57.

Johns, B. (1982). Numerical integration of the shallow water equations over a sloping shelf. *international Journal for Numerical methods in Fluids*, 2:253–261.

Kelly, D. M. (2009). *Bore-Driven Swash on a Mobile Beach*. PhD thesis, University of Nottingham.

Kelly, D. M. and Dodd, N. (2009). Floating grid characteristics method for unsteady flow over a mobile bed. *Computers and Fluids*, 38(4):899–909.

Kelly, D. M. and Dodd, N. (2010). Beach face evolution in the swash zone. *Journal of Fluid Mechanics*, 661:316–340.

Kobayashi, N. and Johnson, B. D. (2001). Sand suspension, storage, advection, and settling in surf and swash zones. *Journal of Geophysical Research*, 106:9363–9376.

Kobayashi, N., Otta, A. K., and Roy, I. (1987). Wave reflection and runup on rough slopes. *Journal of Waterway, Port, Coastal and Ocean Engineering*, 113(3):282–298.

Kroon, A. and Masselink, G. (2002). Morphodynamics of intertidal bar morphology on a macrotidal beach under low-energy wave conditions, North Lincolnshire, England. *Marine Geology*, 190:591–608.

Le Hir, P., Roberts, W., Cazaillet, O., Christie, M., Bassoullet, P., and Bacher, C. (2000). Characterization of intertidal flat hydrodynamics. *Continental Shelf Research*, 20(12-13):1433–1459.

Liu, P. L. F., Yeh, H., and Synolakis, C., editors (2008). *Advanced numerical models for simulating tsunami waves and runup*. Advances in Coastal and Ocean Engineering, Volume 10. World Scientific, Singapore.

Liu, X. J., Gao, S., and Wang, Y. P. (2011). Modeling profile shape evolution for accreting tidal flats composed of mud and sand: a case study of the central jiangsu coase, china. *Continental Shelf Research*, 31(16):1750–1760.

Lynett, P. J., Wu, T. R., and Liu, P. L. F. (2002). Modeling wave runup with depth-integrated equations. *Coastal Engineering*, 46:89–107.

Mariotti, G. and Fagherazzi, S. (2013). Wind waves on a mudflat: the influence of fetch and depth on bed shear stresses. *Continental Shelf Research*, 60:S99–S110.

Masselink, G. and Hughes, M. G. (1998). Field investigation of sediment transport in the swash zone. *Continental Shelf Research*, 18:1179–1199.

Masselink, G. and Hughes, M. G., editors (2003). *Introduction to coastal processes and geomorphology*. Hodder Arnold, London.

Masselink, G. and Short, A. D. (1993). The effect of tide range on beach Morphodynamics and Morphology: A conceptual beach model. *Journal of Coastal Research*, 9(3):785–800.

Nielsen, P. (1992). *Coastal Bottom Boundary Layers and Sediment Transport*, volume 4 of *Advanced Series on Ocean Engineering*. World Scientific.

Özkan-Haller, H. T. and Kirby, J. T. (1997). A Fourier-Chebyshev collocation method for the shallow water equations including shoreline runup. *Applied Ocean Research*, 19:21–34.

Panton, R. L. (2005). *Incompressible Flow*. Hoboken, NJ: Wiley.

Pedrozo-Acuna, D. (2013). *Numerical Modelling of the Sorting and Transport of Non-uniform Sediments in the Swash Zone*. PhD thesis, University of Nottingham.

Peregrine, D. H. (1967). Long waves on a beach. *J. Fluid Mech.*, 77:417–431.

Peregrine, D. H. and Williams, S. M. (2001). Swash overtopping a truncated plane beach. *J. Fluid Mech.*, 440:391–399.

Postacchini, M., Brocchini, M., Mancinelli, A., and Landon, M. (2012). A multi-purpose, intra-wave, shallow water hydro-morphodynamic solver. *Advances in Water Resources*, 38:13–26.

Prasad, R. and Svendsen, I. (2003). Moving shoreline boundary condition for nearshore models. *Coastal Engineering*, 49:239–261.

Price, T. D. and Ruessink, B. G. (2008). Morphodynamic zone variability on a microtidal barred beach. *Marine Geology*.

Pritchard, D., Hogg, A., and Roberts, W. (2002). Morphological modelling of intertidal mudflats: the role of cross-shore tidal currents. *Continental Shelf Research*, 22(11-13):1887–1895.

Pritchard, D. and Hogg, A. J. (2003a). Cross-shore sediment transport and the equilibrium morphology of mudflats under tidal currents. *Journal of Geophysical Research: Oceans*, 108(C10):2156–2202.

Pritchard, D. and Hogg, A. J. (2003b). On fine sediment transport by long waves in the swash zone of a plane beach. *Journal of Fluid Mechanics*, 493:255–275.

Pritchard, D. and Hogg, A. J. (2005). On the transport of suspended sediment by a swash event on a plane beach. *Coastal Engineering*, 52:1–23.

Reniers, A. J., Gallagher, E. L., MacMahan, J. H., Brown, J. A., Rooijen, A. A., van Thiel de Vries, J. S., and van Prooijen, B. C. (2013). Observations and modeling of steep-beach grain-size variability. *Journal of Geophysical Research*, 118:577–591.

Reniers, A. J. H. M., Roelvink, J. A., and Thornton, E. B. (2004). Morphodynamic modeling of an embayed beach under wave group forcing. *Journal of Geophysical Research: Oceans (1978-2012)*, 109:1–22.

Roberts, W., Le Hir, P., and Whitehouse, R. (2000). Investigation using simple mathematical models of the effect of tidal currents and waves on the profile shape of intertidal mudflats. *Continental Shelf Research*, 20(10-11):1079–1097.

Shapiro, R. (1970). Smoothing, Filtering, and Boundary Effects. *Review of Geophysics and Space Physics*, 8(2):359–387.

Shen, M. C. and Meyer, R. E. (1963). Climb of a bore on a beach part 3: Run-up. *J. Fluid Mech.*, 16:113–125.

Short, A. D. (1991). Macro-Meso tidal beach morphodynamics - An overview. *Journal of Coastal Research*, 7(2):417–436.

Sielecki, A. and Wurtele, M. G. (1970). The numerical integration of the nonlinear shallow-water equations with sloping boundaries. *Journal of Fluid Mechanics*, 6:219–236.

Smith, G. D. (1985). *Numerical Solution of Partial Differential Equations: Finite Difference Methods*. Oxford applied mathematics and computing science series. Oxford University Press, 3rd edition.

Sobey, R. J. (2009). Wetting and drying in coastal flows. *Coastal Engineering*, 56:565–576.

Sorensen, R. M. (2005). *Basic Coastal Engineering*. Springer US, 3rd edition edition.

Soulsby, R. L. (1997). *Dynamics of marine sands*. Thomas Telford, 1 edition.

Sriariyawat, A. (2009). *Formation and evolution of beach cusps*. Ph.{d}. thesis, University of Nottingham.

Stoker, J. J. (1948). The formation of breakers and bores. *Communications on Pure and Applied Mathematics*, 1:1–87.

Svendsen, I. A., editor (2005). *Introduction to nearshore hydrodynamics. Volume 24 of Advanced Series on Ocean Engineering*. World Scientific Publishing, Singapore.

Synolakis, C. (1987). The runup of solitary waves. *Journal of Fluid Mechanics*, 185:523–545.

Takeda, H. (1984). Numerical simulation of run-up by variable transformation. *Journal of The Oceanographical Society of Japan*, 40:271–278.

Titov, V. V. and Synolakis, C. E. (1995). Modeling of breaking and nonbreaking long-wave evolution and runup using VTCS-2. *Journal Waterway Port Coastal Ocean Engineering*, 121(6):308–316.

Titov, V. V. and Synolakis, C. E. (1998). Numerical modeling of tidal wave runup. *Journal Waterway Port Coastal Ocean Engineering*.

Van Dongeren, A. R. and Svendsen, I. A. (1997). An absorbing-generating boundary condition for shallow water models. *Journal Waterway Port Coastal Ocean Engineering*, 6(123):303–313.

Van Rijn, L. C. (1993). *Principles of Sediment Transport in River, Estuaries and Coastal Seas*. Aqua Publications, Amsterdam.

Vreugdenhil, C. B. (1994). *Numerical Methods for Shallow Water Flow*. Boston: Kluwer Academic Publishers.

Wang, Y. P., Gao, S., Jia, J., Thompson, C. E. L., Gao, J., and Yang, Y. (2012). Sediment transport over an accretional intertidal flat with influences of reclamation, Jiangsu coast, China. *Marine Geology*, 291–294:147–161.

Wright, L. D. and Short, A. D. (1984). Morphodynamic variability of surf zones and beaches: A synthesis. *Marine Geology*, 56:93–118.

Zelt, J. A. (1986). Tsunamis: the response of harbours with sloping boundaries to long wave excitation. Technical Report Technical Report KH-R-47, California Institute of Technology, Pasadena, California.

Zhou, X., Hon, Y. C., and Cheung, K. F. (2004). A grid-free, nonliear shallow-water model with moving boundary. *Engineering Analysis with Boundary Elements*, 28(8):967–973.

Zhou, Z., Coco, G., Jimenez, M., Olabarrieta, M., van der Wegen, M., and Townend, I. (2014). Morphodynamics of river-influenced back-barrier tidal

basins: The role of landscape and hydrodynamic settings. *Water Resources Research*, 50:9514–9535.

Zhou, Z., Coco, G., van der Wegen, M., Gong, Z., Zhang, C., and Townend, I. (2015). Modeling sorting dynamics of cohesive and non-cohesive sediments on intertidal flats under the effect of tides and wind waves. *Continental Shelf Research*, 104:76–91.

Zhu, F. (2012). *1D morphodynamical modelling of swash zone beachface evolution*. PhD thesis, University of Nottingham.

Zhu, F. and Dodd, N. (2013). Net beach change in the swash zone: A numerical investigation. *Advances in Water Resources*, 53:12–22.

Zhu, F. and Dodd, N. (2015). The morphodynamics of a swash event on an erodible beach. *Journal of Fluid Mechanics*, 762:110–140.

Zyserman, J. A. and Fredsøe, J. (1994). Data analysis of bed concentration of sediment. *Journal of Hydraulic Engineering, ASCE*, 120(9):1021–1042.